PHYSICS OF COMPTON SCATTERING AND X-RAY SPECTRA OF WEAKLY MAGNETING ACCRETING NEUTRON STARS

BY

DIMITRIOS PSALTIS

Dipl., Aristotle University-Thessaloniki, 1992
M.S., University of Illinois at Urbana-Champaign, 1994

THESIS

Submitted in partial fullfilment of the requirements
for the degree of Doctor of Philosophy in Astronomy
in the Graduate College of the
University of Illinois at Urbana-Champaign, 1998

Urbana, Illinois

UNIVERSITY OF ILLINOIS AT URBANA-CHAMPAIGN

THE GRADUATE COLLEGE

August 22, 1997

WE HEREBY RECOMMEND THAT THE THESIS BY

Dimitrios Psaltis

ENTITLED "Physics of Compton Scattering and X-ray Spectra of Weakly Magnetic Accreting Neutron Stars"

BE ACCEPTED IN PARTIAL FULFILLMENT OF THE REQUIREMENTS FOR THE DEGREE OF Doctor of Philosophy

F. K. Lamb
Director of Thesis Research

R. W. Clusker
Head of Department

Committee on Final Examination†

F. K. Lamb
Chairperson

Gordon Baym

Demetrios Michalas

Ronald F. Webbink

† Required for doctor's degree but not for master's.

O-517

UNIVERSITY OF ILLINOIS AT URBANA-CHAMPAIGN

GRADUATE COLLEGE DEPARTMENTAL FORMAT APPROVAL

THIS IS TO CERTIFY THAT THE FORMAT AND QUALITY OF PRESENTATION OF THE THESIS SUBMITTED BY DIMITRIOS PSALTIS AS ONE OF THE REQUIREMENTS FOR THE DEGREE OF Doctor of Philosophy of Astronomy IS ACCEPTABLE TO THE Department of Astronomy.

Full Name of Department, Division or Unit

18 Aug 1998

Date of Approval

R M Cutcher

Departmental Representative

PHYSICS OF COMPTON SCATTERING AND X-RAY SPECTRA OF WEAKLY MAGNETIC ACCRETING NEUTRON STARS

Dimitrios Psaltis, Ph.D.
Department of Astronomy
University of Illinois at Urbana-Champaign, 1997
Frederick K. Lamb, Advisor

Compton scattering of photons by non-relativistic electrons is thought to play an important role in forming the radiation spectrum of many astrophysical systems. Here we study in detail Compton scattering of photons by electrons with non-negligible thermal and bulk velocities and apply our results to understanding the X-ray spectra of weakly magnetic accreting neutron stars. We first derive the time-dependent radiative transfer equation that describes spontaneous and induced Compton scattering as well as absorption and emission by static and moving media. We demonstrate that terms in the radiative transfer equation that are second-order in the electron bulk velocity should usually be retained, because the effects described by these terms can be as important as the effects described by the terms that are first-order in the electron bulk velocity, even when this bulk velocity is small. We then develop a numerical algorithm for solving the radiative transfer equation in systems with spherical symmetry. The algorithm is a generalization of the method of Eddington factors and provides solutions that are valid both in the diffusion and free-streaming regimes. Using this algorithm we perform detailed numerical calculations of the X-ray spectra of the so-called Z sources that are consistent with models of their rapid variability. We show that electron cyclotron emission near the surface of neutron stars with surface magnetic field strengths of $10^9 - 10^{10}$ G, when Comptonized by a hot central corona and a cool radial inflow, produce X-ray spectra and color-color tracks in excellent agreement with observations. We suggest that the differences in the spectra and rapid variability of different Z sources can be attributed to differences in their magnetic field strengths.

To Vicky

Acknowledgements

Life in graduate school follows a tangled road that sometimes is steep and uphill and at other times is full of pleasant surprises. Being very close to reaching the end of this journey I cannot but express my gratitude to all the people who helped and supported me all these years.

Fred Lamb, my thesis advisor, has been a continuous source of inspiration, support, and excitement throughout this effort. He has always been realistic in showing me the world of science and was a good companion in periods of happiness and frustration. His deep understanding of astrophysics as well as his breadth and versatility have set very high standards for me to follow. I very much appreciate the fact that he encouraged me to get involved with all the research projects he was working on as well as the fact that he shared with me almost every aspect of his professional life with no hesitation. I am also especially grateful to him for his emotional and practical support during a very rough period in the Spring of 1996. We really had lots of fun together these last four years, from spending several hours trying to understand a single aspect of a research project to drinking double cappuccinos at local coffee shops, from writing and rewriting research proposals to biking through the streets of Amsterdam.

Several other people have left their mark on the development of my scientific personality. Dimitri Mihalas provided the foundations of my education on radiative transport with his two excellent courses on the subject. His intuition, limitless knowledge, and unique talent in capturing the gist of every question I asked saved me from many troubles (and this is not just because he's "been in this job for a long time

now" as he used to say). Michiel van der Klis was in a way responsible for starting me working on the subject of my thesis several years before I even came to the University of Illinois. He shared with me the excitement of analyzing X-ray data and tried hard to show me "the way science goes". Michiel and the whole research group at the University of Amsterdam have also been extremely helpful in providing me with their observational results in advance of publication on several occasions.

It would have probably taken me much longer to finish my thesis project had I not received from Guy Miller a numerical code to solve my first Comptonization problems. Cole Miller was the other Miller with whom I had the pleasure to collaborate (although he really made me feel ignorant several times with his questions on ... Greek Mythology!). Our long discussions on the phone and his support and encouragement kept me (and AT&T) going this last year.

During my five years at the University of Illinois I was also privileged to have extensive discussions or collaborations with a number of scientists whose office doors were always open for students to enter. Gordon Baym has always been insightful when talking about transport problems, Doug Swesty often provided me with solutions to the numerical problems I faced, and Ron Webbink was always ready to share his insights on problems of binary star evolution. Moreover, Telemachos Mouschovias taught me how stars are formed, whereas Icko Iben showed me how they evolve. During the same time I also had the pleasure of collaborating with a number of other graduate students and postdocs, especially with Luca Zampieri, Erik Kuulkers, Rudy Wijnands, and Pascal Daumerie, on a variety of research projects. Many thanks also go to Willa Hollis, Sandie Osterbur, Deana Pettigrew, and especially Carol Stickrod for helping me out with all the paperwork necessary to enter, survive, and leave graduate school.

My scientific life and early career choices have been significantly influenced by

three wonderful people and good friends back home, Jiannis Seiradakis, Stavros Avgoloupis, and Giorgos Kolovos, whom I also wish to thank.

Life in graduate school is, of course, a lot more than just research and paper writing (or at least that's what everybody likes to believe!). Astro 500, the most important class offered by the Department, which met every Friday at local bars and taught us about friendship and attitude, was absolutely the best way to start a good weekend. All the members of this class and especially Vicky, Sean ("nobody loves me") Points, Jeff ("the drummer") Veal, Robert ("the extragalactic freak") Gruendl, Paschalis ("appetizer") Paschos, Gail ("ponytail") Conway, Silvia ("the look") Zane, and Scott ("no doubt about it") Teare have made my last year a wonderful one that I will never forget. During the last several months I was also introduced to a variety of new activities, some of which became real hobbies. Chris Fryer showed me how to juggle, Jeff and Sean taught me how to play frisby, and Jeff, Sean, Mark Sincell, and Ray Plante showed me how to play 12-bar blues on the guitar.

A number of very good Greek friends were responsible for making Greece seem much closer to Illinois than it really is. Leonidas Tsetseris has been around almost from the beginning and shared with me and Vicky a number of events that we will always remember, including the midnight flood in our apartment during his first week in the U.S.A. Paschalis Paschos, Manolis Antonoyiannakis, Jiannis Giapitzakis, and Thekla Halouva have also kept my Greek spirit alive all these years. Finally, electronic mail made it possible for me never to lose contact with several wonderful friends from my college years, and especially with Nikos Konstantinidis, Kostas Karafasoylis, Stefania Lampoura, and Jiannis Alexandrou in Europe and with Hara Papathanassiou and Philippos Papadopoulos in the U.S.

My sister and brother-in-law, Natasa and Giorgos, made the transition from Greece to the U.S. an easy one with all their help and support, especially during my first two years here. I really feel lucky and thankful for being their young brother!

Moreover, I feel grateful to my parents for giving me their unconditional love and support as well as for understanding and appreciating my personal efforts and goals. In fact, they are really the ones who first started me thinking about science with their present on my tenth birthday.

I have already filled several pages acknowledging all the people that made it possible for me to go through this last step in my formal education. I should probably fill at least as many pages expressing my thankfulness and love to my best friend, partner in science, and, above all, companion in life, Vicky. It has always been the warmth of her presence that gave me the strength to go forward and at the same time to take a step backwards and see the 'big picture'. These past eleven years, we shared every single moment in our lives, growing up together. I am looking forward to many more to come.

This research was supported in part by NSF grants AST 93-15133 and AST 96-18524, NASA grants NAG 5-2925 and NAGW 2935, and several Rossi X-ray Timing Explorer grants.

Contents

Chapter 1

Introduction

1.1 Compact Objects in Low-Mass X-ray binaries: A Historical Overview

X-ray astronomy was born thirty-five years ago with the detection of Sco X-1, the brightest X-ray source in the sky towards the constellation of Scorpio (Giacconi et al. 1962; see also Gursky [1994] for an interesting account of the 'discovery flight'). The properties of this source were puzzling and several years later Shklovskii (1968; although see Trimble 1994) suggested that Sco X-1 may be a compact object accreting from a companion star. The detection of an optical counterpart to this X-ray source that showed a periodic brightness modulation with a period of 0.78 days provided conclusive evidence that this is indeed a binary stellar system (Gottlieb et al. 1975). In the late 60's and early 70's, observations with rocket experiments and with *UHURU*, the first satellite dedicated to X-ray astronomy, revealed a whole population of X-ray sources in binary systems, the so-called X-ray binaries.

Many X-ray binaries show periodic modulations of their X-ray brightness with periods $\sim 1-100$ seconds (see, e.g., Giacconi et al. 1971) or cyclotron scattering features in their X-ray spectra at energies ~ 10 keV. It was soon realized that the compact objects in these systems were strongly magnetic ($\sim 10^{12}$ G) accreting neutron stars and their X-ray brightness was modulated at the spin frequency of the neutron star (see

Pringle & Rees 1972; Davidson & Ostriker 1973; Lamb, Pethick, & Pines 1973). Discovery of the optical counterparts of these accretion-powered pulsars showed that the companion to the neutron stars, in most of these systems, is a massive star ($\gtrsim 8 M_\odot$, see van Paradijs [1991] for a review); however, four accretion-powered pulsars are in low-mass binary systems—GX 1+4, 4U 1626−67, Her X-1, and J1744−25 (the last is the recently discovered Bursting Pulsar; Kouveliotou et al. 1996). No companions have so far been detected for five X-ray pulsars (see Meregheti & Stella 1995).

Observations of about half of the X-ray binary systems show no evidence for periodic oscillations of their X-ray brightness or cyclotron features in their X-ray spectrum (see van Paradijs [1991] for a review). Searches for optical counterparts to these X-ray sources were either unsuccessful or revealed low-mass ($\lesssim 1.5 M_\odot$) main sequence or giant-branch companions. In the mid 1970's two types of X-ray bursts were discovered from low-mass X-ray binary systems (Grindlay et al. 1976; Belian, Conner, & Evans 1976; see Lewin, van Paradijs, & Taam 1995 for a review). The so-called type I X-ray bursts were attributed to thermonuclear burning in the surface layers of the neutron star (see Hansen & van Horn 1975; Woosley & Taam 1976; Lamb & Lamb 1978) and provided the first direct evidence that the compact objects in these particular X-ray binaries are neutron stars. The so-called type II X-ray bursts (seen so far only from the Rapid Burster [Lewin et al. 1976] and possibly from J1744−28 [Lewin et al. 1996]) were attributed to instabilities in the accretion disks (see Lewin, van Paradijs, & Taam 1995).

The launch of *EXOSAT* in 1983 brought the discovery of two types of quasi-periodic oscillations in the brightest low-mass X-ray binaries (LMXBs) with frequencies ∼5–60 Hz (van der Klis et al. 1985; Middleditch & Priedhorsky 1986). These rapid-variability phenomena were found to be correlated with the X-ray spectral states of the sources (Hasinger & van der Klis 1989; van der Klis 1989) and provided further evidence that the compact objects in these particular systems are weakly magnetic,

accreting neutron stars, spinning at frequencies $\gtrsim$100 Hz (see Ghosh & Lamb 1992).

More recently, observations of neutron-star low-mass X-ray binaries using the Rossi X-ray Timing Explorer have revealed a new set of phenomena that occur on timescales of $\sim$ 1 millisecond, such as quasi-periodic oscillations with frequencies $\sim 300 - 1200$ Hz (see, e.g., van der Klis et al. 1996; Strohmayer et al. 1996; Berger et al. 1996; Zhang et al. 1996; see van der Klis 1997 for an early review), nearly coherent oscillations with frequencies $\sim 300 - 600$ Hz during type I X-ray bursts (see, e.g., Strohmayer et al. 1996; Smith & Morgan 1997), and ~ 30 μs time-lags between hard and soft X-rays during kilohertz quasi-periodic oscillations (Vaughan et al. 1997). All these phenomena occur on timescales that are comparable to the dynamical timescale at radii comparable to the radius of a neutron star and therefore probe the physical conditions very close to the neutron star surface.

1.2 Compact Objects in Low-Mass X-ray binaries: Physical Properties

In accretion-powered pulsars, the properties of the brightness oscillations at the spin frequency and, in same cases, cyclotron scattering lines in the spectrum can constrain significantly their magnetic field strengths and mass accretion rates. In most LMXB systems, however, neither of these two phenomena have ever been observed. In these systems, it is the properties of type I X-ray bursts, quasi-periodic oscillations, and continuum X-ray spectra that provide valuable information about the physical conditions near the accreting compact object.

1.2.1 Type I X-ray Bursts

Type I X-ray bursts have been observed from about 35 low-mass X-ray binaries (see van Paradijs 1995 and Lewin, van Paradijs, & Taam 1995 for recent reviews). They are characterized by a rapid ($\sim$ 1 s) rise of the X-ray flux (see though Murakami

et al. 1980) followed by a slow ($\sim 10 - 100$ s) decay to the pre-burst level. The total energy radiated during type I X-ray bursts is typically ~ 100 times smaller than the energy radiated during the the interval between bursts. The X-ray spectra of most type I X-ray bursts is well described by the sum of the pre-burst X-ray spectrum of the source plus a blackbody component with a temperature that decreases as the burst decays and an emitting area comparable to the surface area of a neutron star (Swank et al. 1977).

These and other properties of type I X-ray bursts are well understood in terms of the thermonuclear-flash model (Joss 1977; Lamb & Lamb 1977, 1978) according to which type I X-ray bursts are produced by a helium flash deep in the accreted layer on the surface of the compact object. Helium burning is not delayed by β-decays (as is hydrogen burning) and therefore proceeds rapidly, naturally explaining the fast rise of the X-ray flux during a burst (Lamb & Lamb 1977, 1978). Moreover, the energy per baryon released during helium burning is a few percent of the potential energy per baryon on the neutron star surface and therefore the ratio of the energy released during type I X-ray bursts to the accretion energy radiated in the persistent emission of a burster can be accounted for if the compact object in the system is a neutron star.

Detailed models of nuclear burning of the surface layers of neutron stars revealed additional properties of type I X-ray bursts as well as some complications. For example, Nozakura, Ikeuchi, & Fujimoto (1984) and Bildsten (1994, 1995) have discussed the possibility that non-uniform accretion onto the neutron star leads to non-uniform burning and propagation of burning fronts. Fushiki & Lamb (1987) showed that the properties of the type I X-ray bursts depend not only on the local mass accretion rate on the neutron star but also on the temperature of its deep surface layers and hence on whether these surface layers are in steady state or not. Bildsten, Wasserman, & Salpeter (1992) showed that, under a very wide range of physical conditions,

nuclear spalation of carbon, oxygen, and nitrogen by the accretion flow can alter the composition, the rate of steady hydrogen burning, and the temperature profile at the surface layers of the neutron star, and hence inhibit the bursting activity.

During very energetic type I X-ray bursts, the outward radiation flux through the surface layers of the neutron star becomes higher than the Eddington critical flux, at which the outward radiation force balances gravity, forcing these surface layers to expand. The emerging X-ray luminosity during this phase of radius expansion is maintained very close to the Eddington critical luminosity because the additional luminosity goes into the expanding gas (Ebisuzaki, Hanawa, & Sugimoto 1983; Kato 1983). The peak X-ray flux of a burst with radius expansion can therefore be used as a standard candle. The persistent X-ray luminosity of a source can be estimated if the ratio of the persistent X-ray flux to the peak X-ray flux of such a burst is measured. This approach has led to determinations of the persistent X-ray luminosities and mass accretion rates of a number of low-luminosity LMXBs (see van Paradijs & van der Klis 1994).

If the rate of mass accretion rate onto the neutron star is comparable to the Eddington critical rate $\dot{M}_E$, helium burning in the stellar surface layers becomes stable and the bursting activity is suppressed (see Fushiki & Lamb 1987). This result is in general agreement with observations of high-luminosity LMXBs, which in general do not burst. However, weak, possibly type I X-ray bursts have been observed from two sources, GX 17+2 (Tawara et al. 1983; Sztajno et al. 1986; Kuulkers 1995) and Cyg X-2 (Kahn & Grindlay 1984; Kuulkers, van der Klis, & van Paradijs 1995; Wijnands et al. 1997), both of which accrete matter at near-Eddington rates. Slow hydrogen burning in the deep layers below the He-burning layer may be responsible for these weak X-ray bursts (Taam, Woosley, & Lamb 1996).

1.2.2 Quasi-Periodic Oscillations

Three types of quasi-periodic oscillations (QPOs) have been discovered in low-mass X-ray binaries, the so-called horizontal branch oscillation (HBO), the normal/flaring branch oscillation (N/FBO), and the kilohertz quasi-periodic oscillations (kHz QPOs).

Horizontal-branch oscillations.—Quasi-periodic oscillations with centroid frequencies $\sim 10 - 60$ Hz that in general increase with increasing mass accretion rate have been observed from several LMXBs with mass accretion rates $\sim 0.5 - 0.9\dot{M}_E$, when the sources are on the so-called horizontal branch in their color-color diagrams (van der Klis et al. 1985; see van der Klis 1989 for a review). The rms amplitudes of these QPOs increase with increasing photon energy and are typically $\sim 1 - 6\%$; the fractional widths $\Delta\nu/\nu$ of the peaks are $\lesssim 0.3$.

Soon after the discovery of the HBO, the centroid frequency of the oscillation was identified with the difference between the orbital frequency of density inhomogeneities in the accretion disk at the inner radius of the Keplerian flow of the gas that is threaded by the stellar magnetic field and the stellar spin frequency (Alpar & Shaham 1985; Lamb et al. 1985; Shibazaki & Lamb 1987). According to this beat-frequency model, as the mass accretion rate through the inner accretion disk increases the disk penetrates closer to the neutron star surface and the beat frequency increases. Comparison of the beat frequencies predicted by various models of the disk-magnetosphere interaction with observations of HBOs in bright LMXBs suggests that the spin frequencies of the neutron stars in these sources are $\sim 100 - 300$ Hz and their dipole surface magnetic-field strengths are $\sim 10^9$ G (Ghosh & Lamb 1992). In two LMXBs the HBO frequency has been observed to decrease with increasing mass accretion rate, when the latter became comparable to $\dot{M}_E$ (Wijnands et al. 1996, 1997). This has been attributed to the loss of mass from the inner accretion disk at near-Eddington mass accretion rates and leads to an upper bound the neutron star magnetic field in these sources of $\sim 5 - 8 \times 10^9$ G.

Horizontal branch oscillations observed at high photon energies ($\gtrsim$10 keV) were shown to lag the oscillations at lower energies by a few milliseconds (see, e.g., van der Klis et al. 1987c). Compton scattering in a medium that surrounds the emitting region can produce such time lags and this effect was used by, e.g., Stollman et al. (1987) and Wijers, van Paradijs, & Lewin (1987) to explain the time lags observed during an HBO. However, the large required size of the Comptonizing region ($\sim 10^7 - 10^8$ cm) and the observation of time lags in the second harmonic of the fundamental HBO frequency that differ from the time lags in the fundamental introduce complications to the suggested explanation (Vaughan et al. 1994a).

Normal/flaring branch oscillations.—Quasi-periodic oscillations with frequencies $\sim 5 - 20$ Hz have been observed from LMXBs when the systems are in the so-called normal or flaring branches in their color-color diagrams and the compact objects are accreting matter at accretion rates that are comparable to (and possibly within a few percent of) the critical Eddington mass accretion rate (Middleditch & Priedhorsky 1986). The rms amplitudes of these oscillations depend strongly on photon energy and are typically $\sim 1 - 6\%$ (see, e.g., Mitsuda 1988).

A number of theoretical models have been proposed to explain the normal/flaring branch oscillations (for a discussion of the various models for quasi-periodic oscillations see Lamb 1986, 1991). For example, Alpar et al. (1992) have suggested that sound waves propagating in a geometrically thick region of the accretion disk cause the electron scattering optical depth to oscillate and hence produce a color oscillation. McDermott & Taam (1987) and Bildsten & Cutler (1995; see also Bildsten, Ushomirsky, & Cutler 1996) have attributed the N/FBO to oscillations at the surface layers of the neutron star excited by nuclear burning.

The radiation-hydrodynamic model of Fortner, Lamb, & Miller (1989; see also Fortner 1992; Miller & Lamb 1992) is currently the most appealing for the normal/flaring branch oscillation because it provides a natural explanation for many of

the properties of this QPO, such as the occurrence of the oscillations only in the brightest sources, their frequencies, and the energy dependence of their amplitudes. According to this model, when the mass accretion rate onto the neutron star becomes comparable to $\dot{M}_E$, a region of approximately radial inflow forms around the compact object. Oscillations in this region with a frequency equal to the inverse infall time from its outer boundary become weakly damped at these high mass accretion rates and are excited by fluctuations in the accretion flow. These oscillations appear as QPOs in the power-density spectra of the Z sources.

The rms amplitudes of the normal/flaring branch oscillations in two of the brightest LMXBs (Cyg X-2 and GX 5−1) have a minimum at a low photon energy (6 keV and 2 keV respectively) and the oscillations above this energy are almost 180° out of phase with respect to the oscillations below this energy. In the radiation-hydrodynamic model, the oscillation of the electron density and hence of the electron-scattering optical depth in the region of nearly radial inflow causes the X-ray spectrum to pivot about an energy that is typically of order a few keV (Miller & Lamb 1992). At this pivot energy the rms amplitude of the oscillations is a minimum and the phase difference between the oscillations at higher and lower energies is approximately 180°.

More detailed observations of bright LMXBs have shown that the phase difference between the oscillations at low and high photon energies is probably close to 150° (although 180° is within 3σ of the best estimate; see Dieters & van der Klis 1997); this may be caused by the different residence time in the region of nearly radial inflow of photons that emerge with different energies. Furthermore, observations of Sco X-1 revealed no minimum in the rms amplitude of the oscillations between $2 - 20$ keV (Dieters et al. 1997); this is probably caused by a non-negligible luminosity oscillation that may accompany the optical depth oscillation during the QPO cycle.

The identification of the normal/flaring branch QPO with radiation-hydrodynamic oscillations that occur when a source is accreting at a rate comparable to $\dot{M}_E$ provides

an additional standard candle that can be used for the determination of the accretion rates and distances of the brightest low-mass X-ray binary sources (van Paradijs & van der Klis 1994).

Kiloherz quasi-periodic oscillations.—Recent observations of many weakly magnetic accreting neutron stars have revealed QPOs in their power-density spectra with frequencies $\sim 300 - 1200$ Hz (see, e.g., van der Klis et al. 1996; Berger et al. 1996; Strohmeyer et al. 1996a; Zhang et al. 1996). These high frequencies are comparable to the inverse of the dynamical time-scale very close to the neutron star surface and therefore the properties of the kHz QPOs probe the physical conditions in the strongly curved region of the spacetime near the star.

The kilohertz QPOs typically occur in pairs, with a frequency difference that is consistent with being constant, even when the mass accretion rate onto the neutron star varies by a factor of two (Strohmeyer et al. 1996a). Moreover, nearly coherent oscillations are observed in some sources during type I X-ray bursts with frequencies that are consistent with being equal to the frequency difference of the two kHz QPOs or to its first overtone (Strohmeyer et al. 1996a; Zhang et al. 1997). Both properties can be accounted for if the higher frequency QPO in a pair is identified with the orbital frequency at a characteristic radius in the accretion disk and the lower frequency QPO in the pair is identified with the beat between this orbital frequency and the stellar spin frequency (see Miller, Lamb, & Psaltis 1997 for a discussion of the "sonic-point model" as well as of other beat-frequency models for the kilohertz QPOs).

Identifying the higher frequency QPO in a pair with an orbital frequency around the neutron star poses significant constraints on the radius of a neutron star of given mass. Moreover, requiring the radius of the Keplerian orbit to be outside the radius of the marginally stable orbit poses significant constraints on the mass of the star (Miller, Lamb, & Psaltis 1997; see also Kaaret, Ford, & Chen 1997). Both constraints can be used to significantly narrow the currently wide range of allowed equations of state for

neutron-star matter.

1.2.3 Spectral States

Soon after the discovery of QPOs it became evident that the rapid variability characteristics of a LMXB are correlated with its X-ray spectrum (van der Klis et al. 1987a, 1987b). Hasinger & van der Klis (1989) used two appropriately defined X-ray colors to characterize the spectrum of a source and found that many LMXBs can be divided into two classes, the so-called Z sources and the atoll sources, which are named after the patterns they trace out in color-color diagrams.

The Z sources are the brightest LMXBs. They accrete matter at rates that are comparable to $\dot{M}_E$, burst infrequently, and trace Z-shaped patterns in their color-color diagrams. The three branches of the Z are called the horizontal, normal, and flaring branches. They also show all three types of quasi-periodic oscillations and three types of broad-band 'noise' components in their power-density spectra. The atoll sources are fainter LMXBs that accrete matter at rates that are typically $0.01 - 0.1\dot{M}_E$. They show regular type I X-ray bursts and two types of broad-band noise, but only high-frequency (kHz) QPOs in their power spectra.

The rapid variability and bursting characteristics of both the Z and atoll sources vary, in general, systematically, continuously, and reproducibly with position on the color-color diagrams (see though Dieters & van der Klis [1997] and Wijnands et al. [1997] for possible exceptions). Moreover, when the mass accretion rate in a Z source varies, the source moves along the Z pattern in the color-color diagram without jumping between branches. These together with a variety of other properties (see van der Klis & Lamb 1997 for a review) suggest that the X-ray spectra and rapid variability characteristics of a LMXB of given magnetic field strength are determined largely by a single parameter, which is almost certainly the mass accretion rate (see though Kuulkers 1995).

1.3 X-ray Spectra of Low-Mass X-ray Binaries

Direct deconvolution—The direct deconvolution of the countrate spectra of cosmic X-ray sources measured with current X-ray detectors is still an unsolved problem. The following simplified description of the response of an X-ray detector illustrates the problems that arise when this procedure is followed.

The number of counts C_j measured in the j-th energy channel of a proportional counter can be related to the incident spectrum $S(E)$ by

$$C_j = A\Delta t \int_{E'_j}^{E'_{j+1}} \int_0^\infty R(E', E)\epsilon(E)S(E)dEdE' \,, \tag{1.1}$$

where $\epsilon(E)$ is the efficiency of the detector at energy E, $R(E', E)$ is its response function, A is its effective area, Δt is the duration of the observation, and E'_j and E'_{j+1} are the energy boundaries of channel j. The above integral relation can also be discretized and written in a matrix form as $C_j = \sum_i R_{ji}S_i$; the matrix R_{ji} is called the response matrix of the detector.

The columns of the response matrix R_{ji} are approximately Gaussian functions with a centroid energy and FWHM that varies very slowly with photon energy and hence with i (Dolan 1972). The elements of each column of the matrix R_{ji} are therefore approximately equal to the elements of the adjacent columns and hence the matrix R_{ji} is nearly singular. As a result, the numerical inversion of the response matrix and hence the simple direct deconvolution of the observed countrate spectra is a numerically unstable procedure.

Several authors have developed techniques to solve the above matrix equation without the need of inverting the response matrix of the detector (Dolan 1972; Blissett & Cruise 1979; Kahn & Blissett 1980). All of these techniques have been shown to amplify the counting errors to such a degree that they cannot be used to make quantitative estimates of the spectra of cosmic X-ray sources (see Mason et al. 1979).

Gorenstein et al. (1968) suggested an alternative method of analyzing X-ray spectra that has been widely used ever since. In this method, a model spectrum is assumed for the source and is convolved with the response of the detector. The resulting simulated countrate spectrum is then compared directly with the observations and a maximum likelihood test is used to test the initial hypothesis and to estimate the model parameters.

Spectral models.—Over the last 20 years the above technique has been used extensively in analyzing the X-ray spectra of low-mass X-ray binaries. As the energy resolution of the X-ray detectors became finer and their effective collecting areas became larger it also became evident that no simple, single component spectral model could give acceptable fits to the data (Swank & Serlemitsos 1985). A large number of model spectra with an increasing number of components and free parameters were gradually introduced to fit the X-ray spectral data (see, e.g., White et al. 1986; Mitsuda et al. 1984; Christian & Swank 1997).

The X-ray spectra of low-mass X-ray binaries can be well described by the sum of a simple power-law spectral model with a high energy exponential cut-off plus a blackbody component (see White et al. 1986; Schulz, Hasinger, & Trumper 1989; Hasinger et al. 1990; see also Schulz & Wijers 1993). The power-law spectra of these sources have been attributed to Comptonization of soft photon by hot electrons because thermal bremsstrahlung or other radiation processes are very inefficient at the electron densities and temperatures that are expected around accreting neutron stars (see Chapter 4). The weak "blackbody" components that have been introduced are probably required simply to account for the small deviations of Comptonization spectra from a simple power-law (see Lamb 1989 for a discussion).

1.4 Compton Scattering and the Spectra of Weakly Magnetic, Accreting Neutron Stars

Compton scattering of soft photons by hot electrons is thought to be the dominant spectral formation mechanism around weakly-magnetic accreting neutron stars, as discussed in the previous section. For the electron densities and temperatures that are typical of these sources photons gain, on average, energy by scattering off hot electrons.

Comptonization in static, hot media has been studied in detail, often analytically (see, e.g., Sunyaev & Titarchuk 1980) or by means of Monte Carlo simulations (see Pozdnyakov, Sobol, & Sunyaev [1983] for a review). Both approaches have shown that the exponentially decreasing distribution of escape times of photons from a scattering medium together with the exponential increase of the energy of a photon with the number of scatterings are responsible for the generation of power-law spectra with exponential cut-offs at high photon energies.

Compton scattering in moving media, such as the region of radial inflow around a neutron star that is accreting matter at a rate comparable to $\dot{M}_E$, is more complicated than the simpler case discussed above for a variety of reasons. First, even if the electrons are cold, photons can gain or loose energy by scattering off the moving electrons. Second, if the bulk velocity of the electrons is large enough, then photons may not be able to diffuse outward but may be advected inward with the flow. Finally, electron scattering tends to isotropize the photon distribution in the frame comoving with the electrons and therefore the radiation field in the system frame may be anisotropic even if the photon mean free path is much smaller than the smallest characteristic length scale in the problem.

In Chapter 2 we derive the time-dependent photon kinetic equation that describes spontaneous and induced Compton scattering as well as absorption and emission by static and moving media, the corresponding radiative transfer equation, and their

zeroth and first moments, in both the system frame and in the frame comoving with the medium. We show that it is necessary to use the correct relativistic differential scattering cross section in order to obtain a photon kinetic equation that is correct to first order in ϵ/m_e, T_e/m_e, and V, where ϵ is the photon energy, T_e and m_e are the electron temperature and rest mass, and V is the electron bulk velocity in units of the speed of light. We also demonstrate that the terms in the radiative transfer equation that are second-order in V should usually be retained, because if the radiation energy density is sufficiently large compared to the radiation flux, the effects of bulk Comptonization described by the terms that are second-order in V can be as important as the effects described by the terms that are first-order in V, even when V is relatively small. The system- and fluid-frame equations that we derive are correct to first order in ϵ/m_e. Our system-frame equations, which are correct to second order in V, may be used when V is not too large. Our fluid-frame equations, which are exact in V, may be used when $V \rightarrow 1$. Both sets of equations are valid for systems of arbitrary optical depth and can therefore be used in both the free-streaming and the diffusion regimes. We demonstrate that Comptonization by the electron bulk motion occurs whether or not the radiation field is isotropic or the bulk flow converges and that it is more important than thermal Comptonization if $V^2 > 3T_e/m_e$.

In Chapter 3 we describe a numerical algorithm for the solution of the system-frame, time-independent radiative transfer equation in spherically symmetric systems. This algorithm is a generalization of the method of variable Eddington factors (Mihalas 1980; see also Mihalas 1978, pp. 201–203), in which the radiative transfer equation and its zeroth and first moments are solved iteratively. The method provides the solution to the complete radiative transfer equation, which is therefore valid both in the diffusion and free-streaming regimes. We use this numerical algorithm in order to solve simple model problems and demonstrate the importance of the terms that are

second-order in the electron bulk velocity in calculating the X-ray spectra of accreting compact objects.

Finally, in Chapter 4, we present the results of detailed numerical calculations of the X-ray spectra of Z sources that are consistent with the models of their rapid X-ray variability. We show that electron cyclotron emission near the surface of neutron stars with magnetic fields of $10^9 - 10^{10}$ Gauss produces, when Comptonized by a hot central corona and by a cool radial inflow, X-ray spectra and color-color tracks consistent with those of the Z sources. We also suggest that the differences in the spectra and rapid variability of the different Z sources can be attributed to differences in their neutron star magnetic field strengths.

Chapter 2

Compton Scattering by Static and Moving Media: The Transfer Equation and its Moments

2.1 Introduction

Compton scattering of photons by nonrelativistic particles is thought to play an important role in many astrophysical settings, including the early universe (see Peebles 1971; Sunyaev & Zeldovich 1980), clusters of galaxies (see Rephaeli 1995), active galactic nuclei (see Mushotzky, Done, & Pounds 1993), compact galactic X- and gamma-ray sources (see Pozdnyakov, Sobol, & Sunyaev 1983), and supernova remnants (see McCray 1993). In this process photons lose energy to the electrons or gain energy from their thermal and bulk motions, as a result of Compton recoil.

Starting from the Boltzmann equation for photons, Kompaneets (1957) derived the so-called *Kompaneets equation*, which describes the time evolution of the photon energy distribution caused by scattering by thermal electrons when there is no bulk motion, the radiation field is perfectly isotropic, and the change in the energy of the photon in each scattering is small. The conditions assumed in deriving the Kompaneets equation are never strictly satisfied in astrophysical systems, since the radiation field is always anisotropic near their boundaries. In inhomogeneous systems, the radiation field may be anisotropic even in the interior. Also, in many astrophysical

systems the scattering particles have substantial bulk motions. Thus, although the Kompaneets equation has been used extensively to treat astrophysical systems, in many cases it does not give accurate results. This has motivated several authors to derive photon kinetic equations that are valid under more general conditions.

Comptonization in regions where the radiation field is anisotropic has been studied either by using Monte Carlo techniques or by solving partial differential equations for the specific intensity of the radiation field using finite-difference methods. Pozdnyakov et al. (1983) have reviewed Monte Carlo methods and results. Nagirner & Poutanen (1994) have reviewed work based on calculation of the complete Compton scattering kernel for polarized radiation. Babuel-Peyrissac & Rouvillois (1969), Pomraning (1973), Payne (1980), Madej (1989, 1991), and Titarchuk (1994) derived radiative transfer equations that describe Comptonization of an anisotropic radiation field when there is no bulk motion. Chan & Jones (1975), Blandford & Payne (1981a), and Fukue, Kato, & Matsumoto (1985) derived photon kinetic equations for thermal particles with non-zero bulk velocity, in the diffusion approximation. Thorne (1981; see also Thorne, Flammang, & Żytkow 1981) derived fluid-frame moments of the radiative transfer equation in general relativity. The equations derived by these various sets of authors have been widely used to study Comptonization by strong shocks and accretion flows onto compact objects (see, e.g., Blandford & Payne 1981b; Payne & Blandford 1981; Lyubarskij & Sunyaev 1982; Colpi 1988; Riffert 1988; Mastichiadis & Kylafis 1992; Miller & Lamb 1992; Titarchuk & Lyubarskij 1995; Turolla et al. 1997; Titarchuk, Mastichiadis, & Kylafis 1997).

In the course of our investigation of the effects of Comptonization on the X-ray spectra of accreting neutron stars (see, e.g., Lamb 1989; Miller & Lamb 1992; Psaltis, Lamb, & Miller 1995) we have rederived the radiative transfer equation and its moments for static and moving media and found important corrections to almost all the above derivations of the photon kinetic or radiative transfer equations, as we

explain in § 2.2. There we show that it is necessary to use the correct relativistic differential scattering cross section in order to obtain a photon kinetic equation that is correct to first order in ε/m_e, T_e/m_e, and V, where ε is the photon energy, T_e and m_e are the electron temperature and rest mass, and V is the electron bulk velocity in units of the speed of light (we use units in which the Boltzmann constant and the speed of light are equal to unity). In § 2.2 we also demonstrate that the terms in the radiative transfer equation that are second-order in V usually should be retained, because in many situations the second-order terms are at least as important as the first-order terms, even when V is small (see also Yin & Miller 1995). If the terms that are second-order in V are instead neglected, significant errors are introduced in the photon kinetic equation and its moments.

In § 2.3 we state our assumptions and approximations and introduce our notation. In § 2.4 we derive the time-dependent photon kinetic equation that describes spontaneous and induced scattering by static and moving media, the corresponding radiative transfer equation, and their zeroth and first angular moments, in the system frame and in the frame comoving with the medium. We derive the moment equations as well as the kinetic and transfer equations because, although it is usually necessary to solve the full radiative transfer equation in order to determine accurately the angular distribution of the radiation field, the moment equations can be used to speed up the numerical computation by a large factor (Mihalas 1980; see also Mihalas 1978, pp. 157–158) and to provide additional physical insight. The system- and fluid-frame equations that we derive are correct to first order in ε/m_e. Our system-frame equations, which are correct to second order in V, may be used when V is not too large. Our fluid-frame equations, which are exact in V, may be used when $V \rightarrow 1$. Both sets of equations are valid for systems of arbitrary optical depth and can therefore be used in both the free-streaming and the diffusion regimes. Our equations can easily be generalized to describe scattering by an arbitrary number of particle species.

In Appendix A we give the photon kinetic and radiative transfer equations that are obtained by averaging the equations for a single electron over a drifting, relativistic Maxwellian electron velocity distribution. In Appendix B we give the radiative transfer equation that describes absorption and emission in moving media, and its zeroth and first moments. There we point out that the addition of a photon source term in the transfer equation without any corresponding absorption term (see, e.g., Blandford & Payne 1981) is fundamentally inconsistent with thermodynamics and leads to a radiative transfer equation that has a different mathematical character from the thermodynamically consistent equation.

Finally, in § 2.5 we summarize our results and their implications for Comptonization by static and moving media.

2.2 Motivation

The radiative transfer equation that describes scattering of photons by particles is an integro-differential equation in which only derivatives with respect to the spatial coordinates appear (see, e.g., Nagirner & Poutanen 1994). The scattering kernel in this equation is non-local in photon energy and depends on the (possibly complicated) correlations between the angular dependence of the specific intensity of the radiation field, the velocity distribution of the particles, and the differential scattering cross section. In order to accelerate numerical calculations, gain better physical insight, and facilitate comparison with previous studies that made similar approximations, we convert this integro-differential equation into a partial differential equation over the spatial coordinates and photon energy by expanding the scattering kernel in powers of the dimensionless quantities ε/m_e, T_e/m_e, and V, which we assume are small compared to unity. In this way, the scattering kernel in the transfer equation becomes local in photon energy and the scattering integral over solid angle can be expressed in terms of the angular moments of the specific intensity of the radiation

field.

We are primarily interested in deriving a transfer equation that can be used to calculate the spectra of X-ray and soft γ-ray sources, so in expanding the scattering kernel we shall keep only terms of zeroth and first order in $\Delta\varepsilon_0/\varepsilon_0 \approx \varepsilon/m_e \ll 1$, which is the average fractional decrease in the energy of a photon in a single scattering in the electron rest frame (see eq. [2.17] below). Then, in order to obtain a radiative transfer equation of consistent accuracy, the terms in the expansion of the kernel in powers of T_e/m_e and V that are of the same size as the terms of first order in $\Delta\varepsilon_0/\varepsilon_0$, i.e., of the same size as ε/m_e, must be retained. Depending on the situation, terms of different order in T_e/m_e and V may need to be included.

We now discuss the accuracy of the expansion of the differential scattering cross section needed to obtain a transfer equation that is accurate to first order in ε/m_e, the orders of the terms in V that must be retained, and some subtle points that must be taken into account if the diffusion approximation is used.

2.2.1 Approximate Scattering Cross Section

In order to obtain a transfer equation that is consistently accurate to first order in ε/m_e, it is necessary to use the correct relativistic expression for the differential scattering cross section in the frame in which one is working. We shall work in the electron rest frame and we therefore use the Klein-Nishina expression for the differential scattering cross section (see eq. [2.16]). To first order in ε/m_e, the Klein-Nishina cross section is

$$\frac{d\sigma}{d\Omega_0} \approx \frac{3\sigma_T}{16\pi}\left[1+(\hat{l}_0\cdot\hat{l}_0')^2\right]\left[1-2\frac{\varepsilon}{m_e}(1-\hat{l}_0\cdot\hat{l}_0')\right], \qquad (2.1)$$

where σ_T is the total cross section for Thomson scattering and $\hat{l}_0$ and $\hat{l}_0'$ are the direction vectors of the photon in the electron rest frame, before and after the scattering.

Use of the Thomson approximation for the differential scattering cross section (Chan & Jones 1975; Payne 1980; Madej 1989, 1991) rather than expression (2.1)

introduces errors in the radiative transfer and moment equations of order ε/m_e, i.e., of the same size as the basic Compton effect. Neglecting the angle dependence of the term of order ε/m_e in expression (2.1) (Pomraning 1973; Blandford & Payne 1981a) introduces errors in the radiative transfer equation of this same order because, unlike the Thomson approximation, expression (2.1) is not forward-backward symmetric. Approximating expression (2.1) by the average of the cross section over the electron velocity distribution (Titarchuk 1994) neglects the effects of correlations between the angle dependence of the differential cross section, the specific intensity, and the electron velocity, introducing errors in the radiative transfer equation of order ε/m_e, T_e/m_e, and V. Finally, use in the system frame of the Thomson or Klein-Nishina expressions for the differential scattering cross section (Pomraning 1973; Payne 1980; Madej 1989, 1991) introduces errors in the transfer equation of order V and T_e/m_e, because these expressions are valid only in the electron rest frame.

2.2.2 Importance of the Terms of Order V^2

It has long been recognized that if the divergence of the electron bulk velocity is non-zero, the electron bulk motion causes a secular change in the energy of the photons (see, e.g., Chan & Jones 1975; Blandford & Payne 1981a; Fukue et al. 1985). The photon kinetic equations derived in these works do not include any terms of second order in V and predict that photons are systematically upscattered in energy by the electron bulk motion if the flow is converging. However, as we show with the examples that follow, photons are systematically upscattered by the electron bulk motion even if the terms that are first-order in V have, on average, no effect. Indeed, under some circumstances photons are systematically upscattered by the bulk motion even if the flow is *diverging*.

To see this, consider a situation in which the bulk motion of the electrons can be described as isotropic turbulence in which the velocity correlation length is much

smaller than the photon mean free path and the bulk velocity satisfies $\nabla \cdot \vec{V} = 0$. If all the terms that are first-order in V are included correctly in the photon kinetic equation but terms that are second-order in V are not included (Fukue et al. 1985), the zeroth and first moments of the kinetic equation will indicate that the electron bulk motion has no effect on the photon energy distribution on time scales longer than the velocity correlation time. In reality, however, under the conditions stated the effect of the electron turbulent motions is completely analogous to the effect of electron thermal motions, that is, the turbulent motions cause the mean energy of the photons to increase steadily with time, at a rate proportional to the second moment of the turbulent velocity field. Hence, the electron bulk motion causes the mean photon energy to increase with time even though the flow is not converging; in fact, in this case no terms that are first-order in V have any effect on the radiation field, on average. If the turbulent velocity is high enough, the terms that are second-order in V will cause the mean photon energy to increase even in a diverging flow.

Origin of terms second-order in V.—The origin of the terms in the photon kinetic equation that are second-order in V can be understood by considering a cold ($T_e = 0$) electron fluid with a uniform bulk velocity $\vec{V}$ in the system frame. For simplicity, let us analyze scattering of photons in the Thomson limit in the electron rest frame. In this limit, the angular distribution of the scattered photons is backward-forward symmetric in the electron rest frame, so the average photon energy in the system frame after scattering is $\gamma^2 (1 - \langle \hat{k} \cdot \vec{V} \rangle)$ times the energy before the scattering (see Rybicki & Lightman 1979, p. 198), where $\gamma \equiv (1 - V^2)^{-1/2}$ and the average is over the initial photon wave vectors $\vec{k}$ in the system frame. Consider first the case of a photon distribution that is isotropic in the system frame. In this case the average photon energy in the system frame after scattering is γ^2 times the energy before scattering, so in each scattering the average energy of a photon is increased by an amount of order V^2 and hence there must be terms of order V^2 in the kinetic equation that describe

this effect. In the more general case of a photon distribution that is anisotropic in the system frame these terms of order V^2 almost always produce a secular increase in the average energy of the photons, but there are also terms of order V in the kinetic equation that may cause the average energy of the photons to increase or decrease, depending on the velocity field and the angular distribution of the photons (there are generally terms of order V even if $\nabla \cdot \vec{V} = 0$; see Fukue et al. 1985).

Relative sizes of terms of different order in V.—The order in V of a given term in the various moment equations does not by itself determine whether the term should be retained in solving a given transport problem. This is because the terms of different order in V involve different angular moments of the radiation field, so the relative sizes of the moments must also be considered in determining which terms should be retained (see also Yin & Miller 1995).

For example, in the zeroth moment of the radiative transfer equation, which is a scalar equation for the energy density of the radiation field, the terms that are first-order in V involve the scalar product of the vector quantity $\vec{V}$ with the vector quantity defined by the radiation field, i.e., the radiation flux $\vec{H}$ (see eq. [2.34]). In contrast, the terms that are second-order in V do not involve $\vec{H}$ but instead involve the scalar quantity defined by the radiation field, i.e., the radiation energy density J, and the radiation stress-energy tensor K^{ij} (again see eq. [2.34]). In general, $V_i V_j K^{ij}$ is of the same size as $V^2 J$. Hence, if J is sufficiently large compared to H, the terms in the zeroth moment of the radiative transfer equation that are second-order in V are generally at least as large as the terms that are first-order in V.

In the first moment of the radiative transfer equation, which is a vector equation for the radiation flux, the situation is reversed, in that the terms that are first-order in V involve J and K^{ij} (see eq. [2.40]) whereas the terms that are second-order in V involve $\vec{H}$ and Q^{ijk}. In general, $V_j V_k Q^{ijk}$ is of the same size as $\vec{V}(\vec{V} \cdot \vec{H})$. Hence, one might be tempted to neglect the terms of order V^2 in the first moment of the

radiative transfer equation if J is large compared to H, even if the terms of order V^2 are retained in the zeroth moment equation. However, this is in general unsafe, because it involves treating the same terms in the radiative transfer equation, from which the moment equations are derived, differently, in taking the zeroth and first moment. In addressing a given transport problem, one can only determine which terms in the expansion in powers of V must be kept by considering the boundary conditions as well as the transfer equation.

The radiation field quantities that appear in terms that involve only *odd* powers of V are all of about the same size. Similarly, the radiation field quantities that appear in terms that involve only *even* powers of V are all of about the same size, although they may be much larger or smaller than the radiation field quantities that appear in the terms that involve odd powers of V. Hence, when V is $\ll 1$, terms of order V^3 and higher may be safely neglected in the derivation of the transfer equation (see also Yin & Miller 1995).

2.2.3 Use of the Diffusion Approximation

In situations in which the change during a scattering of the energy of a photon as measured in the fluid frame can be neglected and the longest photon mean free path $\lambda_{\max}$ is much smaller than the smallest length scale $L_{\min}$ on which physical variables change, the specific intensity in the frame comoving with the electron fluid, $I_f(\varepsilon)$, is given to lowest order in $\lambda_{\max}/L_{\min}$ by (see Mihalas & Mihalas 1984, p. 457)

$$I_f(\varepsilon) = J_f(\varepsilon) + 3\,\hat{l}\cdot\vec{H}_f(\varepsilon)\ , \tag{2.2}$$

where $J_f(\varepsilon)$ and $\vec{H}_f(\varepsilon)$ are the zeroth and first angular moments of $I_f(\varepsilon)$. The diffusion approximation (sometimes called the zeroth-order diffusion approximation; see Mihalas & Mihalas 1984, § 97) consists in *assuming* that $I_f(\varepsilon)$ is given *exactly* by equation (2.2). Then the first fluid-frame Eddington factor $f_f^{ij}(\varepsilon) \equiv K_f^{ij}(\varepsilon)/J_f(\varepsilon)$ is *exactly* equal to $\frac{1}{3}$; here $K_f^{ij}(\varepsilon)$ is the second moment of $I_f(\varepsilon)$. As is evident from

equation (2.2), if the source function involves only the zeroth, first, and second moments of $I_f(\varepsilon)$, then in the diffusion approximation it is only necessary to solve the three equations consisting of the zeroth and first moments of the fluid-frame radiative transfer equation and the closure relation $f_f^{ij}(\varepsilon) = \frac{1}{3}$ for the three moments $J_f(\varepsilon)$, $\vec{H}_f(\varepsilon)$, and $K_f^{ij}(\varepsilon)$; the specific intensity may then be calculated in this approximation using equation (2.2).

The moments of the specific intensity in the system frame do *not* satisfy equation (2.2), even when $\lambda_{\max}/L_{\min} \ll 1$. If expression (2.2) is mistakenly used to relate the specific intensity to its zeroth and first moments in the system frame (Blandford & Payne 1981) rather than in the fluid frame, then errors of order V will be introduced in the radiative transfer equation and its moments, even if $\lambda_{\max}/L_{\min} \ll 1$ (see Fukue et al. 1985).

If one wants to use the diffusion approximation (2.2) to solve for the moments of the specific intensity *in the system frame*, one must solve the *four* equations consisting of the zeroth and first moments of the system-frame radiative transfer equation and the two closure relations involving the first two Eddington factors for the first four moments $J(\varepsilon)$, $H^i(\varepsilon)$, $K^{ij}(\varepsilon)$, and $Q^{ijk}(\varepsilon)$ of the specific intensity $I(\varepsilon)$ in the system frame. The reason is that when equation (2.2) is boosted into the system frame and the terms that are second-order in V are retained, as in general they must be (see above), the third moment of the specific intensity $Q^{ijk}(\varepsilon)$ is introduced into the closure relation. (Fukue et al. [1985] were able to set up a closed system of equations consisting of the zeroth and first moments of the system-frame radiative transfer equation and a closure relation involving the first Eddington factor only because they neglected all the terms in the radiative transfer equation that are second-order and higher in V.)

When, as in Compton scattering, the energy of a photon in the fluid frame changes in a scattering, expression (2.2) may not be accurate for all photon energies, even if

the mean free path of a photon is independent of its energy and $\lambda_{\max}/L_{\min} \ll 1$. As an example, consider a slab that is infinite along the x and y axes but finite along the z axis, in which the electrons are cold and have no bulk motion. Suppose the slab is illuminated from one side with monochromatic photons of energy $\varepsilon_{\rm in}$ propagating in the z direction. Since the electrons are static, any photons that have scattered have lost energy to the electrons and hence no longer have energy $\varepsilon_{\rm in}$. Therefore all photons anywhere in the slab with energies equal to $\varepsilon_{\rm in}$ have never been scattered and are still propagating in the z direction. As a result, the angular distribution of these photons is not described accurately by equation (2.2), even if $\lambda_{\max}/L_{\min}$ is very small; indeed, *the Eddington factor at energy $\varepsilon_{\rm in}$ is equal to unity everywhere in the slab*. In this example, expression (2.2) is accurate only at energies sufficiently below the injection energy $\varepsilon_{\rm in}$.

The electron bulk velocity $\vec{V}$ is a vector quantity, and hence the relative sizes of the terms of first and higher order in V in the expansion of the transfer equation and its moments depend strongly on the relation between the angular dependence of the bulk velocity, the radiation field, and the differential scattering cross section. Therefore, even when the diffusion approximation is only slightly inaccurate (as for example when the Eddington factor differs only slightly from $\frac{1}{3}$), this inaccuracy produces additional terms in the moment equations that are of second order in V and that are therefore of the same magnitude as the second-order terms that would be present if the radiation field were given exactly by equation (2.2).

For these reasons we derive the radiative transfer and moment equations without making use of the diffusion approximation.

2.3 Assumptions, Definitions, and Approximations

In the sections that follow we assume that the electron gas is nondegenerate (electron occupation number $\ll 1$). For conciseness we shall refer to it as a fluid, without

implying anything about whether it is collisional or collisionless. We assume that photons are scattered only by electrons, neglecting scattering by any other particles, and set $h = c = k_B = 1$, where h is Planck's constant, c is the speed of light, and k_B is Boltzmann's constant. We indicate quantities evaluated in the rest frame of a particular electron by a subscript '0' and quantities evaluated in the inertial frame momentarily comoving (locally) with the fluid, which we call the 'fluid frame', by a subscript 'f'. The 'system frame' may be any global inertial frame (such as the frame at rest with respect to the center of mass of the system, if it is inertial). Quantities evaluated in the system frame have no subscript.

Bulk velocity and temperature.—We define the fluid frame as the frame in which the energy and momentum flux density both vanish (Landau & Lifshitz 1987, p. 505). In this frame collisions between the electrons tend to establish an isotropic velocity distribution.

The system-frame three-velocity $\vec{u}$ of a given electron is related to its fluid-frame three-velocity $\vec{u}_f$ by a Lorentz boost. The first and second moments of $\vec{u}$ in the system frame are

$$\langle \vec{u} \rangle = \vec{V} \tag{2.3}$$

and

$$\langle u^2 \rangle = \langle v^2 \rangle + V^2 \ , \tag{2.4}$$

where $\vec{V}$ is the three-velocity of the fluid as measured in the system frame and

$$\vec{v} \equiv \vec{u} - \vec{V} \tag{2.5}$$

is the peculiar velocity of an electron as measured in the system frame.

If the electron momentum distribution in the fluid frame is a relativistic Maxwellian, then the second moment of the electron velocity distribution evaluated in the fluid frame is

$$\langle u_f^2 \rangle_f = \frac{3T_e}{m_e} + \mathcal{O}\left(\frac{T_e^2}{m_e^2}\right) \tag{2.6}$$

and the second moment of the electron peculiar velocity distribution in the system frame is

$$\langle v^2 \rangle = \frac{3T_e}{m_e} + \mathcal{O}\left(\frac{T_e}{m_e}V^2\right) . \tag{2.7}$$

Description of the radiation field.—In section 4.1 and Appendix A we derive the equation that describes the evolution of a radiation field interacting with a moving electron fluid. We shall refer to this equation as the *photon kinetic equation* when it is written in terms of the photon mode occupation number and as the *radiative transfer equation* when it is written in terms of the specific intensity of the radiation field; the two descriptions are equivalent (see, e.g., Mihalas 1978, p. 32), but the radiative transfer equation is more often used in astrophysical problems.

In deriving the photon kinetic equation we shall describe the radiation field by the number $n(\hat{l}, \varepsilon)$ of photons with energy ε propagating in direction $\hat{l}$ with a given polarization state (we suppress the dependence on polarization state, because we consider only unpolarized radiation). The first few moments of $n(\hat{l}, \varepsilon)$ are

$$n \equiv \frac{1}{4\pi}\int n(\hat{l}, \varepsilon)\, d\Omega , \tag{2.8}$$

$$n^i \equiv \frac{1}{4\pi}\int n(\hat{l}, \varepsilon)\, l^i\, d\Omega , \tag{2.9}$$

$$n^{ij} \equiv \frac{1}{4\pi}\int n(\hat{l}, \varepsilon)\, l^i l^j\, d\Omega , \tag{2.10}$$

$$n^{ijk} \equiv \frac{1}{4\pi}\int n(\hat{l}, \varepsilon)\, l^i l^j l^k\, d\Omega . \tag{2.11}$$

In definitions (2.8)–(2.11) the dependence of the moments on position and photon energy have been suppressed for brevity. Here and below we display the dependence of the photon occupation number on $\hat{l}$ and ε in order to distinguish it clearly from its zeroth moment.

In writing the radiative transfer equation we shall describe the radiation field by its specific intensity $I(\hat{l}, \varepsilon) \equiv 2\varepsilon^3 n(\hat{l}, \varepsilon)$; here the factor of two accounts for the two photon polarization states. The first few moments of $I(\hat{l}, \varepsilon)$ are

$$J \equiv \frac{1}{4\pi}\int I(\hat{l}, \varepsilon)\, d\Omega = 2\varepsilon^3 n , \tag{2.12}$$

$$H^i \equiv \frac{1}{4\pi}\int I(\hat{l},\varepsilon)\, l^i\, d\Omega = 2\varepsilon^3 n^i\ , \tag{2.13}$$

$$K^{ij} \equiv \frac{1}{4\pi}\int I(\hat{l},\varepsilon)\, l^i l^j\, d\Omega = 2\varepsilon^3 n^{ij}\ , \tag{2.14}$$

$$Q^{ijk} \equiv \frac{1}{4\pi}\int I(\hat{l},\varepsilon)\, l^i l^j l^k\, d\Omega = 2\varepsilon^3 n^{ijk}\ , \tag{2.15}$$

where again we have suppressed the dependence of the moments on position and photon energy.

Compton scattering.—In the rest frame of the electron the differential cross section for scattering of unpolarized radiation is (see Berestetskiĭ, Lifshitz, & Pitaevskiĭ 1971, p. 297)

$$\frac{d\sigma}{d\Omega_0} = \frac{3\sigma_T}{16\pi}\left(\frac{\varepsilon_0'}{\varepsilon_0}\right)^2\left[\frac{\varepsilon_0}{\varepsilon_0'} + \frac{\varepsilon_0'}{\varepsilon_0} - 1 + (\hat{l}_0\cdot\hat{l}_0')^2\right]\ , \tag{2.16}$$

where σ_T is the Thomson cross section, ε_0 and $\hat{l}_0$ are the energy and direction of the incident photon, and

$$\varepsilon_o' = \frac{\varepsilon_0}{1-\frac{\varepsilon_0}{m_e}(1-\hat{l}_0\cdot\hat{l}_0')} \tag{2.17}$$

and $\hat{l}_0'$ are the energy and direction of the scattered photon.

The energy and direction of propagation of a photon in the electron rest frame are related to the same quantities in the system frame by the Lorentz transformations

$$\varepsilon_0 = \gamma\varepsilon(1-\hat{l}\cdot\vec{u}) = \frac{\varepsilon}{\gamma(1+\hat{l}_0\cdot\vec{u})} \tag{2.18}$$

and

$$\hat{l}_0 = \frac{\varepsilon}{\varepsilon_0}\left\{\hat{l} + \left[\frac{\gamma-1}{u^2}\left(\hat{l}\cdot\vec{u}\right) - \gamma\right]\vec{u}\right\}\ . \tag{2.19}$$

The photon phase-space volume is Lorentz invariant (see Mihalas 1978, p. 495), i.e.,

$$\varepsilon\, d\varepsilon\, d\Omega = \varepsilon_0\, d\varepsilon_0\, d\Omega_0\ , \tag{2.20}$$

so

$$n(\hat{l},\varepsilon) = n_0(\hat{l}_0,\varepsilon_0)\ . \tag{2.21}$$

Validity of the approximations.—In deriving the photon kinetic and radiative transfer equations and their moments in the system frame, we shall retain terms

up to first order in ε/m_e and second order in u (first order in T_e/m_e), neglecting terms of order $(\varepsilon/m_e)u$ or higher. These equations are therefore valid when

$$\frac{\varepsilon}{m_e} \ll 1 \qquad \text{and} \qquad \frac{\varepsilon}{m_e}\left(V^2 + \frac{3T_e}{m_e}\right)^{1/2} \ll \left(V^2 + \frac{3T_e}{m_e}\right) \ll 1 \,. \tag{2.22}$$

These conditions are usually satisfied in accretion onto white dwarfs and neutron stars, but are not satisfied in accretion onto black holes, because the bulk velocity $V \to 1$ at the horizon.

Our expressions for the photon kinetic and radiative transfer equations in the fluid frame are correct to all orders in V but only to first order in T_e/m_e and ε_f/m_e. These equations are therefore valid when

$$\frac{\varepsilon_f}{m_e} \ll 1 \qquad \text{and} \qquad \frac{\varepsilon_f}{m_e}\left(\frac{3T_e}{m_e}\right)^{1/2} \ll \left(\frac{3T_e}{m_e}\right) \ll 1 \tag{2.23}$$

and can be used where V is $\simeq 1$.

2.4 Photon Kinetic and Radiative Transfer Equations and their Zeroth and First Moments

2.4.1 Photon Kinetic Equation

The photon kinetic equation in the system frame is

$$\begin{aligned} k^\mu \partial_\mu n(\vec{k}) \;=\; & \int \frac{d^3k'}{(2\pi)^3} \int d^3p \Big\{ W\left(\vec{k}'\vec{p}, \vec{k}\vec{p}'\right) n(\vec{k}') \left[1 + n(\vec{k})\right] f(\vec{p}) \left[1 - f(\vec{p}')\right] \\ & - W\left(\vec{k}\vec{p}, \vec{k}'\vec{p}'\right) n(\vec{k}) \left[1 + n(\vec{k}')\right] f(\vec{p}) \left[1 - f(\vec{p}')\right] \Big\} \,, \end{aligned} \tag{2.24}$$

where $k^\mu = (\varepsilon, \varepsilon\hat{l})$, $n(\vec{k})$ is the photon occupation number, $\vec{p}$ is the electron momentum, $f(\vec{p})$ is the electron momentum distribution, $W\left(\vec{k}\vec{p}, \vec{k}'\vec{p}'\right)$ is the transition rate for the scattering $\vec{k} + \vec{p} \to \vec{k}' + \vec{p}'$, and in writing the total derivative on the left side we have used the Einstein summation convention. The left side of equation (2.24) is manifestly covariant. The ride side is also covariant, if the appropriate transition rates are used.

It is convenient to integrate first over the photon states and then over the electron states, because the angular integrals are then much simpler. We will therefore assume for the moment that all the electrons have the same momentum $\vec{p}$. Because each side of the photon kinetic equation (2.24) is covariant, the left side can be evaluated in the system frame and the right side in the electron rest frame, at the wave vector $\vec{k}_0$ that corresponds to the wave vector $\vec{k}$ of the photon in the system frame. The resulting equation for electrons moving with velocity $\vec{u} = \vec{p}/(\gamma m_e)$ is (compare with Peebles 1971, p. 204)

$$\left(\partial_t + l^i \partial_i\right) \varepsilon n(\hat{l}, \varepsilon) = \varepsilon_0 n_{e0} \int d\Omega_0' \left\{ \left(\frac{\varepsilon_0'}{\varepsilon_0}\right)^2 \frac{\partial \varepsilon_0'}{\partial \varepsilon_0} \left(\frac{d\sigma}{d\Omega'}\right)_0 n_0(\hat{l}_0', \varepsilon_0') \left[1 + n_0(\hat{l}_0, \varepsilon_0)\right] - \left(\frac{d\sigma}{d\Omega'}\right)_0 n_0(\hat{l}_0, \varepsilon_0) \left[1 + n_0(\hat{l}_0', \varepsilon_0')\right] \right\}, \quad (2.25)$$

where $\partial_t \equiv \partial/\partial t$, $\partial_i \equiv \partial/\partial x^i$, the x^i are the spatial coordinates, n_{e0} is the electron density in the electron rest frame, $\hat{l}_0$ and ε_0 are related to $\hat{l}$ and ε by equations (2.19) and (2.18), and ε_0' is related to ε_0 by equation (2.17). The factor preceding the cross section in the first term of the collision integral is the Jacobian that corrects for the different phase spaces of the incident and scattered photons.

We evaluate the collision integral in equation (2.25) by first using the Lorentz invariance of the photon occupation number to relate $n_0(\hat{l}_0', \varepsilon_0')$ to $n(\hat{l}', \varepsilon')$ and relating $n(\hat{l}', \varepsilon')$ to $n(\hat{l}', \varepsilon)$ by expanding $n(\hat{l}', \varepsilon')$ to second order in $\vec{u}$ and to first order in ε/m_e, which gives (see Peebles 1971, p. 204)

$$\begin{aligned} n_0(\hat{l}_0', \varepsilon_0') &\simeq n(\hat{l}', \varepsilon) \\ &+ \left[\left(\hat{l}_0' - \hat{l}_0\right) \cdot \vec{u} + \left(\hat{l}_0 \cdot \vec{u}\right)\left(\hat{l}_0 - \hat{l}_0'\right) \cdot \vec{u} + \frac{\varepsilon}{m_e}\left(1 - \hat{l}_0 \cdot \hat{l}_0'\right)\right] \varepsilon \partial_\varepsilon n(\hat{l}', \varepsilon) \\ &+ \frac{1}{2}\left[\left(\hat{l}_0' - \hat{l}_0\right) \cdot \vec{u}\right]^2 \varepsilon^2 \partial_\varepsilon^2 n(\hat{l}', \varepsilon), \end{aligned} \quad (2.26)$$

where $\partial_\varepsilon \equiv \partial/\partial\varepsilon$ and $\partial_\varepsilon^2 \equiv \partial^2/\partial\varepsilon^2$. We then use this result, the Lorentz invariance of the photon distribution, and $(d\sigma/d\Omega')_0$ and $n_{e0}\varepsilon_0$ expanded to second order in $\vec{u}$ to

obtain the approximate photon kinetic equation for electrons moving with velocity $\vec{u}$

$$\begin{aligned}\left(\partial_t + \hat{l}^i\partial_i\right) n(\hat{l},\varepsilon) &= \frac{3n_e\sigma_T}{16\pi}\int d\Omega_0' \left[1+\left(\hat{l}_0\cdot\hat{l}_0'\right)^2\right]\left[1-2\frac{\varepsilon}{m_e}\left(1-\hat{l}_0\cdot\hat{l}_0'\right)\right]\cdot \\ &\quad \left\{\left[1-\left(\hat{l}_0\cdot\vec{u}\right)+\left(\hat{l}_0\cdot\vec{u}\right)^2-u^2\right]\right. \\ &\quad +\left[\left(\hat{l}_0'-\hat{l}_0\right)\cdot\vec{u}+2\left(\hat{l}_0\cdot\vec{u}\right)\left(\hat{l}_0-\hat{l}_0'\right)\cdot\vec{u}\right]\varepsilon\partial_\varepsilon \\ &\quad +\frac{1}{2}\left[\left(\hat{l}_0'-\hat{l}_0\right)\cdot\vec{u}\right]^2\varepsilon^2\partial_\varepsilon^2+\frac{\varepsilon}{m_e}\left(1-\hat{l}_0\cdot\hat{l}_0'\right)(4+\varepsilon\partial_\varepsilon) \\ &\quad \left.+2\frac{\varepsilon}{m_e}\left(1-\hat{l}_0\cdot\hat{l}_0'\right)n(\hat{l},\varepsilon)(2+\varepsilon\partial_\varepsilon)\right\}n(\hat{l}',\varepsilon) \\ &\quad -n_e\sigma_T\left(1-2\frac{\varepsilon}{m_e}\right)\left(1-\hat{l}\cdot\vec{u}\right)n(\hat{l},\varepsilon)\,, \quad (2.27)\end{aligned}$$

which describes the effects of scattering by electrons with velocity $\vec{u}$.

In Appendix A we give the photon kinetic and radiative transfer equations that are obtained by averaging equation (2.27) over a drifting, relativistic Maxwellian electron velocity distribution (see eqs. [2.3]–[2.7]). The moment equations derived in the next two subsections can be obtained by computing the zeroth and first moments of the equations given in Appendix A. Here we follow the simpler approach of first computing the moments of equation (2.27) and then averaging them over the electron velocity distribution.

2.4.2 Zeroth Moment and Radiation Energy Density

We compute the zeroth moment of the photon kinetic equation by first integrating both sides of equation (2.27) over all directions. Making use of the Jacobian

$$\begin{aligned}\frac{\partial(\Omega,\Omega_0')}{\partial(\Omega_0,\Omega')} &= \left(\frac{\varepsilon_0}{\varepsilon}\frac{\partial\varepsilon_0}{\partial\varepsilon}\right)\left(\frac{\varepsilon'}{\varepsilon_0'}\frac{\partial\varepsilon'}{\partial\varepsilon_0'}\right) \\ &\simeq \left[1-2\left(\hat{l}_0\cdot\vec{u}\right)+2\left(\hat{l}'\cdot\vec{u}\right)-2u^2+3\left(\hat{l}_0\cdot\vec{u}\right)^2\right. \\ &\quad \left.+3\left(\hat{l}'\cdot\vec{u}\right)^2-4\left(\hat{l}_0\cdot\vec{u}\right)\left(\hat{l}'\cdot\vec{u}\right)\right]\,, \quad (2.28)\end{aligned}$$

we find

$$\partial_t n+\partial_i n^i = \frac{3\sigma_T}{16\pi}n_e\int d\Omega'\int d\Omega_0\left[1+\left(\hat{l}_0\cdot\hat{l}_0'\right)^2\right]\left[1-\frac{2\varepsilon}{m_e}\left(1-\hat{l}_0\cdot\hat{l}_0'\right)\right]\cdot$$

$$
\begin{aligned}
\Big[\Big\{\Big[1-3u^2+3\left(\hat{l}'\cdot\vec{u}\right)^2+2\left(\hat{l}'\cdot\vec{u}\right)\Big]+\left(\hat{l}'_0\cdot\vec{u}\right)\Big[1+2\left(\hat{l}'\cdot\vec{u}\right)\Big]\varepsilon\partial_\epsilon \\
+\frac{1}{2}\left(\hat{l}'_0\cdot\vec{u}\right)^2\varepsilon^2\partial_\epsilon^2+\frac{\varepsilon}{m_e}\Big(4+\varepsilon\partial_\epsilon\Big)\Big\} \\
-\left(\hat{l}_0\cdot\vec{u}\right)\Big\{\Big[3+6\left(\hat{l}'\cdot\vec{u}\right)\Big]+\Big[1+2\left(\hat{l}'\cdot\vec{u}\right)\Big]\varepsilon\partial_\epsilon+\left(\hat{l}'_0\cdot\vec{u}\right)\varepsilon^2\partial_\epsilon^2\Big\} \\
+\left(\hat{l}_0\cdot\vec{u}\right)^2\Big(6+4\varepsilon\partial_\epsilon+\frac{1}{2}\varepsilon^2\partial_\epsilon^2\Big)-\frac{\varepsilon}{m_e}(\hat{l}_0\cdot\hat{l}'_0)\Big(4+\varepsilon\partial_\epsilon\Big) \\
+\frac{2\varepsilon}{m_e}\left(1-\hat{l}\cdot\hat{l}'\right)n(\hat{l},\varepsilon)\Big(2+\varepsilon\partial_\epsilon\Big)\Big]\Big]\,n(\hat{l}',\varepsilon) \\
-n_e\sigma_T\left[\left(1-2\frac{\varepsilon}{m_e}\right)n-n^iu_i\right]\,. \qquad (2.29)
\end{aligned}
$$

Next we integrate over $d\Omega_0$ and then over $d\Omega'$, using definitions (2.8)–(2.11). The result is

$$
\begin{aligned}
\frac{1}{n_e\sigma_T}\left(\partial_t n+\partial_i n^i\right) &= (3+\varepsilon\partial_\epsilon)\,n^iu_i+\left[\frac{\varepsilon}{m_e}(4+\varepsilon\partial_\epsilon)+\frac{u^2}{3}\left(4\varepsilon\partial_\epsilon+\varepsilon^2\partial_\epsilon^2\right)\right]n \\
&+\left(\frac{36}{10}+\frac{34}{10}\varepsilon\partial_\epsilon+\frac{11}{20}\varepsilon^2\partial_\epsilon^2\right)\left(n^{ij}u_iu_j-\frac{1}{3}nu^2\right) \\
&+\frac{3}{2}\left(\frac{\varepsilon}{m_e}\right)\left(2n^2-2n^in^i+2n^{ij}n^{ij}-2n^{ijk}n^{ijk}\right. \\
&\left.+n\varepsilon\partial_\epsilon n-n^i\varepsilon\partial_\epsilon n^i+n^{ij}\varepsilon\partial_\epsilon n^{ij}-n^{ijk}\varepsilon\partial_\epsilon n^{ijk}\right), \qquad (2.30)
\end{aligned}
$$

where we have again used the Einstein summation convention. Finally, after averaging equation (2.30) over the electron velocity distribution we obtain the zeroth moment of the kinetic equation that describes the effects of scattering by a fluid of electrons, namely,

$$
\begin{aligned}
\frac{1}{n_e\sigma_T}\left(\partial_t n+\partial_i n^i\right) &= (3+\varepsilon\partial_\epsilon)\,n^iV_i+\frac{\varepsilon}{m_e}(4+\varepsilon\partial_\epsilon)\,n \\
&+\frac{1}{3}\left(\langle v^2\rangle+V^2\right)\left(4\varepsilon\partial_\epsilon+\varepsilon^2\partial_\epsilon^2\right)n \\
&+\left(\frac{36}{10}+\frac{34}{10}\varepsilon\partial_\epsilon+\frac{11}{20}\varepsilon^2\partial_\epsilon^2\right)\left(n^{ij}\langle v_iv_j\rangle-\frac{1}{3}n\langle v^2\rangle\right) \\
&+\left(\frac{36}{10}+\frac{34}{10}\varepsilon\partial_\epsilon+\frac{11}{20}\varepsilon^2\partial_\epsilon^2\right)\left(n^{ij}V_iV_j-\frac{1}{3}nV^2\right) \\
&+\frac{3}{2}\left(\frac{\varepsilon}{m_e}\right)\left(2n^2-2n^in^i+2n^{ij}n^{ij}-2n^{ijk}n^{ijk}\right. \\
&\left.+n\varepsilon\partial_\epsilon n-n^i\varepsilon\partial_\epsilon n^i+n^{ij}\varepsilon\partial_\epsilon n^{ij}-n^{ijk}\varepsilon\partial_\epsilon n^{ijk}\right)\,. \qquad (2.31)
\end{aligned}
$$

This equation is valid in both the diffusion and free-streaming regimes, for any arbitrary (possibly anisotropic) distribution of electron velocities.

If the electron velocity distribution in the fluid frame is a relativistic Maxwellian with temperature T_e, then (see eqs. [2.3] and [2.7])

$$\langle v_i v_j \rangle \simeq \frac{1}{3}\langle v^2 \rangle \delta_{ij} \simeq \frac{T_e}{m_e}\delta_{ij} \ , \tag{2.32}$$

and the zeroth moment of the photon kinetic equation can be written, to the same accuracy as equation (2.31), as

$$\begin{aligned}
\frac{1}{n_e \sigma_T}\left(\partial_t n + \partial_i n^i\right) &= (3+\varepsilon\partial_\varepsilon)\, n^i V_i \\
&\quad + \left[\frac{\varepsilon}{m_e}(4+\varepsilon\partial_\varepsilon) + \left(\frac{T_e}{m_e}+\frac{V^2}{3}\right)\left(4\varepsilon\partial_\varepsilon + \varepsilon^2\partial_\varepsilon^2\right)\right] n \\
&\quad + \left(\frac{36}{10}+\frac{34}{10}\varepsilon\partial_\varepsilon + \frac{11}{20}\varepsilon^2\partial_\varepsilon^2\right)\left(n^{ij}V_iV_j - \frac{1}{3}nV^2\right) \\
&\quad + \frac{3}{2}\left(\frac{\varepsilon}{m_e}\right)\left(2n^2 - 2n^i n^i + 2n^{ij}n^{ij} - 2n^{ijk}n^{ijk}\right. \\
&\quad \left. + n\varepsilon\partial_\varepsilon n - n^i\varepsilon\partial_\varepsilon n^i + n^{ij}\varepsilon\partial_\varepsilon n^{ij} - n^{ijk}\varepsilon\partial_\varepsilon n^{ijk}\right) \ ,
\end{aligned} \tag{2.33}$$

where we have used the relation $n^{ij}\delta_{ij} = n$. The corresponding zeroth moment of the radiative transfer equation with emission and absorption included (see Appendix B) is

$$\begin{aligned}
\frac{\partial J}{\partial t} + \frac{\partial}{\partial x^i}H^i &= \left\{\varepsilon\partial_\varepsilon\left[\left(\frac{\varepsilon - 4T_e}{m_e}\right)J\right] + \frac{T_e}{m_e}\varepsilon\partial_\varepsilon^2(\varepsilon J) + \varepsilon\partial_\varepsilon H^i V_i\right. \\
&\quad + \frac{V^2}{3}\left[-4\varepsilon\partial_\varepsilon J + \varepsilon\partial_\varepsilon^2(\varepsilon J)\right] \\
&\quad + \left(\frac{1}{10}\varepsilon\partial_\varepsilon + \frac{11}{20}\varepsilon^2\partial_\varepsilon^2\right)\left(K^{ij}V_iV_j - \frac{1}{3}JV^2\right) \\
&\quad + \frac{3}{4}\left(\frac{\varepsilon}{m_e}\right)\left[(\varepsilon\partial_\varepsilon J - J)\frac{J}{\varepsilon^3} - \left(\varepsilon\partial_\varepsilon H^i - H^i\right)\frac{H^i}{\varepsilon^3}\right. \\
&\quad \left.\left. + \left(\varepsilon\partial_\varepsilon K^{ij} - K^{ij}\right)\frac{K^{ij}}{\varepsilon^3} - \left(\varepsilon\partial_\varepsilon Q^{ijk} - Q^{ijk}\right)\frac{Q^{ijk}}{\varepsilon^3}\right]\right\} n_e\sigma_T \\
&\quad + \left(1 - \frac{1}{6}V^2\varepsilon\partial_\varepsilon + \frac{1}{6}V^2\varepsilon^2\partial_\varepsilon^2\right)\eta_\varepsilon \\
&\quad - \left\{\left(J + \frac{1}{2}JV^2 - H^iV_i\right) + \left[K^{ij}V_iV_j + \frac{1}{2}JV^2 - H^iV_i\right]\varepsilon\partial_\varepsilon\right. \\
&\quad \left. + \frac{1}{2}K^{ij}V_iV_j\varepsilon^2\partial_\varepsilon^2\right\}\chi_\varepsilon \ ,
\end{aligned} \tag{2.34}$$

where η_ϵ and χ_ϵ are the emission and absorption coefficients, which are defined in the fluid frame but evaluated at the energy ε of the photons in the system frame.

2.4.3 First Moment and Radiation Flux

We compute the first moment of the photon kinetic equation by multiplying both sides of equation (2.27) by $\hat{l}$ and then integrating over all directions. In performing the integration we use the transformation (2.19) and the Jacobian (2.28), integrating first over $d\Omega_0$ and then over $d\Omega'$. The result is

$$\begin{aligned}
\frac{1}{n_e\sigma_T}\left(\partial_t n^i + \partial_j n^{ij}\right) &= -n^i - \frac{2}{5}\frac{\varepsilon}{m_e}\left(1+\varepsilon\partial_\epsilon\right)n^i + \frac{1}{5}\left(-nu_i + 3n^{ij}u_j\right) \\
&\quad -\frac{1}{5}\left(8n^{ijk}u_j u_k - 2n^i u_j u_j\right) - \frac{1}{10}\left[3\varepsilon\partial_\epsilon\left(nu_i\right) + \varepsilon\partial_\epsilon\left(n^{ij}u_j\right)\right] \\
&\quad -\frac{1}{10}\left[10\varepsilon\partial_\epsilon\left(n^j u_j\right)u_i + 9\varepsilon\partial_\epsilon\left(n^{ijk}u_j u_k\right) - \varepsilon\partial_\epsilon n^i u^2\right] \\
&\quad -\frac{1}{10}\left[3\varepsilon^2\partial_\epsilon^2\left(n^j u_j\right)u_i + \varepsilon^2\partial_\epsilon^2\left(n^{ijk}u_j u_k\right)\right] \\
&\quad +\frac{3}{2}\left(\frac{\varepsilon}{m_e}\right)\left(2nn^i - 2n^j n^{ij} + 2n^{jk}n^{ijk} - 2n^{jkl}n^{ijkl}\right. \\
&\quad \left. + n^i\varepsilon\partial_\epsilon n - n^{ij}\varepsilon\partial_\epsilon n^j + n^{ijk}\varepsilon\partial_\epsilon n^{jk} - n^{ijkl}\varepsilon\partial_\epsilon n^{jkl}\right) . \qquad (2.35)
\end{aligned}$$

Averaging equation (2.35) over the electron velocity distribution, we finally obtain

$$\begin{aligned}
\frac{1}{n_e\sigma_T}\left(\partial_t n^i + \partial_j n^{ij}\right) &= -n^i - \frac{2}{5}\frac{\varepsilon}{m_e}\left(1+\varepsilon\partial_\epsilon\right)n^i \\
&\quad +\frac{3}{5}\left(n^{ij}V_j - \frac{1}{3}nV_i\right) - \frac{1}{10}\varepsilon\partial_\epsilon\left(n^{ij}V_j + 3nV_i\right) \\
&\quad -\frac{2}{5}\left(4n^{ijk}V_j V_k - n^i V_j V_j\right) \\
&\quad -\frac{1}{10}\varepsilon\partial_\epsilon\left(9n^{ijk}V_j V_k + 10n^j V_j V_i - n^i V_j V_j\right) \\
&\quad -\frac{1}{10}\varepsilon^2\partial_\epsilon^2\left(n^{ijk}V_j V_k + 3n^j V_j V_i\right) \\
&\quad -\frac{2}{5}\left(4n^{ijk}\langle v_j v_k\rangle - n^i\langle v_j v_j\rangle\right) \\
&\quad -\frac{1}{10}\varepsilon\partial_\epsilon\left(n^{ijk}\langle v_j v_k\rangle + 10n^j\langle v_j v_i\rangle - n^i\langle v_j v_j\rangle\right) \\
&\quad -\frac{1}{10}\varepsilon^2\partial_\epsilon^2\left(n^{ijk}\langle v_j v_k\rangle + 3n^j\langle v_j v_i\rangle\right) \\
&\quad +\frac{3}{2}\left(\frac{\varepsilon}{m_e}\right)\left(2nn^i - 2n^j n^{ij} + 2n^{jk}n^{ijk} - 2n^{jkl}n^{ijkl}\right.
\end{aligned}$$

$$+ n^i\varepsilon\partial_\varepsilon n - n^{ij}\varepsilon\partial_\varepsilon n^j + n^{ijk}\varepsilon\partial_\varepsilon n^{jk} - n^{ijkl}\varepsilon\partial_\varepsilon n^{jkl}\Big) \quad (2.36)$$

If the electron velocity distribution in the fluid frame is a relativistic Maxwellian with temperature T_e, then

$$n^j\langle v_j v_i\rangle = \frac{T_e}{m_e}n^i \quad (2.37)$$

and

$$n^{ijk}\langle v_j v_k\rangle = \frac{T_e}{m_e}n^i\,, \quad (2.38)$$

and the first moment of the photon kinetic equation reduces to

$$\begin{aligned}\frac{1}{n_e\sigma_T}\left(\partial_t n^i + \partial_j n^{ij}\right) &= -\left[1+\frac{2}{5}\frac{\varepsilon}{m_e}(1+\partial_\varepsilon)+\frac{2}{5}\frac{T_e}{m_e}\left(1+4\varepsilon\partial_\varepsilon+\varepsilon^2\partial_\varepsilon^2\right)\right]n^i\\ &+\frac{3}{5}\left(n^{ij}V_j-\frac{1}{3}nV_i\right)-\frac{1}{10}\varepsilon\partial_\varepsilon\left(n^{ij}V_j+3nV_i\right)\\ &-\frac{2}{5}\left(4n^{ijk}V_jV_k-n^iV_jV_j\right)\\ &-\frac{1}{10}\varepsilon\partial_\varepsilon\left(9n^{ijk}V_jV_k+10n^jV_jV_i-n^iV_jV_j\right)\\ &-\frac{1}{10}\varepsilon^2\partial_\varepsilon^2\left(n^{ijk}V_jV_k+3n^jV_jV_i\right)\\ &+\frac{3}{2}\left(\frac{\varepsilon}{m_e}\right)\left(2nn^i-2n^jn^{ij}+2n^{jk}n^{ijk}-2n^{jkl}n^{ijkl}\right.\\ &\left.+\,n^i\varepsilon\partial_\varepsilon n-n^{ij}\varepsilon\partial_\varepsilon n^j+n^{ijk}\varepsilon\partial_\varepsilon n^{jk}-n^{ijkl}\varepsilon\partial_\varepsilon n^{jkl}\right) \quad (2.39)\end{aligned}$$

The corresponding first moment of the radiative transfer equation with absorption and emission included is (again see Appendix B)

$$\begin{aligned}\partial_t H^i+\partial_j K^{ij} &= \left\{-H^i-\frac{2}{5}\left(\frac{T_e-3\varepsilon}{m_e}\right)H^i-\frac{2}{5}\left[\varepsilon\partial_\varepsilon\left(\frac{\varepsilon-4T_e}{m_e}\right)+\frac{T_e}{m_e}\varepsilon\partial_\varepsilon^2\varepsilon\right]H^i\right.\\ &+\frac{1}{10}\left[\left(9-\varepsilon\partial_\varepsilon\right)K^{ij}V_j+\left(7-3\varepsilon\partial_\varepsilon\right)JV_i\right]\\ &+\frac{1}{10}\left(-6+8\varepsilon\partial_\varepsilon-\varepsilon^2\partial_\varepsilon^2\right)H^jV_jV_i+\frac{1}{10}\left(1+\varepsilon\partial_\varepsilon\right)H^iV_jV_j\\ &-\frac{1}{10}\left(1+3\varepsilon\partial_\varepsilon+\varepsilon^2\partial_\varepsilon^2\right)Q^{ijk}V_jV_k\\ &+\frac{3}{4}\left(\frac{\varepsilon}{m_e}\right)\left[\left(\varepsilon\partial_\varepsilon J-J\right)\frac{H^i}{\varepsilon^3}-\left(\varepsilon\partial_\varepsilon H^j-H^j\right)\frac{K^{ij}}{\varepsilon^3}\right.\\ &\left.\left.+\left(\varepsilon\partial_\varepsilon K^{jk}-K^{jk}\right)\frac{Q^{ijk}}{\varepsilon^3}-\left(\varepsilon\partial_\varepsilon Q^{jkl}-Q^{jkl}\right)\frac{R^{ijkl}}{\varepsilon^3}\right]\right\}n_e\sigma_T\end{aligned}$$

$$-\left[\left(1+\frac{1}{2}V_jV_j\right)H^i-K^{ij}V_j+\left(\frac{1}{2}H^iV_jV_j-K^{ij}V_j+\right.\right.$$
$$\left.\left.\frac{1}{2}Q^{ijk}V_jV_k\right)\varepsilon\partial_\varepsilon+\frac{1}{2}Q^{ijk}V_jV_k\varepsilon^2\partial_\varepsilon^2\right]\chi_\varepsilon+\frac{1}{3}V_i\left(2-\varepsilon\partial_\varepsilon\right)\eta_\varepsilon\ , \quad (2.40)$$

where R^{ijkl} is the fourth moment of the specific intensity.

2.4.4 Equations in the Fluid Frame

The photon kinetic and radiative transfer equations as well as their moments take their simplest form in the fluid frame, since $V = 0$ in this frame, by definition. These equations can be written choosing as independent variables either Eulerian coordinates fixed in space and time or Lagrangian coordinates comoving with the fluid.

In terms of the fluid-frame coordinates, the transfer equation (A.8) and its zeroth and first moment (2.34) and (2.40) in the fluid frame become

$$\begin{aligned}\left(\partial_{t_f}+l_f^i\partial_{i_f}\right)I_f(\hat{l}_f,\varepsilon_f) &= n_{e,f}\sigma_T\Big[\mathcal{L}_1I_f(\hat{l}_f,\varepsilon_f)\\ &\quad+\frac{3}{4}\left(\mathcal{L}_2J_f+\mathcal{L}_3^iH_f^i+\mathcal{L}_4^{ij}K_f^{ij}+\mathcal{L}_5^{ijk}Q_f^{ijk}+\mathcal{L}_6^{ijkl}R_f^{ijkl}\right)\\ &\quad+\frac{3}{4\varepsilon^3}\left(\frac{\varepsilon_f}{m_e}\right)I_f(\hat{l}_f,\varepsilon_f)\left(\varepsilon_f\partial_{\varepsilon_f}-1\right)\\ &\quad\left(J_f-l_f^iH_f^i+l_f^il_f^jK_f^{ij}-l_f^il_f^jl_f^kQ_f^{ijk}\right)\Big]\ , \qquad (2.41)\end{aligned}$$

$$\begin{aligned}\partial_{t_f}J_f+\partial_{i_f}H_f^i &= n_{e,f}\sigma_T\Big\{\left[\varepsilon_f\partial_{\varepsilon_f}\left(\frac{\varepsilon_f-4T_e}{m_e}\right)+\frac{T_e}{m_e}\varepsilon_f\partial_{\varepsilon_f}^2\varepsilon_f\right]J_f\\ &\quad+\frac{3}{4}\left(\frac{\varepsilon_f}{m_e}\right)\left[\left(\varepsilon_f\partial_{\varepsilon_f}J_f-J_f\right)\frac{J_f}{\varepsilon_f^3}-\left(\varepsilon_f\partial_{\varepsilon_f}H_f^i-H_f^i\right)\frac{H_f^i}{\varepsilon_f^3}\right.\\ &\quad\left.+\left(\varepsilon_f\partial_{\varepsilon_f}K_f^{ij}-K_f^{ij}\right)\frac{K_f^{ij}}{\varepsilon_f^3}-\left(\varepsilon_f\partial_{\varepsilon_f}Q_f^{ijk}-Q_f^{ijk}\right)\frac{Q_f^{ijk}}{\varepsilon_f^3}\right]\Big\} \quad (2.42)\end{aligned}$$

and

$$\begin{aligned}\partial_{t_f}H_f^i+\partial_{j_f}K_f^{ij} &= -n_{e,f}\sigma_T\Big\{H_f^i+\frac{2}{5}\left[\left(\frac{T_e-3\varepsilon_f}{m_e}\right)+\varepsilon_f\partial_{\varepsilon_f}\left(\frac{\varepsilon_f-4T_e}{m_e}\right)\right.\\ &\quad\left.+\frac{T_e}{m_e}\varepsilon_f\partial_{\varepsilon_f}^2\varepsilon_f\right]H_f^i\end{aligned}$$

$$+\frac{3}{4}\left(\frac{\varepsilon_f}{m_e}\right)\left[\left(\varepsilon_f\partial_{\varepsilon_f}J_f - J_f\right)\frac{H_f^i}{\varepsilon_f^3} - \left(\varepsilon_f\partial_{\varepsilon_f}H_f^j - H_f^j\right)\frac{K_f^{ij}}{\varepsilon_f^3}\right.$$
$$\left. + \left(\varepsilon_f\partial_{\varepsilon_f}K_f^{jk} - K_f^{jk}\right)\frac{Q_f^{ijk}}{\varepsilon_f^3} - \left(\varepsilon_f\partial_{\varepsilon_f}Q_f^{jkl} - Q_f^{jkl}\right)\frac{R_f^{ijkl}}{\varepsilon_f^3}\right]\Bigg\}, \tag{2.43}$$

where the coefficients $\mathcal{L}_1$–$\mathcal{L}_6$, which are given in Appendix A, are to be evaluated at $V = 0$.

The left sides of the above equations can also be written in terms of the system-frame Eulerian coordinates as in equations (95.9), (95.11), and (95.12) of Mihalas & Mihalas (1984). The resulting equations, which are often called *mixed-frame* equations, are correct to all orders in V and therefore can be used in situations where the bulk velocity is relativistic. The velocity-dependent terms that appear in the mixed-frame equations arise from Lorentz transformation of the left sides of equations (2.41)–(2.43), whereas the velocity-dependent terms that appear in the system-frame equations arise from Lorentz transformation of the scattering integral on the right sides of these equations.

The right side of the radiative transfer equation (2.41), can also be used in the formalism developed by Thorne (1981), for solving Comptonization problems in general relativity (compare eqs. [6.10] and [6.13] of Thorne 1981).

2.5 Discussion

In the previous section we derived the radiative transfer equation in both the system and fluid frames, taking into account absorption and emission as well as spontaneous and induced Compton scattering. In this section, we first show that our equation reduces to the Kompaneets equation in the appropriate limits and call attention to several errors and misunderstandings in the literature. Next, we discuss the moment equations for an anisotropic radiation field in a static medium and show that the radiation force, and hence the critical flux and luminosity, generally depend on both the

photon energy spectrum and the electron temperature. We then consider the equation for the zeroth moment of the specific intensity for moving media and show that if the radiation field is isotropic, the terms in the transfer equation that are second-order in the electron bulk velocity produce a systematic increase in the energy of the photons that is completely analogous to the systematic increase in the energy of the photons produced by the electron thermal motions. We also show that Comptonization by electron bulk motion occurs, whether or not the radiation field is isotropic or the bulk flow converges, and give estimates for the time scales on which the photon energy distribution changes because of systematic downscattering and upscattering caused by the electron thermal and bulk motions. We derive a new, more general condition for determining when Comptonization by the electron bulk motion is more important than Comptonization by the electron thermal motions. We conclude by indicating how the transfer equations we have derived can be solved using the method of variable Eddington factors.

2.5.1 The Kompaneets Equation

When the radiation field is isotropic and there is no bulk velocity and no absorption or emission, equation (2.34) reduces to the Kompaneets (1957) equation[1]

$$\partial_{t_c} J = \frac{\varepsilon}{m_e}\partial_\varepsilon(\varepsilon J) - \frac{4T_e}{m_e}\varepsilon\partial_\varepsilon J + \frac{T_e}{m_e}\varepsilon\partial_\varepsilon^2(\varepsilon J) + \frac{\varepsilon}{m_e}(\varepsilon\partial_\varepsilon J - J)\frac{J}{\varepsilon^3}\,, \qquad (2.44)$$

where on the left side we have introduced the differential Compton time $dt_c \equiv n_e\sigma_T dt$. The first two terms on the right side of equation (2.44) describe the effects of systematic downscattering and upscattering of the photons by electrons. The third term

[1]In their derivations of the Kompaneets equation, Rybicki & Lightman (1979, p. 213) and Katz (1987, pp. 100–114) did not take into account in the collision integral the different phase spaces of the incident and scattered photons. However, following Kompaneets they evaluated the integral by using photon conservation and the thermodynamic equilibrium photon distribution rather than by performing the integration directly and thereby obtained the correct result despite this error. These authors also used the Thomson approximation to the Klein-Nishina cross section. In general this introduces an error of the same size as the systematic downscattering term (see below), but this error vanishes if the photon distribution is isotropic.

describes the diffusion in energy produced by the thermal motion of the electrons. The last term describes the effect of induced Compton scattering.

As noted by Kompaneets (1957), *any* Bose-Einstein distribution is a stationary solution of equation (2.44). Induced Compton scattering cannot change the chemical potential, because it does not change the number of photons. Hence, the statement by Pomraning (1973, p. 193; see also Rybicki & Lightman 1979, p. 209) that the Planck spectrum (the particular Bose-Einstein distribution with zero chemical potential) is the only stationary solution of the Kompaneets equation if induced scattering is included is not correct. Integrating equation (2.44) over energy shows that if the electron temperature is equal to the Compton temperature

$$T_{\rm C} \equiv \frac{\langle \varepsilon^2 \rangle - \langle n\varepsilon^2 \rangle}{4\langle \varepsilon \rangle} , \tag{2.45}$$

the photon energy density remains constant although the photon spectrum may evolve with time; here the average is over photon energy, using the photon-number density $N(\varepsilon) \equiv (J/\varepsilon)$ as the weighting function. Note that, for a given photon spectrum, induced Compton scattering *always decreases* the Compton temperature.

2.5.2 Implications of the Moment Equations for Static Media

As we mentioned in the Introduction, the Kompaneets equation (2.44) is not strictly valid for astrophysical systems, since it requires the radiation field to be isotropic and hence that no radiation leaves the system. If the radiation field is anisotropic but there is no bulk motion, the system of equations

$$\begin{aligned} \partial_t J + \partial_i H^i &= \eta - \chi J \\ &\quad + n_e \sigma_T \left[\varepsilon \partial_\varepsilon \left(\frac{\varepsilon - 4T_e}{m_e} \right) + \frac{T_e}{m_e} \varepsilon \partial_\varepsilon^2 \varepsilon \right] J \end{aligned} \tag{2.46}$$

and

$$\begin{aligned} \partial_t H^i + \partial_j K^{ij} &= -n_e \sigma_T H^i - \chi H^i \\ &\quad - \frac{2}{5} n_e \sigma_T \left[\left(\frac{T_e - 3\varepsilon}{m_e} \right) + \varepsilon \partial_\varepsilon \left(\frac{\varepsilon - 4T_e}{m_e} \right) + \frac{T_e}{m_e} \varepsilon \partial_\varepsilon^2 \varepsilon \right] H^i \end{aligned} \tag{2.47}$$

must be solved simultaneously together with closure relations for K^{ij} and J, which are usually introduced as variable Eddington factors (see Mihalas 1978, p. 157). For simplicity, we have neglected the effects of induced Compton scattering in equations (2.46) and (2.47). The term $(2n_e\sigma_T/5)[(T_e - 3\varepsilon)/m_e]H^i$ does not appear in the first moment of the transfer equation derived by Chan & Jones (1975), Payne (1980), and Madej (1989, 1991), because these authors did not use the appropriate relativistic scattering cross section.

In a static medium and in the absence of absorption, emission, and induced scattering, F^i, the radiation force per unit volume on the electrons (see also Miller & Lamb 1995) can be obtained by integrating equation (2.47) over photon energy, which gives

$$F^i = \frac{4\pi}{c} n_e \sigma_T \left(1 - \frac{8}{5}\frac{\langle\varepsilon\rangle_{H^i}}{m_e} + 2\frac{T_e}{m_e}\right) \int_0^\infty H^i \, d\varepsilon \ , \tag{2.48}$$

where $\langle\varepsilon\rangle_{H^i}$ is the average photon energy, using H^i as the weighting function. Blandford & Payne (1981a) neglected the terms in the square brackets on the right side of equation (2.47) and therefore the radiation force given by their equation is incorrect to first order in ε/m_e and T_e/m_e. Equation (2.48) shows that the volume radiation force on the electrons produced by Compton scattering of the photons is different from that obtained in the Thomson limit, and depends both on the photon spectrum and on the electron temperature (see also Fukue et al. 1985). Hence, to first order in ε/m_e and T_e/m_e, the energy-integrated critical radial radiation flux $\mathcal{F}^{\rm crit}$ that produces a radially outward radiation force which exactly balances the inward gravitational force of a massive object depends on the photon spectrum and the electron temperature. For a completely ionized hydrogen gas, the critical radiation flux at radius r is given implicitly by the equation

$$\mathcal{F}^{\rm crit} = \frac{cm_pGM}{r^2\sigma_T} \left(1 - \frac{8}{5}\frac{\langle\varepsilon\rangle_{\mathcal{F}_\varepsilon^{\rm crit}}}{m_e} + 2\frac{T_e}{m_e}\right)^{-1} \ , \tag{2.49}$$

where m_p is the proton mass, M is the mass of the object, and $\langle\varepsilon\rangle_{\mathcal{F}_\varepsilon^{\rm crit}}$ is the average photon energy, using $\mathcal{F}_\varepsilon^{\rm crit}$ as the weighting function. For example, in the spectral

formation region of many neutron-star low-mass X-ray binaries, $\langle\varepsilon\rangle_{\mathcal{F}_e^{\rm crit}}$ is ~ 1 keV and T_e can be ~ 25 keV (Miller & Lamb 1992; Psaltis et al. 1995), in which case the critical flux is $\sim 10\%$ smaller than the usual Eddington critical flux computed assuming Thomson scattering. Note also that to this order the critical luminosity $L_{\rm crit} \equiv 4\pi r^2 \mathcal{F}^{\rm crit}$ generally depends on radius, because both $\langle\varepsilon\rangle_{\mathcal{F}_e^{\rm crit}}$ and T_e generally depend on radius.

2.5.3 Implications of the Moment Equations for Moving Media

Consider now a medium in which the electron bulk velocity is not zero. Suppose first, for simplicity, that the radiation field is isotropic in the *system* frame. To make this situation concrete, consider a thought experiment in which electrons are moving with uniform and constant bulk velocity $\vec{V}$ through a box with sides of length L. The electrons are assumed to be able to pass through the walls of the box whereas photons are confined inside the box and have a mean free path much larger than L. Under these conditions, scattering of photons by the walls of the box, which is much more frequent than scattering of photons by the electrons, keeps the photon distribution nearly isotropic.

In this situation the equation for the zeroth moment of the specific intensity reduces to

$$\partial_{t_c} J = \frac{\varepsilon}{m_e}\partial_\varepsilon(\varepsilon J) + \left(\frac{T_e}{m_e} + \frac{V^2}{3}\right)\left(-4\varepsilon\partial_\varepsilon + \varepsilon\partial_\varepsilon^2\varepsilon\right) J \,, \tag{2.50}$$

where for simplicity we have neglected absorption, emission, and induced scattering. Equation (2.50) shows that when the radiation field is isotropic in the system frame, Comptonization by the bulk motion of the electrons is described entirely by terms that are second-order in V; all terms that are first-order in V vanish identically.

Suppose now that (i) photons with energies $\varepsilon \ll T_e + \frac{1}{3}m_e V^2$ are injected into the box with an isotropic momentum distribution, (ii) the photons are allowed to remain

in the box for a distribution of residence times that decreases exponentially with the residence time, and (iii)

$$y_b \equiv 4\left(\frac{T_e}{m_e} + \tfrac{1}{3}V^2\right)\bar{t}_{\rm res} \lesssim 1\ , \tag{2.51}$$

where $\bar{t}_{\rm res}$ is the mean residence time measured in units of the Compton time $(1/n_e\sigma_T)$. The solution of equation (2.50) is then a power-law spectrum with a high-energy cutoff. At high and low energies the spectrum is

$$J \;=\; \begin{cases} \varepsilon^{3+\alpha}\ , & \varepsilon \ll T_e + \frac{1}{3}m_eV^2\ , \\ \varepsilon^3\exp[-\varepsilon/(T_e+\frac{1}{3}V^2)]\ , & \varepsilon \gg T_e + \frac{1}{3}m_eV^2\ , \end{cases} \tag{2.52}$$

where

$$\alpha \equiv -\frac{3}{2} - \sqrt{\frac{9}{4} + \frac{4}{y_b}}\ . \tag{2.53}$$

and the factor ε^3 arises because we are considering the energy density rather than the photon occupation number. This solution is a simple generalization of the solution to the Kompaneets equation obtained by Shapiro, Lightman & Eardly (1976; see also Rybicki & Lightman 1979, Ch. 7) and shows that *the terms in the transfer equation that are second-order in the electron bulk velocity produce a systematic increase in the energy of the photons that is completely analogous to the systematic increase in the energy of the photons produced by the electron thermal motions.* In treating astrophysical systems, the mean residence time $\bar{t}_{\rm res}$ in equation (2.51) is often expressed in terms of τ^2, where τ is the electron scattering optical depth of the system.

When the photon momentum distribution is not perfectly isotropic, the characteristic time scales on which the photon distribution changes because of systematic downscattering and Comptonization by the electron thermal and bulks motions are (see eq. [2.34])

$$t_{\rm down}^{-1} \;\sim\; n_e\sigma_T\left(\frac{\varepsilon}{m_e}\right)\ , \tag{2.54}$$

$$t_{\rm th}^{-1} \;\sim\; n_e\sigma_T\left(\frac{4T_e}{m_e}\right)\ , \tag{2.55}$$

$$t_{\rm V}^{-1} \sim n_e \sigma_T \vec{V} \cdot \left(\frac{\vec{H}}{J} \right) , \tag{2.56}$$

$$t_{\rm V^2}^{-1} \sim n_e \sigma_T \left(\frac{4V^2}{3} \right) , \tag{2.57}$$

where the last two time scales have been estimated from the terms that are first- and second-order in V.

Comparison of rates (2.55) and (2.57) shows that Comptonization by the electron bulk motion is more important than Comptonization by the electron thermal motion if

$$V^2 > \frac{3T_e}{m_e} . \tag{2.58}$$

In fact, Comptonization by the bulk motion occurs whether or not the radiation field is isotropic or the bulk motion converges (see also eq. [2.50]), contrary to the impression given by Blandford & Payne (1981a). Comparison of rates (2.56) and (2.57) shows that *if J is sufficiently large compared to $H^{\rm i}$, the effects of bulk Comptonization described by the terms that are second-order in V are dominant compared to the effects described by the terms that are first-order in V.*

In estimating the characteristic time scale for bulk Comptonization, Blandford & Payne (1981a; see also Blandford & Payne 1981b and Payne & Blandford 1981) used only one of the several terms in their equation that are first-order in V, neglecting other terms that generally also produce systematic upscattering or downscattering of photons. As a result, the characteristic time scale that they obtained for bulk Comptonization is proportional to $(\nabla \cdot \vec{V})/3$, which they assumed to be proportional to $n_e \sigma_T V^2/3$. This assumption is not generally valid. When it is, their expression suggests that bulk Comptonization is less important than thermal Comptonization if $V^2 < 12T_e/m_e$. However, comparison of rates (2.55)–(2.57) shows that the bulk Comptonization terms that are second-order in V are already as important as the thermal Comptonization terms when $V^2 \sim 3T_e/m_e$ and hence that these terms can be more important than the thermal terms even if $V^2 < 12T_e/m_e$.

2.5.4 A Method of Solving the Transfer Equation for Moving Media

In more realistic models, the radiation field is not isotropic in the system frame in the presence of bulk motion (see, e.g., Miller & Lamb 1993, 1996) because electron scattering tends to isotropize the photon distribution in the *fluid* frame. In this case, the full radiative transfer equation must be solved. This can be done using the method of variable Eddington factors (Mihalas 1980; see also Mihalas 1978, pp. 201–203), in which the radiative transfer equation and its zeroth and first moments are solved iteratively. In this approach, the second and higher moments of the specific intensity are related to the zeroth and first moments via variable Eddington factors. The zeroth and first moments of the radiative transfer equation are then solved using initial guesses for the variable Eddington factors and the source function is computed from the calculated moments of the specific intensity. The radiative transfer equation is then solved, the Eddington factors are updated, and the whole procedure is repeated until convergence is achieved.

A detailed study of the solutions of the equations derived here for realistic models of astrophysical systems are discussed in Chapters 3 and 4.

Chapter 3

Compton Scattering by Static and Moving Media: Solutions for Spherically Symmetric Systems

3.1 Introduction

Compton scattering of photons by electrons with non-zero thermal and bulk velocities is the dominant radiation process in several astrophysical systems. In particular, Comptonization in quasi-spherical coronae and accretion flows is thought to be responsible for the X-ray spectra of many accreting compact objects. For example, the hard X-ray spectra of weakly-magnetic accreting neutron stars can be naturally explained if a spherical hot corona surrounds the neutron star and inner accretion disk (see, e.g., Lamb 1989; Psaltis, Lamb & Miller 1995). The spectral signature of isolated neutron stars accreting from the interstellar medium, which is required for their positive identification, is determined mainly by the efficiency of Compton upscattering of thermal photons emitted from the stellar surfaces (see, e.g., Zampieri et al. 1995). Moreover, Compton scattering in advection-dominated accretion disks plays a major role in the formation of the high-energy spectra of accreting black holes (see, e.g., Narayan, McClintock, & Yin 1995). A variety of related phenomena have also been attributed to Compton scattering in quasi-spherical regions around *compact objects, such as the strong photon-energy dependence of the amplitudes of*

quasi-periodic oscillations with low ($\sim 6 - 15$ Hz) and high ($\gtrsim$200 Hz) frequencies observed from various low-mass X-ray binaries (Miller & Lamb 1992; Miller, Lamb & Psaltis 1997), as well as the microsecond time lags between high-frequency ($\sim$ 800 Hz) quasi-periodic oscillations observed at different photon energies (Vaughan et al. 1997).

Comptonization in static and moving media has been studied either by using Monte Carlo simulations or by solving partial differential equations for the specific intensity of the radiation field using finite-difference methods. Monte Carlo methods and results have been reviewed by Pozdnyakov, Sobol, & Sunyaev (1983) and will not be discussed here.

Over the last twenty five years several authors have derived the photon kinetic or radiative transfer equation and their moments for Compton scattering in static and moving media (see, e.g., Kompaneets 1957; Babuel-Peyrissac & Rouvillois 1969; Pomraning 1973; Chan & Jones 1975; Payne 1980; Blandford & Payne 1981a; Thorne 1981; Fukue, Kato, & Matsumoto 1985; Madej 1989, 1991; Titarchuk 1994). The moment equations derived by these various sets of authors have been widely used in studies of Comptonization by static media (see, e.g., Katz 1976; Shapiro, Lightman, & Eardly 1976; Sunyaev & Titarchuk 1980) or by strong shocks and accretion flows onto compact objects (see, e.g., Blandford & Payne 1981b; Payne & Blandford 1981; Lyubarskij & Sunyaev 1982; Colpi 1988; Riffert 1988; Mastichiadis & Kylafis 1992; Titarchuk & Lyubarskij 1995; Turolla et al. 1996; Titarchuk, Mastichiadis, & Kylafis 1997), either under the diffusion approximation or with closure relations that were specified a priori. Most of the above analyses of Compton scattering by moving media were performed in the system frame and to first order in the electron bulk velocity. Recently, Zane et al. (1996) developed a numerical algorithm for solving radiative transfer problems by integrating the general-relativistic radiative transfer equation for Compton scattering along characteristics without the need for specifying a priori closure relations.

In Paper I (Psaltis & Lamb 1997; see also Chapter 2) of this series we derived the time-dependent photon kinetic and radiative transfer equations and their zeroth and first moments that describe absorption and emission as well spontaneous and induced Compton scattering in static and moving media, correcting various errors in the literature. The system-frame equations that we derived are valid to first order in ϵ/m_e and T_e/m_e, and to *second* order in V, where m_e and T_e are the electron mass and temperature, ϵ is the photon energy, and V is the bulk velocity of the electrons. The fluid-frame equations that we derived are valid for arbitrary values of the bulk velocity V. Using these equations we demonstrated in Paper I that the effects of Comptonization by the bulk electron velocity that are described by the terms that are second-order in V can become at least as important as the effects described by the terms that are first-order in V, even when V is small, and hence these second-order terms should generally be retained (see also Yin & Miller 1995).

In this chapter, we describe a numerical algorithm for the solution of time independent radiative transfer problems in systems with spherical symmetry. This algorithm is a generalization of the method of variable Eddington factors (Mihalas 1980; see also Mihalas 1978, p. 157–158) and provides the solution to the radiative transfer equation in the system frame. It is therefore accurate for systems of arbitrary optical depth and does not require a priori specification of closure relations. The algorithm is based on the iterative solution of both the transfer equation and the systems of its first two moments and hence the validity and accuracy of the solution can be verified at the end of each run. The method also requires a small number of iterations in order to converge to the solution and is therefore ideal for future extensions to time-dependent and multi-dimensional transport problems.

In §3.2, we summarize the results from Paper I and in §3.3 we present the numerical algorithm. In §3.4 we solve simple model problems in order to understand the physical origin of the various terms in the radiative transfer equation as well as their effects

on the emerging photon spectra and in §3.5 we briefly discuss our results and their implications for the spectral models of accreting compact objects.

3.2 The Electron Gas and Radiation Field

Units.—Throughout this chapter we set $h = k_B = c = 1$, where h is Planck's constant, k_B is Boltzmann's constant, and c is the speed of light. We also normalize all the spatial coordinates to the inner radius of the flow, the electron temperature T_e and photon energy ϵ to the electron rest mass m_e, and the electron density n_e to its value at the inner radius of the flow. Finally, we normalize the emission and absorption coefficients $\eta(r, \epsilon)$ and $\chi(r, \epsilon)$ to the inverse of the electron scattering mean-free path in the Thomson limit.

The electron gas.—In this chapter we assume that photons are scattered only by electrons and that the electrons are non-degenerate (electron occupation number $\ll 1$).

Let $\vec{u}$ be the system-frame three-velocity of a given electron. We define the local bulk velocity $\vec{V}$ of the electrons as measured in the system frame as

$$\vec{V} \equiv \langle \vec{u} \rangle \, , \tag{3.1}$$

where the sharp brackets indicate the average over the local electron velocity distribution in the system frame. We also assume that the electron velocity distribution in the fluid frame is a relativistic Maxwellian and therefore

$$\langle u^2 \rangle \simeq V^2 + 3T_e/m_e \, , \tag{3.2}$$

where we have neglected terms of order $V^2 T_e$ and higher.

The radiation field.—We describe the radiation field at any position in the system frame with coordinate vector $\vec{r}$ using the monochromatic specific intensity $I(\vec{r}, \hat{l}, \epsilon)$, where $\hat{l}$ is the direction of propagation and ϵ is the photon energy. Here we consider

only unpolarized radiation and hence we have suppressed the dependence of the specific intensity on polarization. Because of the assumed spherical symmetry of the problem the radiation field depends only on the radial distance from the center of symmetry (i.e., the r–component of the vector $\vec{r}$), on the angle θ between the radial direction and the direction of propagation (i.e., $\cos\theta = \hat{l} \cdot \vec{r}/r$), and on the photon energy ϵ.

We define the first five moments of the monochromatic specific intensity as

$$J(\vec{r},\epsilon) \equiv \frac{1}{4\pi}\int_\Omega I(\vec{r},\hat{l},\epsilon)d\Omega \tag{3.3}$$

$$H^i(\vec{r},\epsilon) \equiv \frac{1}{4\pi}\int_\Omega I(\vec{r},\hat{l},\epsilon)l^i d\Omega \tag{3.4}$$

$$K^{ij}(\vec{r},\epsilon) \equiv \frac{1}{4\pi}\int_\Omega I(\vec{r},\hat{l},\epsilon)l^i l^j d\Omega \tag{3.5}$$

$$Q^{ijk}(\vec{r},\epsilon) \equiv \frac{1}{4\pi}\int_\Omega I(\vec{r},\hat{l},\epsilon)l^i l^j l^k d\Omega \tag{3.6}$$

$$R^{ijkl}(\vec{r},\epsilon) \equiv \frac{1}{4\pi}\int_\Omega I(\vec{r},\hat{l},\epsilon)l^i l^j l^k l^l d\Omega\ . \tag{3.7}$$

The non-zero components of the first five moments of the specific intensity for systems with spherical symmetry are given in Appendix C.

The transfer equation and its moments—Following Mihalas (1980; see also Mihalas 1978) we solve the radiative transfer equation in a plane that contains the center of symmetry of the system between the inner and outer radii $r_{\rm in}$ and $r_{\rm out}$ of the flow, using the coordinate system shown in Figure 3.1 and the coordinates $z \equiv r\cos\theta$ and $p \equiv r\sin\theta$.

The radiative transfer equation along a ray of constant coordinate p is

$$\pm\frac{\partial}{\partial\tau_z}I^\pm(z,p,\epsilon) = (1-2\epsilon)I^\pm(z,p,\epsilon) - S^\pm(z,p,\epsilon)\ , \tag{3.8}$$

where the signs '+' and '−' correspond to the equations for the outgoing and incoming rays respectively and we have neglected the effects of induced Compton scattering. In equation (3.8) we have used the optical depth along the ray defined as $d\tau_z \equiv -n_e\sigma_T[1+\chi(r,z,\epsilon)]dz$, where $\tau_z = 0$ at the outer boundary and σ_T is the angle-integrated Thomson scattering cross section. $S^\pm(z,p,\epsilon)$ is the generalized source

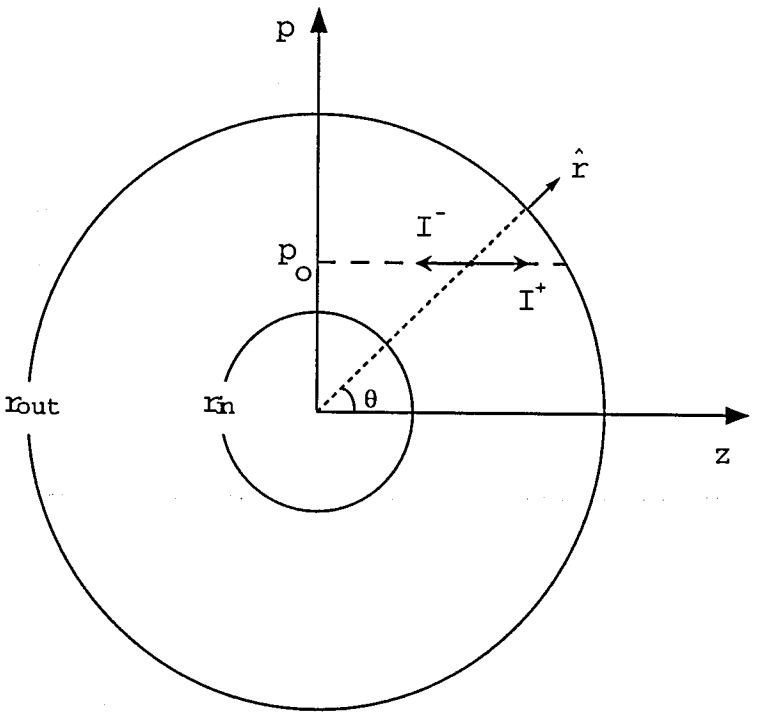

Figure 3.1: The system of coordinates used for solving the radiative transfer equation.

function for absorption, emission, and Compton scattering in systems with spherical symmetry and is given in Appendix D.

The equations for the moments of the specific intensity can be derived either directly from equation (3.8) or from equations (34) and (40) of Paper I (eqs. [2.34] and [2.40] in Chapter 2). Written in compact form and using the dimensionless quantities defined above, the moment equations are

$$A_1 J + A_2 \epsilon \partial_\epsilon J + A_3 \epsilon^2 \partial_\epsilon^2 J + A_4 H^r + A_5 \epsilon \partial_\epsilon H^r + \partial_{\tau_r} H^r = C1 \qquad (3.9)$$

$$B_1 J + B_2 \epsilon \partial_\epsilon J + f^{rr} \partial_{\tau_r} J + B_3 H^r + B_4 \epsilon \partial_\epsilon H^r + B_5 \epsilon^2 \partial_\epsilon^2 H^r = C2\,, \qquad (3.10)$$

where $\partial_\epsilon \equiv \partial/\partial\epsilon$, $\partial_\epsilon^2 \equiv \partial^2/\partial\epsilon^2$, $\partial_{\tau_r} \equiv \partial/\partial\tau_r$, and $\tau_r \equiv -\sigma_T n_e(r_{\rm in})(r - r_{\rm out})$. When the electron density is uniform, then the dimensionless quantity τ_r is equal to the electron scattering optical depth in the radial direction measured from $r_{\rm out}$. The coefficients in equations (3.9) and (3.10) are given in Appendix E.

In Appendix F we show that the system of partial differential equations (3.9) and

(3.10) is parabolic.

Boundary Conditions.—The boundary conditions for both the transfer equation and the system of its moments depend on the specific problem under study. For the model problems discussed in section 3.5, we shall assume that the flow is not illuminated from the outside, i.e.,

$$I^{-}(r_{\rm out},\theta,\epsilon) = 0 \tag{3.11}$$

at the outer boundary, and specify the radiation flux at the inner boundary, i.e.,

$$I^{+}(r_{\rm in},\theta,\epsilon) = I^{-}(r_{\rm in},\theta,\epsilon) + 4H_0^r(\epsilon)\,. \tag{3.12}$$

For solving the moments of the radiative transfer equation we shall specify, for all photon energies ϵ, the first moment of the monochromatic specific intensity at the inner radius, i.e.,

$$H^r(r_{\rm in},\epsilon) = H_0^r(\epsilon) \tag{3.13}$$

as well as the ratio of the first to the zeroth moment of the monochromatic specific intensity at the outer radius

$$\frac{H^r(r_{\rm out},\epsilon)}{J(r_{\rm out},\epsilon)} = k(\epsilon)\,. \tag{3.14}$$

We shall also set at all radii

$$\lim_{\epsilon\to 0} J(r,\epsilon) = \lim_{\epsilon\to\infty} J(r,\epsilon) = 0 \tag{3.15}$$

$$\lim_{\epsilon\to 0} H^r(r,\epsilon) = \lim_{\epsilon\to\infty} H^r(r,\epsilon) = 0 \tag{3.16}$$

3.3 Numerical Method

Equation (3.8) is an integro-differential equation for the specific intensity of the radiation field and therefore any numerical solution of this equation is not trivial to obtain. On the other hand, the system of equations (3.9) and (3.10) depends on two variable Eddington factors and an unknown outer boundary condition, which can be

computed only when the solution of equation (3.8) for the specific intensity is obtained. Here, we employ a numerical algorithm that is a generalization of the method of variable Eddington factors (Mihalas 1980; see also Mihalas 1978, pp. 157–158) in order to solve iteratively equation (3.8) for the specific intensity of the radiation field and the system of partial differential equations (3.9) and (3.10) for its zeroth and first moments. This algorithm has proven to be very efficient and gives a solution to the complete transfer equation that is limited only by numerical accuracy, independent of the optical depth of the medium.

In this method, we first solve the moments of the transfer equation using an initial guess for the variable Eddington factors and for the outer boundary condition. We then compute the generalized source function using the calculated moments of the specific intensity, solve the radiative transfer equation, and use this solution to update the Eddington factors. We repeat the whole procedure until convergence is achieved.

3.3.1 Solution of the Moments of the Transfer Equation

The moments of the transfer equation depend only on radius and photon energy, when the variable Eddington factors are known. Therefore, we need to discretize the domain of solution and the differential operators of equations (3.9) and (3.10) on a two–dimensional mesh of N_τ grid points over the variable τ_r and N_{En} grid points over the photon energy ϵ.

The mesh of discrete grid points over the variable τ_r must resolve the rapid change of the variable Eddington factors with optical depth near the boundaries of the domain of solution. In order to achieve this, we define the mesh points to be equidistant in the quantity

$$Q = \begin{cases} W\tau + (1-W)\log\tau\,, & \tau \le \frac{1}{2}\tau_m \\ W\left(\tau_m - \tau\right) + (1-W)\log\left(\tau_m - \tau\right) & \tau \ge \frac{1}{2}\tau_m \end{cases}\,, \qquad (3.17)$$

where τ is the optical depth (and not the quantity τ_r) in the radial direction measured from $r_{\rm out}$, $\tau_m \equiv \tau(r_{in})$ is the maximum radial optical depth in the medium, and W

is a dimensionless parameter that allows us to combine a logarithmic grid near the boundaries with a linear grid in the interior. Because the spectra that emerge from Comptonizing media are often close to power laws, we shall use a logarithmic mesh of discrete grid points over photon energy ϵ.

Let F_{ij} be the value of a physical quantity (e.g., J, H^r, f^{rr}, or g^{rr}) at the i–th grid point in the variable τ_r and at the j–th grid point in photon energy. For all the interior grid points, in discretizing the zeroth moment of the transfer equation we approximate the first derivative of the quantity F with respect to the variable τ_r using the relation

$$\left(\frac{\partial F_{ij}}{\partial \tau_r}\right)_{i-1/2,j} = \frac{F_{i,j} - F_{i-1,j}}{(\tau_r)_i - (\tau_r)_{i-1}} , \tag{3.18}$$

and center all the other differential operators at $(i-1/2, j)$. In discretizing the first moment of the transfer equation, we approximate the first derivative of the quantity F with respect to the variable τ_r using the relation

$$\left(\frac{\partial F_{ij}}{\partial \tau_r}\right)_{i+1/2,j} = \frac{F_{i+1,j} - F_{i,j}}{(\tau_r)_{i+1} - (\tau_r)_i} , \tag{3.19}$$

and center all the other differential operators at $(i+1/2, j)$. In both equations we approximate the first derivative of the quantity F with respect to photon energy by

$$\left(\frac{\partial F_{ij}}{\partial \epsilon}\right)_{ij} = \frac{F_{i,j+1} - F_{i,j-1}}{\epsilon_{j+1} - \epsilon_{j-1}} . \tag{3.20}$$

and the second derivative with respect to photon energy by

$$\left(\frac{\partial^2 F_{ij}}{\partial \epsilon^2}\right)_{ij} = \frac{2}{\epsilon_{j+1} - \epsilon_{j-1}} \left(\frac{F_{i,j+1} - F_{i,j}}{\epsilon_{j+1} - \epsilon_j} - \frac{F_{i,j} - F_{i,j-1}}{\epsilon_j - \epsilon_{j-1}} \right) . \tag{3.21}$$

We solve the system of equations (3.9) and (3.10) for the zeroth and first moments of the specific intensity of the radiation field, J and H^r, at N_τ grid points in optical depth and $N_{\rm En}$ grid points in photon energy. Therefore the system of equations has $N_\tau \times N_{\rm En}$ unknowns. At all the interior grid points ($1 < i < N_\tau$; $1 < j < N_{\rm En}$) we solve both equations (3.9) and (3.10) using the differencing scheme of equations (3.18)–(3.21). For $i = 1$ and for all j we solve equations (3.13) and (3.10), whereas for

$i = N_\tau$ and for all j we solve equations (3.14) and (3.9). Finally, for all i and for $j = 1, N_{En}$, we set both the zeroth and first moments of the specific intensity equal to zero, according to boundary conditions (3.15) and (3.16).

The resulting system of equations is linear in both the zeroth and first moments of the specific intensity. Defining the quantity P_i as

$$P_1 = J_{1,1}\ ;\quad P_2 = H^\tau_{1,1}\ ;\quad \ldots\quad P_{2N_\tau-1} = J_{N_\tau,1}\quad P_{2N_\tau} = H^\tau_{N_\tau,1}\quad \text{etc.} \tag{3.22}$$

the system of equations takes the form shown in Figure 3.2. The matrix of coefficients is a sparse matrix and can be solved efficiently with the biconjugate gradient method [see, e.g., Press et al. (1992), p. 209] with a preconditioner matrix. We choose the preconditioner matrix to be the coefficient matrix, with the elements at the outer two diagonal bands set equal to zero. The preconditioner matrix can then be inverted efficiently with the LU-decomposition method [see, e.g., Press et al. (1992), p. 202]. In this method, in order to avoid round-off errors, we scale all the rows in the coefficient matrix so that the highest value of the elements in each row is unity. Depending on the complexity of the particular problem, the system of difference equations can be solved to a fractional accuracy of 10^{-5} within less than fifty iterations, which can be performed in a fraction of a minute on a current workstation.

3.3.2 Solution of the Radiative Transfer Equation

In the iterative method of the variable Eddington factors, the transfer equations (3.8) is solved at every grid point in the $(p - z)$ plane for the boundary conditions (3.11) and (3.12). Because the generalized source function is calculated using the results from the previous iterations, the solution of equation (3.8) is just the formal solution that can be obtained analytically, i.e.,

$$\begin{aligned} I^-(\tau_z, p, \epsilon) &= -\int_0^{\tau_z} S(t, p, \epsilon) e^{(1-2\epsilon)(t-\tau_z)} dt \\ I^+(\tau_z, p, \epsilon) &= I^+(z_{\min}, p, \epsilon) e^{(1-2\epsilon)(\tau_z - \tau_{z\min})} \end{aligned}$$

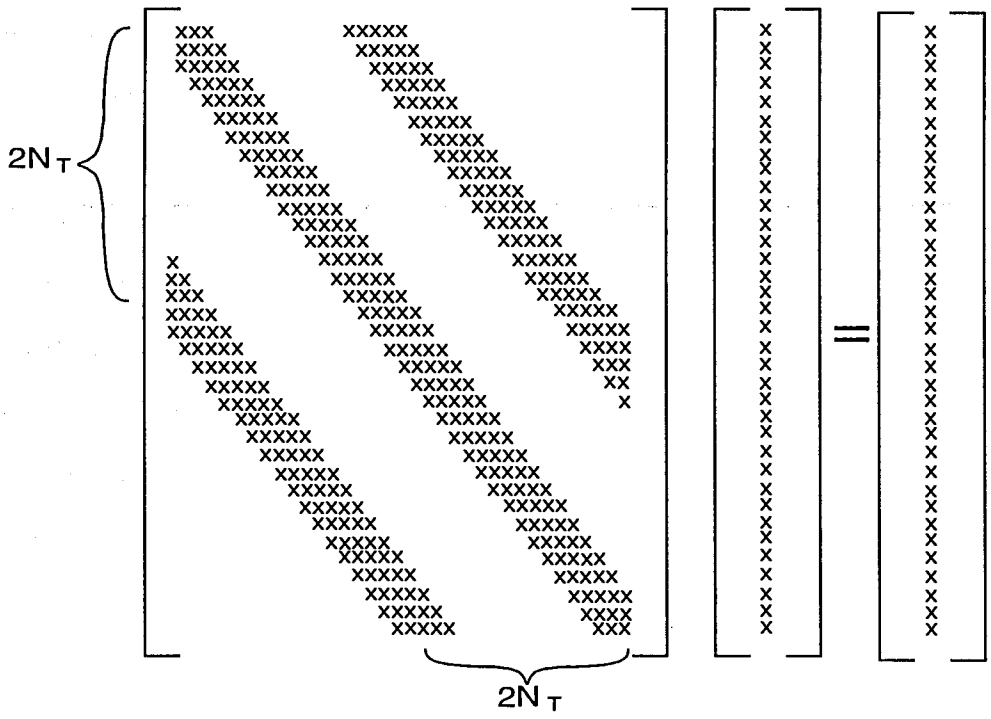

Figure 3.2: Schematic representation of the linear system of the discretized zeroth and first moments of the radiative transfer equation.

$$+\int_{\tau_z}^{\tau_{zmin}} S(t,p,\epsilon)e^{(1-2\epsilon)(\tau_z-t)}dt\,, \tag{3.23}$$

where

$$I^+(z_{\min},p,\epsilon) = \begin{cases} I^-(z_{\min},p,\epsilon)\,, & p > r_{\text{in}} \\ I^-(z_{\min},p,\epsilon) + 4H_0^r(\epsilon)\,, & p < r_{\text{in}} \end{cases} \tag{3.24}$$

and $z_{min} = 0$ or $z_{min} = (r_{\text{in}}^2 + p^2)^{1/2}$ when $p > r_{\text{in}}$ or $p < r_{\text{in}}$ respectively.

3.3.3 Code Validation

We test the implementation of the numerical method described above in the following way:

First we test the implementation of the solution to the radiative transfer equation. We choose the generalized source function to be an exponential in the variable τ_z so that the integrals in equations (3.23) can be evaluated analytically. We then calculate the numerical solution of the transfer equation and refine the discrete mesh until the numerical solution agrees with the analytic one.

Finally, we perform a consistency test between the solution of the transfer equation and the solution of the moment equations. We solve equation (3.8) iteratively without using the solution of the system of equations (3.9)–(3.10), by starting with an assumed generalized source function [e.g., $S(z,p,\epsilon)=0$], solving the transfer equation for the specific intensity, calculating its moments, updating the generalized source function, and repeating until convergence is achieved. We then calculate the moments of the specific intensity obtained in this way and compare them directly with the moments obtained by solving equations (3.9) and (3.10).

The desired accuracy of the calculations, which depends mainly on the choice of the discrete mesh, depends on the particular problem. Because we are interested in calculating the spectra of accreting compact objects, the X-ray colors of which are observed to change by a few percent when the mass accretion rate changes by a factor of ~ 2 (Hasinger & van der Klis 1989), we require for our solutions a fractional accuracy of $\sim 10^{-3}$.

3.4 Results

In this section we solve the radiative transfer equation for four model problems with spherical symmetry that are related to various astrophysical systems and in particular to accretion flows onto compact objects. In §3.4.1 we discuss Comptonization of soft X-ray photons by a static, uniform medium of hot electrons; this configuration is thought to be responsible for the hard X-ray spectra of weakly magnetic, accreting neutron stars (see, e.g., Lamb 1989). In §3.4.2 we solve the radiative transfer equation in a uniform, cold, converging flow; although such a configuration requires fine tuning of the physical conditions around an accreting object and may not occur in nature, it is used here to provide physical understanding of the effect of Comptonization by the bulk electron velocity. Finally, in §3.4.3 we discuss more realistic problems of spherical accretion onto and outflows from compact stars.

3.4.1 Compton Scattering in a Hot, Static Medium

For the first model problem, we consider a static, spherically symmetric, purely scattering medium and set the parameters to values that are typical for weakly magnetic, accreting neutron stars (see Psaltis et al. 1995). We set the outer radius of the scattering medium to $3r_{\rm in}$, its electron temperature to 10 keV, its electron scattering optical depth to 4, and the energy-dependence of the radiation flux at the inner boundary to be that of a blackbody with a temperature of 0.5 keV; the normalization of the input flux is arbitrary because we have assumed that there are no sources of photons in the medium. This is a frequently solved problem that has been analyzed in detail by, e.g., Katz (1976), Shapiro et al. (1976), and Sunyaev & Titarchuk (1980). All these authors showed that the emerging radiation spectrum at energies much larger than the energy of the injected photons is largely independent of the details of the input spectrum and can be described by a power-law with an exponential cut-off at $\sim 3T_e$. Here we solve this simple problem to demonstrate the fact that the variable Eddington factors are *not* independent of energy even when the photon mean-free path is independent of energy and the medium is static (see also the discussion in Paper I and Chapter 2).

Figure 3.3 shows the zeroth and first moments of the specific intensity of the radiation field, J and H^r, as a function of photon energy and radius. Both quantities decrease overall with increasing radius because of the dilution of the radiation field. The energy dependence of the radiation energy density changes within one photon mean-free-path from the inner boundary but remains unchanged at larger radii. On the other hand, the radiation flux evolves throughout the scattering medium. This is a consequence of the fact that we solved the system of moment equations by imposing an inner boundary condition on H and an outer boundary condition on the ratio H/J and not on J itself.

Figure 3.4 shows the first Eddington factor $f = K^{rr}/J$ at two photon energies as

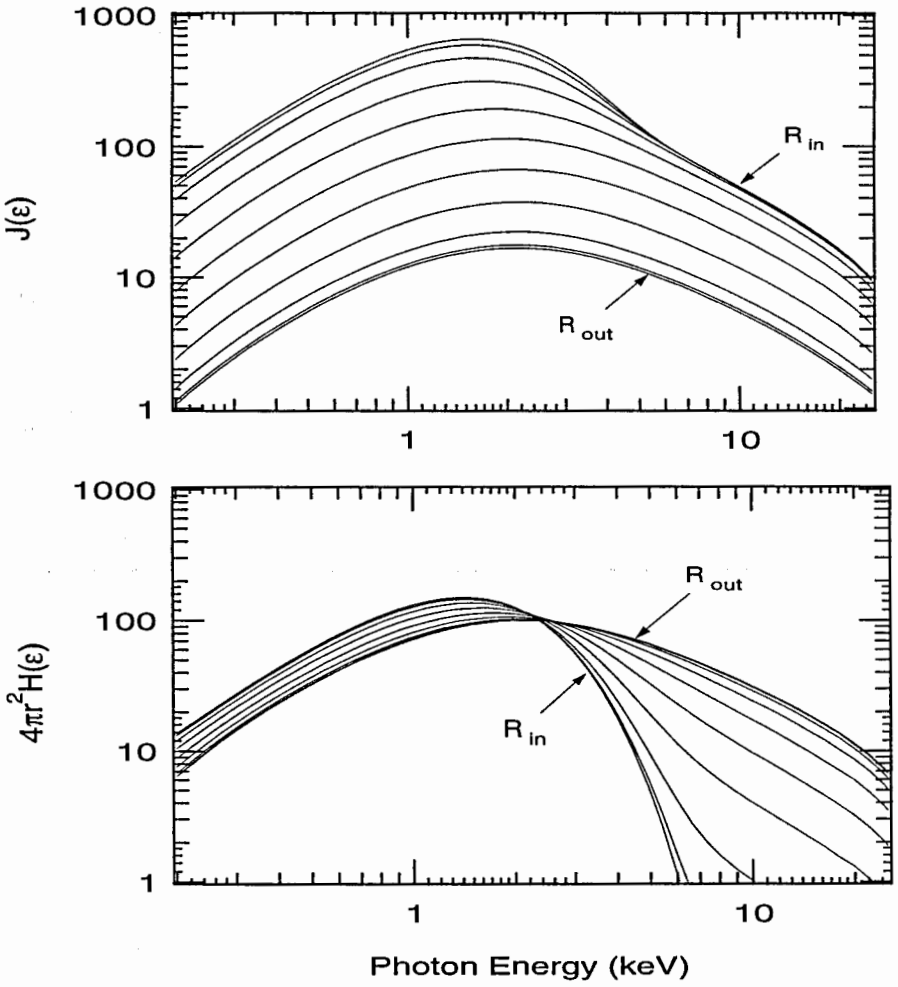

Figure 3.3: The zeroth and first moments of the specific intensity of the radiation field in the static, hot medium discussed in §3.4.1. In both panels the curves correspond to radii in the medium that are equidistant in the parameter Q (see eq.[3.17]).

well as the ratio of the energy-integrated second to zeroth moments of the specific intensity of the radiation field. The Eddington factor shows a strong dependence on photon energy even though the scattering cross section and hence the photon mean-free-path are mostly energy independent at these low photon energies. This is because photons were injected into the medium with energies $\ll T_e$ and on average gain energy at each scattering. As a result, photons emerging with low energy have experienced on average a smaller number of scatterings than photons with higher energy and therefore their distribution is less isotropic.

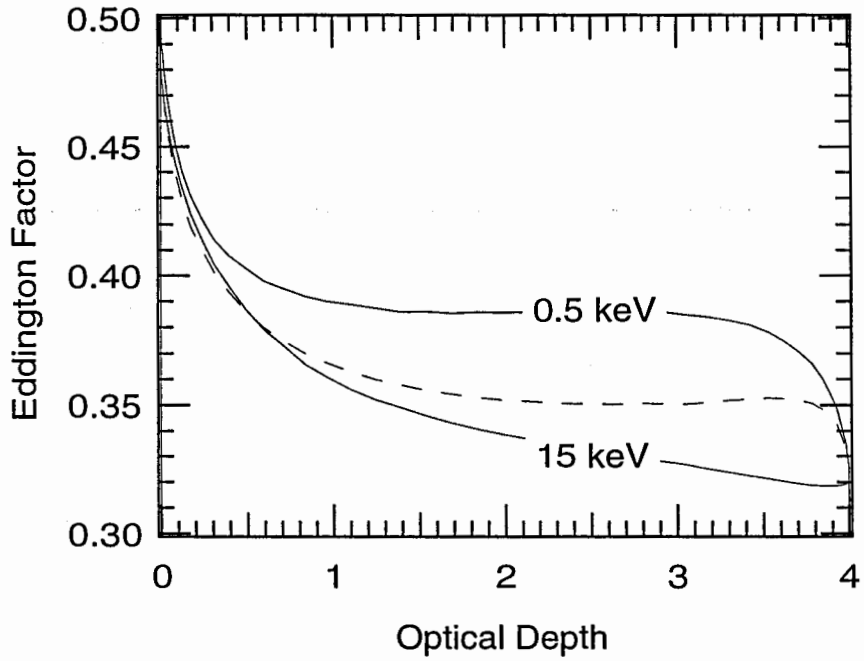

Figure 3.4: The first Eddington factor at two photon energies (solid lines) as well as the ratio of the energy-integrated second to zeroth moment of the specific intensity of the radiation field (dashed line) for the model problem discuss in §3.4.1.

Figure 3.5 compares the emerging radiation spectrum obtained using the method of variable Eddington factors with the spectra obtained using the same boundary conditions but two energy-independent prescriptions of the first Eddington factor that are commonly used; the second Eddington factor does not enter the calculation when the bulk velocity of the electrons is zero. Note that the prescription $f = 1/3$ for all photon energies is *not* the correct diffusion approximation for Compton scattering because it neglects the strong energy dependence of f on photon energy that exists even when the photon mean-free-path is smaller than any characteristic length in the system and photons diffuse through the scattering medium (see Psaltis & Lamb 1997 and Chapter 2). The discrepancy between the self-consistent solution and the ones obtained using prescribed Eddington factors is small for the prescription that depends on optical depth and can be as large as $\sim 50\%$ at high photon energies for the prescription that is independent of optical depth. This discrepancy increases when

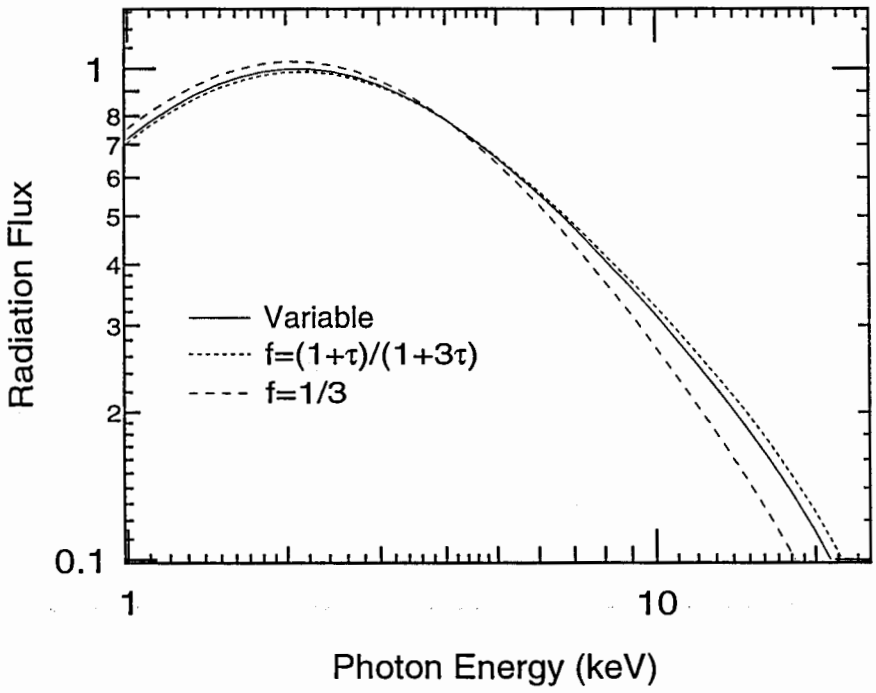

Figure 3.5: The radiation spectrum at the outer boundary obtained using the method of variable Eddington factors and the spectra obtained using the same boundary conditions but two energy-independent prescriptions of the first Eddington factor.

the ratio of the photon mean-free path to the smallest characteristic length scale in the system increases.

3.4.2 Compton Scattering in a Uniform Flow

In order to investigate the effects of Comptonization by the bulk electron flow we first use the same scattering medium as in the previous paragraph but set the electron temperature equal to zero and the inward electron bulk velocity equal to $0.2c$ everywhere in the flow.

Figure 3.6 shows the radiation spectrum at the inner boundary, the emerging radiation spectrum when only terms that are first-order in the electron bulk velocity are taken into account, as well as the emerging radiation spectrum that is correct to second order in the electron bulk velocity. The terms that are first-order in the electron bulk velocity produce a displacement in $\log \epsilon$ of the input spectrum towards

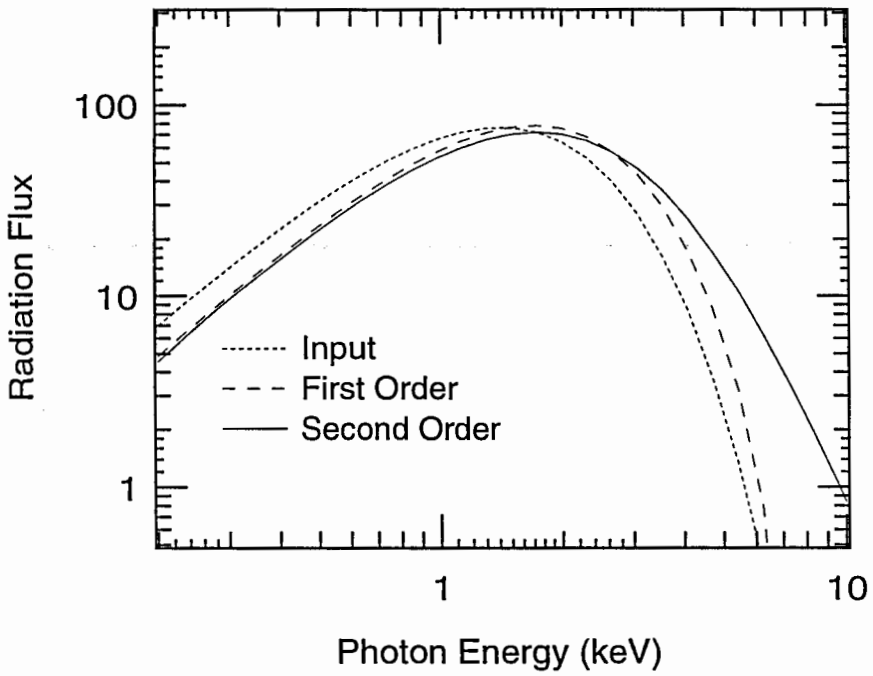

Figure 3.6: The radiation spectrum at the inner boundary (dotted line), the emerging radiation spectrum when only terms that are first-order in the electron bulk velocity are taken into account (dashed line), and the emerging radiation spectrum that is correct to second order in the electron bulk velocity (solid line) for the configuration discussed in §3.4.2.

higher photon energies, whereas the terms that are second-order in the electron bulk velocity produce a power-law tail at high photon energies.

When the total optical depth of the scattering medium and hence the average number of scatterings that each photon experiences are increased, then on average photons gain more energy by scattering off moving electrons. As a result, the emerging radiation spectrum is displaced towards higher photon energies, and the power-law tail becomes flatter (see Fig. 3.7a). The emerging spectrum changes in a similar way when the electron bulk velocity is increased (see Fig. 3.7b).

3.4.3 Compton Scattering in Inflows and Outflows

For our simple model calculations of accretion onto a central object we assume a free-fall density profile and set everywhere in the flow the electron temperature to zero and

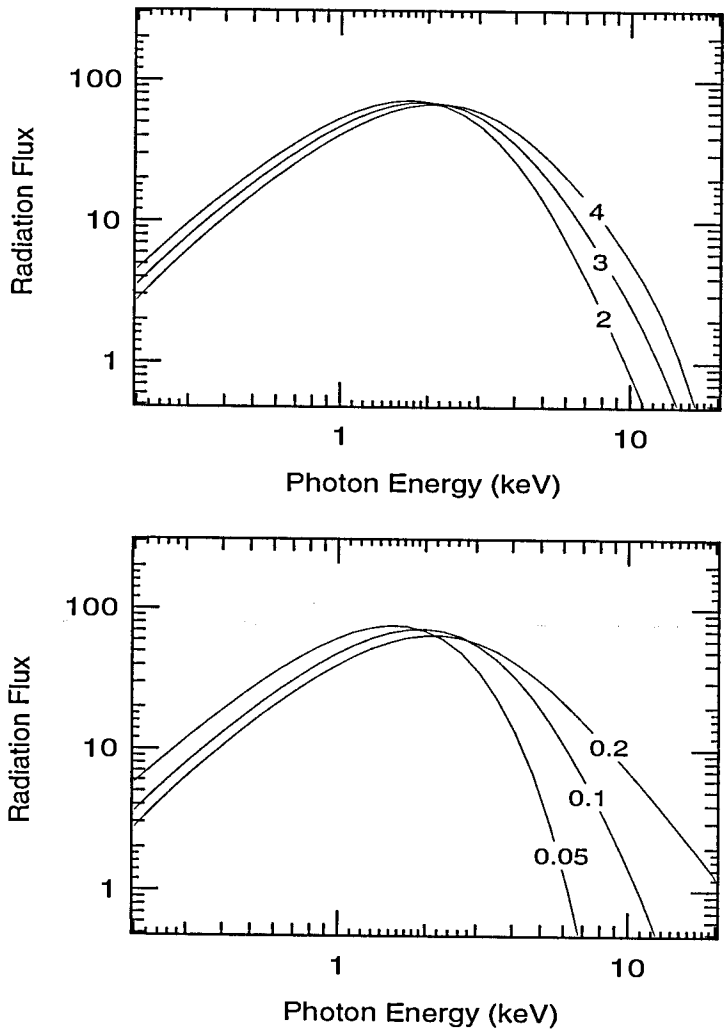

Figure 3.7: The dependence of the emerging radiation spectrum on (a) the electron scattering optical depth and (b) the electron bulk velocity, for the configuration discussed in §3.4.2.

the inward radial velocity equal to the free-fall velocity from infinity onto a compact object with a gravitational mass of $1.4M_{\odot}$. We also set the outer radius of the medium to $30r_{\rm in}$; at these large radii the photon mean-free path is large compared to radius and the electron bulk velocity is small compared to the speed of light that the flow does not effect significantly the photon distribution. Finally, instead of specifying the mass accretion rate onto the compact object, we specify the total electron-scattering optical depth of the flow.

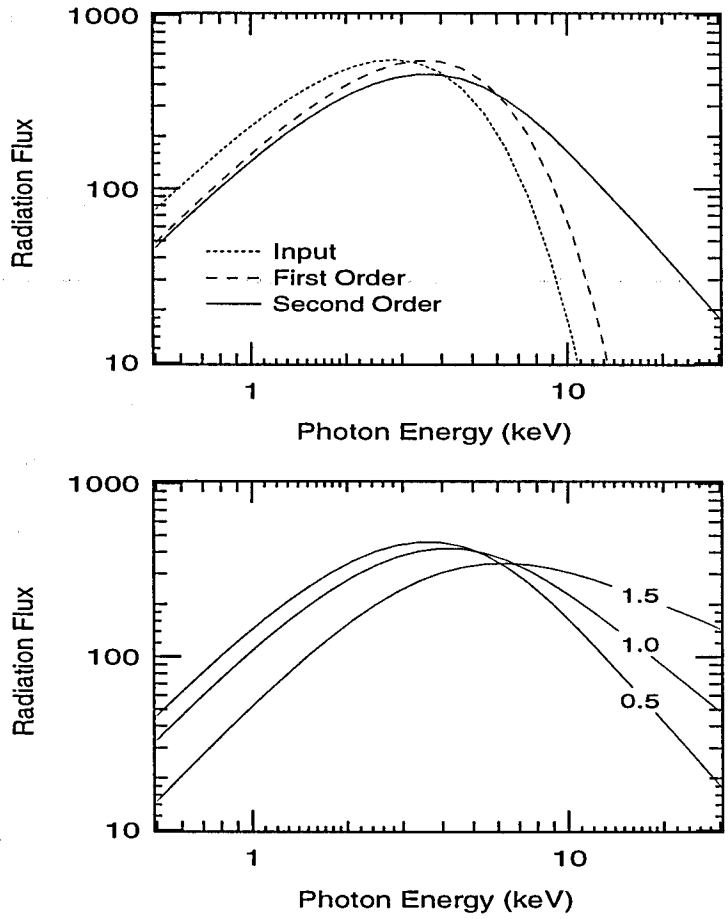

Figure 3.8: (a) The radiation spectrum at the inner boundary (dotted line), the emerging radiation spectrum when only terms that are first-order in the electron bulk velocity are taken into account (dashed line), and the emerging radiation spectrum that is correct to second order in the electron bulk velocity (solid line) for the inflow problem discussed in §3.4.3. (b) The dependence of the emerging radiation spectrum on the electron-scattering optical depth of the flow.

Figure 3.8a shows the radiation spectrum at the inner boundary, the emerging radiation spectrum when only terms that are first-order in the electron bulk velocity are taken into account, as well as the emerging radiation spectrum that is correct to second order in the electron bulk velocity. As in the model calculation discussed in §3.4.2, the terms that are first-order in the electron bulk velocity produce a displacement in $\log \epsilon$ of the input radiation spectrum towards higher photon energies. On the

other hand, the terms that are second-order in the electron bulk velocity systematically upscatter photons and produce a power-law tail at high photon energies. When the optical depth of the flow is increased, the systematic upscattering of photons becomes more efficient and the high-energy tail becomes flatter.

Figure 3.9 shows the same quantities as Figure 3.8 but for the case of an outflow. For this model problems we have used the same parameters as in the inflow calculation but changed the sign of the velocity at all radii. In an outflow, the terms that are first-order in the electron bulk velocity produce a displacement in $\log \epsilon$ of the input radiation spectrum towards *lower* photon energies. On the other hand, the effect of the terms that are second-order in the electron bulk velocity is the same as in the case of inflow, i.e., they systematically upscatter the photons and produce a tail at high photon energies. For the optical depths and bulk velocities considered here, the effect of the second-order terms nearly cancels the effect of the first-order terms and the major difference between the input and emerging spectra is the power-law tail at high photon energies. As in the case of the inflow, when the optical depth of the flow increases, the power-law tail becomes flatter.

3.5 Discussion

In the previous sections we presented a method for solving numerically the radiative transfer equation that describes Compton scattering in spherically symmetric systems, and applied it to a variety of cases related to accretion onto compact objects. We showed that the first Eddington factor, which describes the degree of isotropicity of the radiation field at a given point in space, may depend strongly on photon energy even though the photon mean-free-path is energy independent, if the photons are preferably upscattered or downscattered in energy at each scattering. We also demonstrated that the terms that are first-order in the electron bulk velocity alter the input spectrum in a way that is qualitatively and quantitatively different than

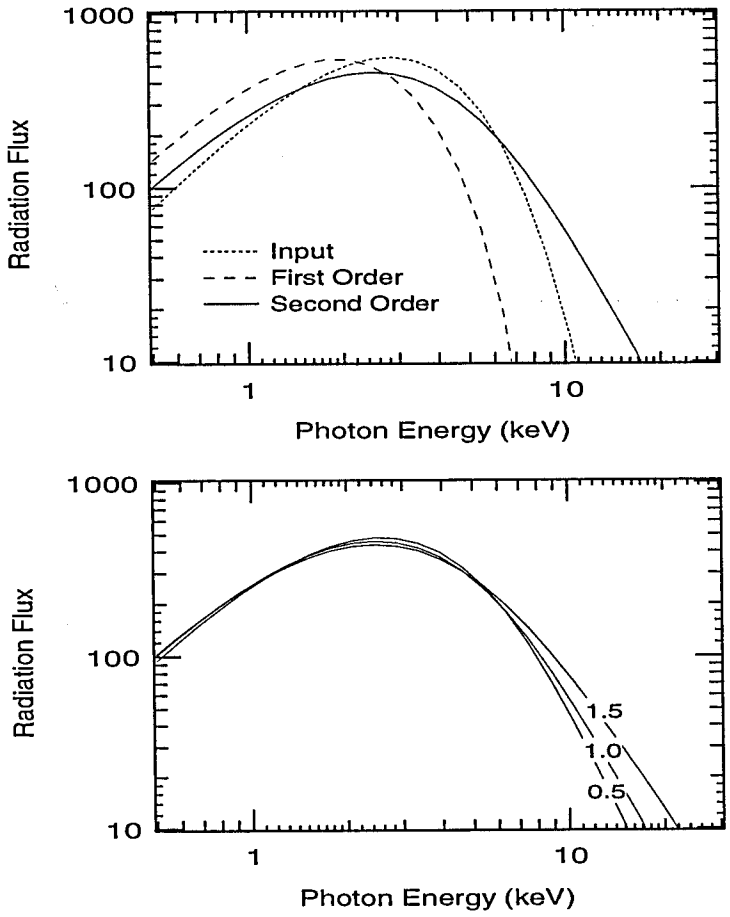

Figure 3.9: (a) The radiation spectrum at the inner boundary (dotted line), the emerging radiation spectrum when only terms that are first-order in the electron bulk velocity are taken into account (dashed line), and the emerging radiation spectrum that is correct to second order in the electron bulk velocity (solid line) for the outflow problem discussed in §3.4.3. (b) The dependence of the emerging radiation spectrum on the electron-scattering optical depth of the flow.

the effect of the terms that are of second-order.

The effect of the terms that are first-order in the electron bulk velocity becomes evident if we keep in the zeroth moment of the radiative transfer equation, which is also the energy equation of the radiation field, only these first-order terms, i.e., if we write it as

$$\frac{\partial}{\partial z}\left(H^r r^2\right) = -\frac{\partial}{\partial \log \epsilon}\left(H^r r^2\right) \ . \tag{3.25}$$

where

$$dz = -n_e \sigma_T \left(\vec{V} \cdot \hat{l}_H \right) dr \ , \tag{3.26}$$

where $\hat{l}_H$ is the unit vector in the direction of the radiation flux and we have again assumed that there are no sources of photons within the Comptonizing medium. The solution of equation (3.25) is simply

$$H^r(r, \log \epsilon) = H^r \left(r_{\rm in}, \log \epsilon' \right) \left(\frac{r_{\rm in}}{r} \right)^2 \ , \tag{3.27}$$

where

$$\log \epsilon' = \log \epsilon - \int_r^{r_{\rm in}} n_e \sigma_T \left(\vec{V} \cdot \hat{l}_H \right) dr \ . \tag{3.28}$$

Equation (3.27) describes a displacement in $\log \epsilon$ of the input spectrum towards higher photon energies when the photons move on average against the electrons ($\vec{V} \cdot \vec{H} < 0$) or towards lower photon energies when the photons move on average with the electrons ($\vec{V} \cdot \vec{H} > 0$). This result is very general, provided only that there are no sources of photons within the flow. It is independent of the value of the Eddington factors and hence is valid in both the diffusion and free-streaming regimes. It is also independent of whether the flow converges or diverges.

Equation (3.27) shows that the effect on the radiation of the terms that are first-order in the electron bulk velocity is determined mainly by the input boundary conditions. If there were sources of photons within the flow that were specified a priori, then the effect of these first-order terms would also depend very sensitively on the input spatial and energy distribution of these sources. Therefore, the power-law spectra obtained by various authors (see, e.g., Payne & Blandford 1981b; Mastichiadis & Kylafis 1992; Titarchuk, Mastichiadis, & Kylafis 1997) as a result of Comptonization of soft photons by the bulk electron motion, when only terms that are first-order in the electron bulk velocity are kept, are not general but depend very sensitively on the assumed boundary conditions and on the particular configuration of the problem under study. A discussion of Comptonization in moving media to first order in

the electron bulk velocity and a detailed comparison with previous studies will be reported elsewhere (Zampieri et al. 1997).

The effect on the radiation field of the terms that are second-order in the electron bulk velocity is qualitatively and quantitatively different than the effect of the terms that are first-order. At each scattering with a moving electrons, the second-order average fractional energy change of a photon in the system frame is always positive, independent of the photon energy, and equal to $4V^2/3$ (see, e.g., Rybicki & Lightman 1979, ch. 7; see also the discussion in Psaltis & Lamb 1997 and Chapter 2). If the distribution of photon residence times in the Comptonizing medium drops exponentially to zero at late times, then a power-law tail is produced at high photon energies (for total scattering optical depths $\gtrsim 1$), in analogy to the generation of power-law tails by thermal Comptonization.

The velocity at which the terms that are second-order in V become important depends on the ratio of the photon mean-free-path $\lambda_{\rm mfp}$ to the shortest characteristic length scale L in the problem. In general, when $V(\lambda_{\rm mfp}/L) \sim 1$, i.e., close to and within the photon-trapping radius, the terms that are first- and second-order in V become comparable in size (Yin & Miller 1995; Psaltis & Lamb 1997a and Chapter 2) and hence the latter should not be neglected.

In conclusion, using the above simple model-problems we demonstrated that radiative transport calculations in flows in which Compton scattering is important should be performed correctly at least to second order in the electron bulk velocity, even when this velocity is small. Moreover, we showed that the complete radiative transfer equation should be solved and not simply the moment equations, because the solution of the latter depends sensitively on the prescription used for the closure relations and on the boundary conditions. For models of accretion onto compact objects additional effects should be included in the calculations, such as departures from spherical symmetry and general relativistic effects. Models of the X-ray spectra of accreting

compact objects that can match the level of detail observed in these systems with current instruments can only be the results of very detailed calculations of the transport of radiation in the accretion flows around them.

Chapter 4

X-ray Spectra of Z Sources

4.1 Introduction

Low-mass X-ray binary systems (LMXBs) are thought to consist of a compact object (a neutron star or black hole) and a low-mass main sequence or giant companion. About 100 such systems have been detected in our galaxy. Despite many attempts during the last twenty years, no periodic X-ray brightness oscillations or cyclotron lines have ever been detected in the persistent emission of most low-mass X-ray binaries (see Mereghetti & Grindlay 1987; Wood et al. 1991; Vaughan et al. 1994b and references therein); only four of the known low-mass X-ray binary systems are X-ray pulsars (van Paradijs 1995). Current upper limits on the rms amplitude of any periodic oscillations with frequencies below 500 Hz in the persistent emission of most LMXBs range from a few percent in some faint LMXBs to $\sim 0.3\%$ in the brightest ones.

The detection of type I X-ray bursts from ~ 35 LMXBs, which are thought to be caused by thermonuclear flashes in the surface layers of a neutron star, provides compelling evidence that these particular systems contain accreting neutron stars (see Lewin, van Paradijs & Taam 1995). The recent detection of nearly coherent X-ray brightness oscillations with frequencies $\sim 360-590$ Hz from four LMXBs during type I X-ray bursts provides additional evidence that the compact objects in these systems are neutron stars (Strohmayer et al. 1996a, 1996b; Smith, Morgan, & Bradt 1997;

Zhang et al. 1997). About 20 LMXBs are thought to contain black holes, based either on measured mass-functions that imply gravitational masses higher than the expected $3M_{\odot}$ maximum mass of a neutron star or based on the detection of a collection of related phenomena that are thought to indicate the presence of a black-hole (Tanaka & Lewin 1995). In this chapter we will focus on low-mass X-ray binaries that contain neutron stars and will refer to them hereafter simply as LMXBs.

During the last decade, observations of LMXBs made using several X-ray satellites (mainly *EXOSAT* and *Ginga*) that had good spectral resolution and fast timing capabilities revealed a great number of phenomena at frequencies $\lesssim$200 Hz that vary systematically with the spectral state of the sources. All these phenomena were successfully organized by Hasinger & van der Klis (1989) into a general phenomenological framework (see also van der Klis 1989). According to this framework, many neutron-star LMXBs can be classified as either Z or atoll sources (the names come from the shapes of the tracks these sources make in X-ray color diagrams). Atoll sources have X-ray luminosities $\sim 0.01 - 0.1$ times the Eddington critical luminosity L_E, have several distinct broad-band components in their power density spectra below $\sim$ 200 Hz, and produce type I X-ray bursts. The Z sources, in contrast, have X-ray luminosities $\sim L_E$, produce two types of quasi-periodic X-ray brightness oscillations (QPOs) and three types of broad-band noise below $\sim$ 200 Hz, and infrequently burst if they burst at all. More recently, observations of Z and atoll sources with the *Rossi X-ray Timing Explorer* have revealed in several of these sources QPOs with frequencies of order $\sim$ 1 kHz (see, e.g., van der Klis et al. 1996; Berger et al. 1996; Strohmeyer et al. 1996a; Zhang et al. 1996) and characteristics that change with the X-ray spectra of the sources. In this chapter we concentrate on the rapid-variability phenomena with frequencies $\lesssim$200 Hz and refer to Miller, Lamb, & Psaltis (1997) for a discussion of a model for the kilohertz QPOs that is consistent with the results of the current work.

A model that provides a unified description of the X-ray spectra and variability of

the Z and atoll sources has been proposed by Lamb (1989). In this model, LMXBs are assumed to be weakly magnetic neutron stars that accrete matter from a Keplerian disk and also, when the mass accretion rate is near-Eddington, from a region of nearly radial inflow that originates in a corona above the inner part of the disk. If a source has a magnetic field $\gtrsim 10^9$ G and accretion rate $\sim 0.5 - 0.9\ \dot{M}_E$ (where $\dot{M}_E$ is the Eddington critical mass accretion rate), it produces quasi-periodic brightness oscillations at the beat frequency between the orbital frequency of density inhomogeneities in the accretion disk at the inner radius of the Keplerian flow of the gas that is threaded by the stellar magnetic field and the stellar spin frequency (Alpar & Shaham 1985; Lamb et al. 1985; Shibazaki & Lamb 1987). This is the so-called horizontal branch oscillation (HBO; see also §4.2). When the mass accretion rate becomes comparable to the Eddington critical rate, oscillations in the region of nearly radial inflow become weakly damped and QPOs are produced at frequencies approximately equal to the inverse inflow time from the outer radius of the region (Fortner, Lamb, & Miller 1989; Fortner 1992). This is the so-called normal/flaring branch oscillation (N/FBO). Relatively flat X-ray spectra, cut-off at energies in the range $10 - 30$ keV, are produced by Comptonization of soft photons, which are emitted close to the stellar surface, by the hot plasma that surrounds the neutron star. The preliminary results of Psaltis, Lamb, & Miller (1995) and of Litchfield & Kylafis (1996) have shown that the X-ray spectra and colors predicted by the unified model are consistent with observations.

In this chapter, we present the results of detailed numerical calculations of the X-ray spectra of the Z sources, based on the unified model. We treat in detail Compton scattering in the accretion flow around the neutron star. However, due to the complexity of the problem, we make several simplifying assumptions regarding the emission processes that are responsible for the production of photons near the neutron star surface. Even with these approximations though, the results provide a simple, physically consistent explanation of the $2 - 15$ keV X-ray spectra as well as of several

other heretofore inexplicable properties of the Z sources. In §4.2 we summarize the relevant observations and outline the key characteristics of the unified model. In §4.3 and §4.4 we discuss the physical conditions and radiation processes in the two main region of the model, namely the hot central corona and the region of nearly radial inflow. In §4.5 we demonstrate the ability of our spectral model to reproduce the X-ray spectra and color diagrams of the Z sources. Finally, in §4.6 we discuss the similarities and differences between Z sources with different neutron-star magnetic field strengths, as well as some implications of our results for issues related to the X-ray spectra of Z sources.

4.2 Observations and Theoretical Models

4.2.1 Observations and Spectral Models

Color diagrams and power spectra.—The Z sources are luminous LMXBs that show a characteristic Z-shaped pattern in their color-color diagrams, which consists of three branches: the horizontal (HB), normal (NB) and flaring branch (FB; Hasinger & van der Klis 1989). When a Z source is on the HB, a quasi-periodic oscillation of its X-ray emission is observed, with a centroid frequency $\simeq 20-60$ Hz that, in general, increase with increasing countrate and is accompanied by a low frequency noise component (LFN) in the power-density spectra (van der Klis et al. 1985). This is the so-called horizontal branch oscillation (HBO). On the normal branch, the HBO becomes weaker and eventually disappears into the noise. Instead, a low-frequency QPO peak appears in the power spectrum, with a frequency that does not show any similar correlation with countrate (Middleditch & Priedhorsky 1986). As the source moves through the NB-FB transition, the frequency of this low-frequency QPO increases abruptly, while the QPO peak becomes broader and weaker. This is the normal/flaring branch oscillation (N/FBO). A recent analysis of archival *EXOSAT* observations of Cyg X-2 revealed a QPO peak at ~ 26 Hz, when the source was near the hardest end of the FB

(Kuulkers & van der Klis 1995); it is still unclear whether this QPO peak is related to the N/FBO or represents a third type of QPO.

The motion of a particular source along the Z pattern in the color diagram is erratic but continuous and is thought to be described by the very low frequency noise component (VLFN) in the power spectrum of the source (see Dieters & van der Klis 1997). A complete Z track is usually traced out on a timescale of 10–20 hours. In general, all the rapid variability phenomena appear to vary systematically, continuously, and reproducibly with position on the Z. Similar patterns are also traced by the Z sources in the hardness-countrate diagrams.

Recent analyses of archival *EXOSAT* data (Kuulkers et al. 1994; Kuulkers 1995; Kuulkers & van der Klis 1996; Kuulkers, van der Klis, & Vaughan 1996) indicate that the Z sources can be further divided into two classes: Cyg X-2, GX 5−1 , and GX 340+0 (hereafter referred to as the "Cyg-like" sources) form one class, whereas Sco X-1, GX 17+2 , and Sco X-2 (hereafter referred to as the "Sco-like sources") form the other. The Cyg-like sources have: (1) extended HBs, (2) short FBs in the HID that extend towards lower countrates, (3) strong HBO, and (4) Z patterns that are not fixed in the color diagram plane, but move on time scales of a few days. On the other hand, the Sco-like sources have: (1) short HBs, (2) long FBs in the hardness-countrate diagrams, which extend towards higher count-rates, (3) weak (GX 17+2 , Sco X-1) or absent (GX 349+2) HBO, (4) peaked LFN on the HB, and (5) Z patterns that are fixed in the color-color plane.

In discussing the tracks of the Z sources in color diagrams, a monoparametric reference frame is often used to describe the position of a particular source along any branch (Hertz et al. 1992). This single parameter, the so-called rank number, is set equal to 1 at the HB-NB transition (hard vertex) and equal to 2 at the NB-FB transition (soft vertex) and is allowed to increase continuously and monotonically from the HB to the NB and finally to the FB. Positions on the HB and the FB are

assigned rank numbers based on the metric established by the NB length.

Spectral models—In early work, a variety of simple mathematical expressions were used to fit the observed spectra of the Z and atoll sources. As the precision of measurements improved, acceptable fits to the spectra of these sources could not be obtained with a single, simple expression and additional components were introduced to the model spectra (Swank & Serlemitsos 1985). Over time, expressions with an increasing number of free parameters have given statistically acceptable fits to the data (White et al. 1986; Mitsuda et al. 1984; White, Stella, & Parmar 1988; Schulz, Hasinger, & Trumper 1989; Hasinger et al. 1990; Asai et al. 1994; Christian & Swank 1997; see Vacca et al. 1987 for a discussion of the different models). However, when additional components were added to the model spectra, the number of free parameters became comparable to the implicit degrees of freedom in the data and statistically acceptable fits to the same observations could be obtained using a variety of quite different mathematical models. These spectral models, when folded with the response of the detectors, give a fairly good representation of the observed countrate spectra, although most are simply mathematical functions and not the result of self-consistent detailed calculations of the various physical processes that take place around accreting neutron stars. Some authors have also developed physical models, which fit well the time-averaged spectra of particular Z and atoll sources (White et al. 1986; Ponman et al. 1989; Schulz & Wijers 1993). However, these models do not attempt to describe the detailed phenomenology and properties of the Z sources, i.e., the properties of the QPOs, the variation of the model parameters with mass-accretion rate, etc.

Most of the above analyses have shown that the spectra of Z sources between $1-15$ keV can be fitted fairly well by the sum of a power-law spectrum (with an exponential cut-off at energies $\sim 10-30$ keV) plus a broad spectral component (usually a blackbody component) at energies $\sim 1-3$ keV. The spectra of Z sources at energies $\gtrsim$15 keV could not be observed with satellites like *EXOSAT* or *GINGA* that had

a vanishingly small quantum efficiency at these high photon energies. Observations with *SIGMA* and with balloon-born detectors have shown that less than $\sim 1\%$ of the total X-ray flux of the Z sources is emitted at energies $\gtrsim$30 keV (Barret & Vedrenne 1994; see also Matt et al. 1990; Ubertini et al. 1992; Gilfanov et al. 1993).

The detection of iron emission lines (e.g., at $\sim$ 6.7 keV) is hampered by inaccuracies in the subtraction of the continua and has been debated for several years. Detection of broad (FWHM$\sim 0.5 - 1$ keV) iron emission lines has been reported for some Z sources (e.g., Sco X-1: Suzuki et al. 1984; White, Peacock, & Taylor 1985; Cyg X-2: Chiappetti et al. 1990; Smale et al. 1993), whereas any emission lines were absent in others (GX 5−1 : Kendziorra et al. 1985). Gottwald et al. (1995) summarized the results on iron emission lines obtained by *EXOSAT*. Finally, there have been many reports of detections of broad emission lines at $\sim$ 1 keV in Cyg X-2 and Sco X-1 (see Kuulkers et al. 1997 and references therein).

4.2.2 The Unified Model

In the unified model (for a detailed discussion of the unified model see Lamb 1989), the compact object in a Z source is assumed to be a neutron star with a magnetic field strength of $\sim 10^9 - 10^{10}$ G accreting matter from a disk fed by the companion star.

At all mass accretion rates, the magnetosphere and the inner disk are surrounded by a hot central corona (HCC). Electron scattering in this HCC spreads the pulsar beam and efficiently suppresses periodic modulations of the X-ray brightness at the spin frequency of the neutron star (Lamb 1989; see also Brainerd & Lamb 1987; Kylafis & Phinney 1989).

When the total luminosity of the neutron star, the HCC, and the inner disk becomes comparable to the Eddington critical luminosity, the outward radiation force drives plasma out of the disk, forming an extensive inner disk corona (Lamb 1989;

Fortner, Lamb, & Miller 1989; Fortner 1992). Radiation drag then removes the azimuthal and vertical momentum from the plasma in the inner disk corona in less than one orbit creating a region of approximately radial inward flow (RF). Because of the close balance between gravity and the radial component of the radiation force, oscillations in the region of approximately radial inflow with frequencies $\sim 5 - 10$ Hz become weakly damped (Fortner et al. 1989; Fortner 1992; Miller & Park 1995) and these modes appear in the power spectra of the Z sources as QPO peaks, the so-called N/FBO. Detailed numerical calculations of the frequency, phase shift, and energy-dependent amplitudes of the N/FBO are in excellent agreement with observations (Fortner et al. 1989; Fortner 1992; Miller & Lamb 1992).

In the unified model, the behavior of a LMXB depends primarily on two parameters: the neutron star surface magnetic field strength $B_{\rm NS}$ and the mass accretion rate $\dot{M}$. Although the magnetic field is not expected to vary on the time scales of interest here, there is evidence that the mass accretion rate changes by $\sim 10\%$ within ~ 100 s and by a factor of two within a few hours (see van der Klis 1989). In the Z sources, it appears that $\dot{M}$ increases monotonically as the source moves along the Z (i.e., with rank number), in the sense HB$\rightarrow$NB$\rightarrow$FB. This is supported by (for a more complete discussion see van der Klis & Lamb 1997): (1) the small width of the Z-shaped patterns in the color diagrams and the fact that all properties of the Z sources vary systematically, continuously, and reproducibly with position along the Z, (2) the increase of the centroid frequency of the HBO along the HB (e.g., Kuulkers et al. 1994), which according to the magnetospheric beat-frequency model (Alpar & Shaham 1985; Lamb et al. 1985) is caused by an increase in the mass accretion rate through the inner accretion disk, (3) the rapid turn-on of the N/FBO in the middle of the NB which, in the unified model, is caused by the rapid decrease in the damping of radial oscillations with increasing mass accretion rate (Fortner et al. 1989; Fortner 1992), (4) the increase of the X-ray variability as the sources move from the NB to

the FB, which is expected if $\dot{M}$ changes from subcritical to supercritical, and (5) the monotonic increase of UV emission lines and continuum flux along the Z, which can be fit by accretion disk models in which the mass accretion rate increases with rank number (Vrtilek et al. 1990). Hereafter we shall assume that the variations in the X-ray colors and countrates that produce the Z-shaped patterns in the color-color diagrams are caused by variations in the mass accretion rate.

4.3 The Hot Central Corona

As outlined in §4.2, according to the unified model the neutron star in a Z source is surrounded by a hot central corona that suppresses any periodic oscillations at the spin-frequency of the neutron star and in which the hard X-ray spectrum of the source is formed. In this section, we discuss the heating and cooling of the electrons, the structure of the magnetic field, and the dominant radiation processes in the HCC.

4.3.1 Heating and Cooling of the Electrons

In principle, the HCC could be supported against gravity by the stellar magnetic field, rotation, radiation forces, gas pressure gradient forces, or be in free-fall. The fact that all LMXBs—which have different magnetic field strengths, mass accretion rates, and are observed at different inclinations—show evidence for a Comptonizing corona that surrounds the inner disk and magnetosphere strongly suggests that the HCC is more or less spherically symmetric and hence cannot be supported by the stellar magnetic field or by rotation. Since a HCC exists even at mass accretion rates that are much lower than the Eddington critical rate (i.e., in the atoll sources), the HCC cannot be supported by radiation forces or even be in free-fall, because in the latter case the optical depth of the HCC would not be enough to account for the hard X-ray spectra of LMXBs. As a result, the HCC is probably supported by the thermal pressure of hot ions. We thus have a situation in which the ions are heated

by unspecified processes (perhaps interaction with the magnetosphere or thermal instability of the inner disk) and cooled by interaction with electrons, the electrons are heated by the ions (collisional heating) and cooled by interactions with photons, and the photons are heated by the electrons (Comptonization and cyclotron emission and self-absorption; energy exchange between photons and electrons due to thermal bremsstrahlung is negligible, as we demonstrate in §4.3.3). Here we demonstrate with the following simple argument that radiative cooling in the HCC can be very efficient in maintaining the electrons at a much lower temperature than the ions.

In order for the ion thermal pressure to support the gas in the HCC, the ion temperature should be comparable to the free-fall temperature

$$T_i \simeq \frac{2}{3}\left(\frac{m_p}{m_e}\right)\left(\frac{R_g}{R_{\rm NS}}\right)\left(\frac{R_{\rm NS}}{R}\right) m_e c^2 \simeq 0.1\left(\frac{R_g/R_{\rm NS}}{0.2}\right)\left(\frac{R_{\rm NS}}{R}\right)\ {\rm GeV}\,, \qquad (4.1)$$

where m_p and m_e are the proton and electron rest masses, $R_{\rm NS}$ is the radius of the neutron star, $R_g \equiv GM/(R_{\rm NS}c^2)$, and M is the mass of the neutron star.

The electrons exchange energy with the ions via Coulomb collisions and with the photons via Compton scattering and cyclotron absorption and emission. We approximate the Coulomb heating rate by (Spitzer 1956)

$$\Gamma_{\rm c} = \frac{3}{2} n_i k_{\rm B}(T_i - T_e)\frac{1}{t_{e-i}}\,, \qquad (4.2)$$

where n_i is the ion number density, T_i and T_e are the ion and electron temperatures, and t_{e-i} is the characteristic time-scale for energy-exchange between ions and electrons. This time scale is (Spitzer 1973)

$$t_{e-i} = \frac{3A_i m_e m_p}{8\sqrt{2\pi} n_e Z_i^2 e^4 \ln\Lambda}\left(\frac{k_{\rm B}T_e}{m_e} + \frac{k_{\rm B}T_i}{m_i}\right)^{3/2}\,, \qquad (4.3)$$

where n_e is the electron density and A_i and Z_i are the massive and atomic numbers of the ions,

$$\Lambda \equiv \frac{3}{2Z_i e^3}\left(\frac{k_{\rm B}^3 T_e^3}{\pi n_e}\right)^{1/2}\begin{cases} 1\,, & T_e < 4.2\times10^5\ {\rm K} \\ (T_e/4.2\times10^5\ {\rm K})^{-1/2}\,, & T_e \geq 4.2\times10^5\ {\rm K}\end{cases}\,, \qquad (4.4)$$

and e is the electron charge.

We calculate the Compton and cyclotron heating and cooling rates by integrating the right side of the zeroth moment of the radiative transfer equation, which is also the energy equation of the radiation field, [see equation (4.23) below] over photon energies and obtain

$$\Gamma_{\rm R} = 4\pi \left[-n_e \sigma_T \frac{4k_{\rm B}T_e - \langle E \rangle_J}{m_e c^2} + \langle \chi \rangle_{S-J} \left(\frac{S}{J} - 1 \right) \right] J \, , \tag{4.5}$$

where σ_T is the Thomson scattering cross section, χ is the absorption coefficient and S the source function for cyclotron emission (taken here to be the Planck spectrum), J is the energy integrated zeroth moment of the specific intensity of the radiation field,

$$\langle E \rangle_J = \frac{1}{J} \int_0^\infty E J_E dE \, , \tag{4.6}$$

and

$$\langle \chi \rangle_{S-J} = \frac{1}{S-J} \int_0^\infty \chi (S_E - J_E) dE \, . \tag{4.7}$$

In steady state, there is no net energy exchange between the ions, the electrons, and the photons and hence $\Gamma_{\rm C} = \Gamma_{\rm R}$. Using equations (4.1)–(4.7) we can estimate the equilibrium electron temperature as

$$T_e \simeq 6 \left(\frac{R_g/R_{\rm NS}}{0.2} \right)^{-1} \left(\frac{R}{R_{\rm NS}} \right) \left(\frac{H}{H_{\rm E}} \right)^{-1} \left(\frac{\ln \Lambda}{15} \right) \left(\frac{T_i}{0.1 \text{ GeV}} \right)^{-1/2} \left(\frac{1}{1+\xi} \right) \text{ keV} \, , \tag{4.8}$$

where H is the energy-integrated radial component of the first moment of the specific intensity of the radiation field, $4\pi H_{\rm E} = cGMm_p/(R_{\rm NS}\sigma_T)$ is the Eddington critical flux at the neutron star surface, and ξ is the ratio of the cyclotron and Compton heating and cooling rates. In writing equation (4.8) we have assumed that $T_i \gg T_e \gg \langle E \rangle_J/4$ and that $J \sim 3 n_e \sigma_T R H$. The parameter ξ depends on the details of the transport of radiation in the HCC. Using the numerical simulations presented in §4.5 we find that, for the magnetic field strengths and electron densities that are typical for the HCC around Z sources, $\xi \lesssim 1$. Note that the last four terms in equation (4.8)

depend implicitly on T_e. For example, $4\pi H$ is the local energy flux of the radiation field at the *base* of the HCC and therefore it is not simply proportional to the accretion luminosity but depends on the efficiency of Comptonization in the HCC and hence on T_e.

Equation (4.8) demonstrates that the electrons in the HCC can have a significantly lower temperature than the ions because of the very efficient radiative cooling. As the photon flux increases, Compton cooling of the electrons becomes more efficient and the electron temperature decreases. Moreover, when the efficiency of cyclotron cooling increases, the electron temperature decreases, as well.

4.3.2 Magnetic Field Structure

The magnetosphere of the neutron star is compressed both by the accretion disk and by the settling gas in the HCC. Because of the very high electrical conductivity of the gas, electric currents that flow in the accretion disk and possibly in the HCC can screen the stellar magnetic field from these regions. As a result, the magnetic flux from the stellar field is trapped within a small volume and therefore the magnetic field strength in the magnetosphere increases.

In order to estimate the amplification of the stellar magnetic field in the magnetosphere and hot central corona we make the following simplifying assumptions. We assume that the neutron star has only a magnetic dipole moment μ_d, that the magnetosphere is current-free, and that the stellar magnetic field is zero at radii larger than a characteristic radius in the HCC. This characteristic radius must be smaller than the size of the HCC in order for electron scattering to reduce the amplitudes of any periodic oscillations produced by the channeling of the accreting gas by the stellar field below the currently observed upper limits. We therefore set this characteristic radius equal to the outer radius of the HCC and hence calculate an upper limit on the magnetic field strength in the magnetosphere.

Starting from Maxwell's equation

$$\nabla \cdot \vec{B} = 0 \,, \tag{4.9}$$

where $\vec{B}$ is the magnetic field in the magnetosphere, and defining the magnetic potential as $\nabla\Phi \equiv \vec{B}$ we obtain

$$\Phi(r,\theta) = \sum_l \left(a_l r^l + \frac{b_l}{r^{l+1}} \right) P_l(\cos\theta) \,, \tag{4.10}$$

where r and θ are the polar coordinates in a plane perpendicular to the equatorial plane and $P_l(\cos\theta)$ are the Legendre polynomials of order l.

Using the continuity of the component of the magnetic field that is perpendicular to the interface between the hot central corona and the region of nearly radial inflow we obtain

$$a_l = \frac{l+1}{l} \frac{b_l}{R_{\rm HCC}^{2l+1}} \,, \tag{4.11}$$

where $R_{\rm HCC}$ is the radius of the interface. Similarly, using the continuity of the component of the magnetic field that is perpendicular to the neutron star surface, i.e., $B_r(R_{\rm NS}) = -(2\mu_d/R_{\rm NS}^3)\cos\theta$, we obtain

$$b_l = \begin{cases} \frac{\mu}{(R_{\rm NS}/R_{\rm HCC})^3 - 1} \,, & l = 1 \\ 0 \,, & l \neq 1 \end{cases} \tag{4.12}$$

The two components of the magnetic field in the magnetosphere therefore become

$$B_r = \frac{2\mu_d}{R^3} \left[\frac{(R/R_{\rm HCC})^3 - 1}{(R_{\rm NS}/R_{\rm HCC})^3 - 1} \right] \cos\theta \tag{4.13}$$

and

$$B_\theta = \frac{\mu_d}{R^3} \left[\frac{2(R/R_{\rm HCC})^3 + 1}{(R_{\rm NS}/R_{\rm HCC})^3 - 1} \right] \sin\theta \,. \tag{4.14}$$

In the following radiative transfer calculations, we shall assume that the hot central corona is spherically symmetric. For this reason, at every given radius R we shall use an average of the magnetic field strength over the polar angle θ as an estimate of the strength of the magnetic field at this radius. Figure 4.1 shows the root-mean-square of the magnetic field strength in units of the magnetic field strength of an

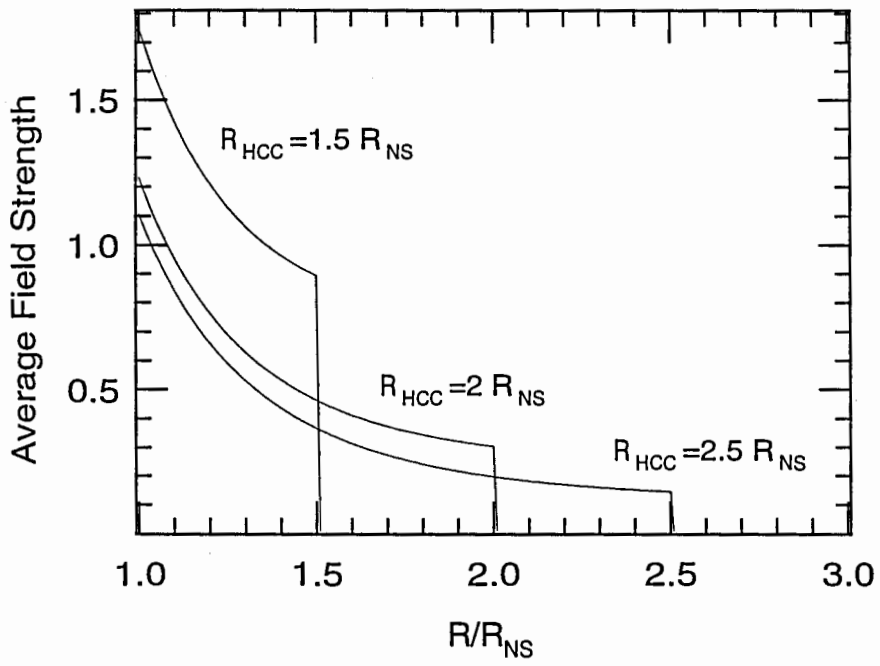

Figure 4.1: The angle-averaged magnetic field strength in the hot central corona, in units of the magnetic field strength of an isolated neutron star at its magnetic equator, for different values of the radius of the hot central corona.

isolated neutron star at its magnetic equator for different values of the radius of the hot central corona and demonstrates the fact that as $R_{\rm HCC}$ decreases, the strength of the magnetic field in the magnetosphere increases. Note also that although the neutron star is assumed to have only a dipole magnetic moment when it is isolated, the magnetic field in the magnetosphere is non-dipolar.

4.3.3 Radiation Processes

At the photon energies ($\gtrsim$0.5 keV), electron-scattering optical depths ($\sim 3-5$), and magnetic-field strengths ($\lesssim 10^{10}$ G) of interest here, the only relevant radiation processes are thermal bremsstrahlung, cyclotron emission and self-absorption, and Compton scattering. In this section we discuss each of these processes in detail.

Thermal Bremsstrahlung

The absorption coefficient for thermal bremsstrahlung at photon energy E is (Rybicki & Lightman 1979, p. 162)

$$\chi^{TB} \simeq 3\times10^{-5} Z^2 g(T_e, E) \left(\frac{T_e}{10 \text{ keV}}\right)^{-1/2} \left(\frac{E}{1 \text{ keV}}\right)^{-3} \left(\frac{n_i}{10^{19} \text{ cm}^{-3}}\right) \left(1 - e^{-E/T_e}\right) n_e \sigma_T \,, \tag{4.15}$$

and therefore for the electron densities and temperatures of interest here, the magnetosphere and hot central corona of the neutron star are optically thin to thermal bremsstrahlung.

The volume emissivity of optically thin thermal bremsstrahlung is given by (Rybicki & Lightman 1979, p. 162)

$$\epsilon^{TB} = 1.4 \times 10^{-27} T_e^{1/2} n_e n_i Z^2 g(T_e) \text{ erg s}^{-1} \text{ cm}^{-2} \,, \tag{4.16}$$

where $g(T_e)$ is the Gaunt factor averaged over photon energy. If optically thin thermal bremsstrahlung were the dominant source of photons in a Z source then the required radius of the emitting region would be

$$R \simeq 2 \times 10^{11} Z g(T_e) \tau_{es}^{-2} \left(\frac{T_e}{1 \text{ keV}}\right)^{-1/2} \left(\frac{L}{10^{37} \text{ erg c}^{-1}}\right) \text{ cm} \,, \tag{4.17}$$

where τ_{es} is the electron scattering optical depth of the region and L is the emerging luminosity. Clearly, optically thin thermal bremsstrahlung is an inefficient photon production mechanism since the size of the emitting region in the Z sources is expected to be comparable to the radius of the neutron star, i.e., comparable to 10^6 cm ($\ll 10^{11}$ cm).

Cyclotron Emission

The energy of the fundamental electron cyclotron frequency in the magnetosphere is

$$E_c = \hbar\omega_c \equiv \frac{B_m e}{m_e c} \simeq 0.012 \left(\frac{B_m}{10^9 \text{ G}}\right) \text{ keV}, \tag{4.18}$$

where B_m is the magnetospheric field strength. Cyclotron emission is self-absorbed if (Bekefi 1965)

$$\Lambda \equiv \frac{\omega_p^2 R}{\omega_c c} = 4\pi e n_e R B^{-1} \simeq 1.8 \times 10^7 \left(\frac{B_m}{10^9 \text{ G}}\right)^{-1} \tau_{es} \gg 1, \qquad (4.19)$$

where ω_p is the plasma frequency, n_e is the electron density, R is the characteristic length of the emitting region, namely the size of the magnetosphere, and τ_{es} is the electron scattering optical depth in the HCC, which we have approximated by $\tau_{es} \simeq n_e \sigma_T R$, where σ_T is the Thomson scattering cross section. Equation (4.19) shows that cyclotron emission in the magnetosphere is heavily self-absorbed for the magnetic field strengths and optical depths that are typical for the Z sources.

A characteristic feature of cyclotron absorption is the strong dependence of the absorption coefficient on photon energy. Let $E_{\max}$ be the photon energy that corresponds to the maximum flux due to cyclotron emission; $E_{\max}$ is comparable to the energy at which the cyclotron-absorption optical depth is equal to one and depends on the parameter Λ, the electron temperature T_e, and the geometry of the emitting region (see Bekefi 1965). At energies below $E_{\max}$ the optical depth is very high and hence, when electron scattering in the emitting region is negligible, the energy spectrum follows very closely the Planck spectrum. At energies above $E_{\max}$ the optical depth is almost zero and the energy spectrum drops rapidly. If electron scattering is not negligible and $E_{\max}$ is smaller than the electron temperature, then a fraction of the photons are upscattered by resonant and non-resonant scattering from the hot electrons and a power-law tail is formed at photon energies higher than $E_{\max}$.

Several authors have estimated $E_{\max}$ for a slab geometry (see, e.g., Bekefi 1965; Hartmann, Woosley, & Arons 1988; Chanmugam & Langer 1991). In this chapter we use the cyclotron absorption coefficients derived by Robinson & Melrose (1984) and generalized by Hartmann et al. (1988) for a relativistic Maxwellian distribution of electrons. These absorption coefficients were calculated in the continuum approximation (i.e., with no harmonic structure) and were found to be very accurate at the

high harmonic numbers ($\gtrsim$8; see Chanmugam et al. 1989) that are relevant for the magnetospheres of Z sources.

Modeling in detail cyclotron emission, self-absorption, as well as resonant and non-resonant scattering in the HCC would require solving four coupled, multi-dimensional equations for the Stokes parameters in the HCC with extremely complicated coupling kernels; such a calculation is very time consuming even with current computers and numerical algorithms. Furthermore, this calculation would require the use of transition rates derived for situations where the electron thermal velocities are mildly relativistic and the radiation field is intense (photon occupation number $\gtrsim$1); such transition rates are not currently available in the astronomical literature. However, as we demonstrate in the following sections, the above processes are important at energies $\lesssim$1 keV and the X-ray spectrum at higher energies is formed by Comptonization of the soft cyclotron photons and is mostly independent of the details of cyclotron emission and absorption. For modeling the HCC, we shall therefore solve the polarization-independent radiative transfer equation in spherical symmetry using the polarization- and angle-averaged absorption coefficients for cyclotron emission and absorption discussed above.

Figure 4.2 shows the absorption coefficient for cyclotron self-absorption in units of the inverse photon mean-free-path for electron scattering and compares it to the absorption coefficient for thermal bremsstrahlung for an electron temperature of $T_e = 10$ keV and for a variety of magnetic field strengths and electron densities that are typical for the HCC and the upper surface layers of the neutron star. When the electron temperature is higher than 10 keV, the absorption coefficient for cyclotron self-absorption at a given energy increases whereas the absorption coefficient for thermal bremsstrahlung decreases. For an electron scattering optical depth of 5, cyclotron emission is self-absorbed up to a photon energy of $\sim 0.8(B/10^{10}$ G) keV and therefore up to a harmonic number of ~ 8.

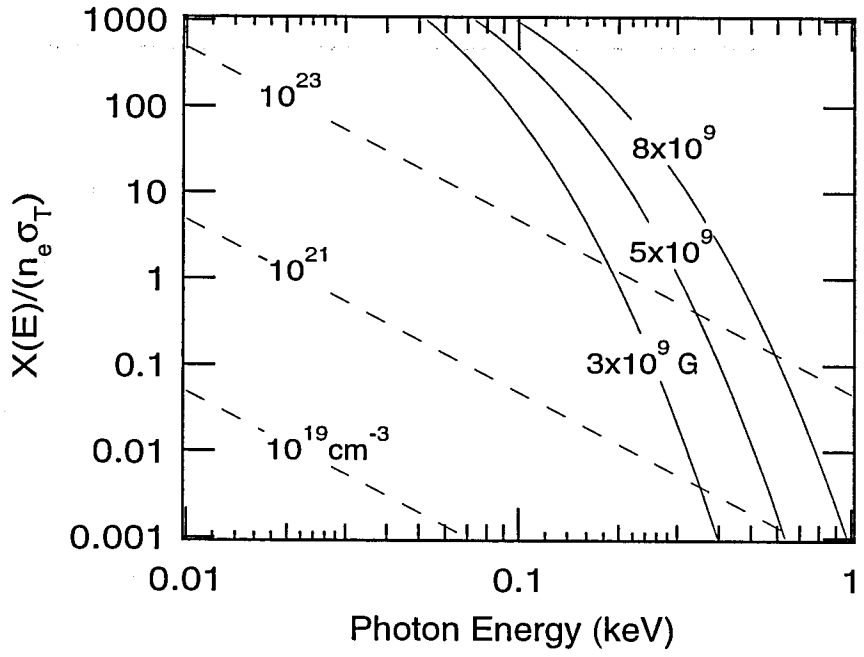

Figure 4.2: The absorption coefficient for cyclotron self-absorption (solid lines) and for thermal bremsstrahlung (dashed lines), in units of the inverse electron scattering mean free path, for an electron temperature of $T_e = 10$ keV, and for a variety of magnetic field strengths and electron densities.

Compton Scattering

The soft photons injected into the magnetosphere and HCC are Comptonized by the hot electrons there. Because the energy of the photons injected into the Comptonizing medium is much smaller than the electron temperature there, the emerging radiation spectrum is largely independent of the details of the injected spectrum and is well approximated by the expression (Shapiro, Lightman, & Eardly 1976; see also Katz 1976; Sunyaev & Titarchuk 1980)

$$H(E) \sim \begin{cases} E^{3+m}, & E < k_B T_e \\ E^3 \exp(-E/k_B T_e), & E > k_B T_e \end{cases} , \tag{4.20}$$

where

$$m \equiv -\frac{3}{2} - \sqrt{\frac{9}{4} + \frac{4}{y}} . \tag{4.21}$$

and

$$y \equiv \frac{4k_B T_e}{m_e c^2} \max\{\tau, \tau^2\}. \tag{4.22}$$

The simple "unsaturated Comptonization" model of LMXB X-ray spectra (see, e.g., White et al. [1986, 1988]) is motivated by the spectrum (4.20).

In the following calculations we model Compton scattering by solving iteratively the radiative transfer equation and its zeroth and first moments derived by Psaltis & Lamb (1997a; see also Chapter 2) using the generalization of the method of variable Eddington factors described in Psaltis & Lamb (1997b; see also Chapter 3). The zeroth and first moments of the transfer equation to first order in $E/m_e c^2$ and $T_e/m_e c^2$, for a static, spherically symmetric medium are

$$\begin{aligned} \frac{\partial H_E^r}{\partial r} + \frac{2}{r} H_E^r &= \eta_E - \chi_E J_E \\ &\quad + n_e \sigma_T \left[E \frac{\partial}{\partial E} \left(\frac{4k_B T_e - E}{m_e c^2} \right) + \frac{k_B T_e}{m_e c^2} E^2 \frac{\partial^2}{\partial E^2} E \right] J_E \end{aligned} \tag{4.23}$$

$$\begin{aligned} \frac{\partial K_E^{rr}}{\partial r} + \frac{3}{r}(K_E^{rr} - J_E) &= -\chi_E H_E^r - n_e \sigma_T H_E^r - \frac{2}{5} n_e \sigma_T \left[\left(\frac{k_B T_e - 3E}{m_e c^2} \right) \right. \\ &\quad \left. + E \frac{\partial}{\partial E} \left(\frac{4k_B T_e - E}{m_e c^2} \right) + \frac{k_B T_e}{m_e c^2} E^2 \frac{\partial^2}{\partial E^2} E \right] H_E^r \, , \end{aligned} \tag{4.24}$$

where J_E, H_E^r, and K_E^{rr} are the zeroth, first, and second moments of the monochromatic specific intensity of the radiation field and η_E and χ_E are the emission and absorption coefficients for Cyclotron emission and absorption. We close the system of equations by introducing the variable Eddington factors $f_E = K_E^{rr}/J_E$. We first solve the moment equations for the zeroth and first moment of the specific intensity of the radiation field, with the variable Eddington factors set equal to some initial guess. We then solve the radiative transfer equation (eq. [A8] of Psaltis & Lamb [1997a]; see also Appendix A) having evaluated the scattering integral using the moments of the specific intensity of the radiation field obtained above. We then update the variable Eddington factors and repeat the whole procedure until convergence is achieved.

We expect induced scattering to be important at low photon energies ($\lesssim$1 keV) in the coronae of LMXBs because the photon occupation number at these photon energies is comparable to unity for the physical conditions of interest (Miller & Lamb 1992). However, induced scattering is unimportant at energies $\gtrsim$1 keV and hence alters only slightly the shape and colors of the calculated X-ray spectra at these energies. For simplicity we shall neglect the terms that describe induced Compton scattering in the calculations presented here. On the other hand, induced scattering must be taken into account in calculating the photon-energy dependence of the r.m.s. amplitudes of the NBO (see Miller & Lamb 1992), because these amplitudes are affected by small differences in the X-ray spectra.

4.4 The Region of Radial Inflow

Radial accretion onto weakly magnetic neutron stars has been analyzed by Miller (1990) in the Newtonian limit and by Park & Miller (1991) in general relativity. The structure of the region of nearly radial inflow has been discussed in detail by Fortner (1992; see also Lamb 1989). Here we summarize the key results of these studies.

4.4.1 Structure of the Region of Radial Inflow

Size of the region—When the total luminosity of the neutron star, the HCC, and the inner disk becomes comparable to the Eddington critical luminosity L_E, the outward radiation force drives plasma out of the disk, forming an extensive inner disk corona (Lamb 1991; Fortner 1992). Radiation drag then removes the azimuthal and vertical momentum from the plasma in the inner disk corona in less than one orbit, creating a region of approximately radial inflow. The outer radius of this region can be estimated by considering the interaction of radiation with the plasma and demanding that the azimuthal radiation drag can remove all the angular momentum of the accreting matter in less than one orbit. Such an estimate gives an upper limit to the extent of

the region of approximately radial inflow (Lamb 1989; Fortner 1992) of

$$R_{\rm RF} \simeq 250\,(1-\epsilon)^2 \left(\frac{0.05}{\epsilon}\right)\ {\rm km}\,, \tag{4.25}$$

where

$$\epsilon \equiv \frac{L_{Edd} - L}{L_{edd}}. \tag{4.26}$$

The fraction μ_r of the total mass accretion rate that can be removed from the accretion disk by radiation drag is limited by the amount of angular momentum that can be carried away by the photon flux. Fortner (1992) has showed that at most a fraction equal to $(GM_{\rm NS}/R_{\rm NS}c^2) \sim 0.3$ of the total mass flux can be removed from the accretion disk.

Temperature Profile—Compton heating and cooling of the electrons in the region of nearly radial inflow is very efficient. The characteristic time for Compton heating and cooling in the radial flow is (Lamb 1989; see also Pozdnyakov, Sobol, & Sunyaev 1983)

$$t_{\rm C} \equiv \frac{3m_e c}{32\pi\sigma_T J} \simeq 4\times10^{-7}\left(\frac{R_{\rm RF}}{100\ {\rm km}}\right)\left(\frac{L}{10^{38}\ {\rm erg\ s^{-1}}}\right)^{-1}\left(\frac{\tau_{\rm RF}}{5}\right)^{-1}{\rm s}\,, \tag{4.27}$$

where $\tau_{\rm RF}$ is the electron scattering optical depth of the radial flow and L is the luminosity of the source. The Compton time is much shorter than any other characteristic time around the neutron star (e.g., the dynamical time scale is $\sim 10^{-3}$ s) and therefore the electron temperature in this region is maintained equal to the local Compton temperature (see Lamb 1989)

$$k_{\rm B}T_{\rm C} \equiv \frac{\langle E^2\rangle}{4\langle E\rangle}\,, \tag{4.28}$$

where the sharp angles indicate averages of the photon energy E and its square E^2 over the photon distribution. Previous studies (see Miller & Lamb 1992; Psaltis et al. 1995; Litchfield & Kylafis 1996) have shown that the Compton temperature in the region of radial inflow is ~ 1 keV.

Velocity Profile—The exact structure of the velocity profile in the accreting gas depends on the details of the radiative transfer and, in particular, on the degree of isotropy of the radiation field, i.e., on the radial profiles of the variable Eddington factors in the flow (Miller 1990; Fortner 1992; Yin & Miller 1995). In general, Miller (1990; see also Park & Miller [1991] and Fortner [1992]) has shown that the flow around a compact object that is accreting radially at a near-critical mass accretion rate has three characteristic regions.

In the outermost of the three regions, the radial velocity of the accreting gas is small and hence the radiation flux in the frame comoving with the gas is sub-critical. As a result the inward radial velocity of the accreting gas is equal to the modified free-fall velocity

$$\frac{V_{\rm mff}}{c} = \sqrt{\frac{\epsilon G M_{\rm NS}}{R c^2}} \simeq 0.6 \epsilon^{1/2} \left(\frac{R_g / R_{\rm NS}}{0.2} \right)^{1/2} \left(\frac{R}{R_{\rm NS}} \right)^{-1/2} . \tag{4.29}$$

In the middle of the three regions, the radiation flux in the frame comoving with the gas becomes comparable to the critical flux, the net force on the accreting gas vanishes, and hence the inward radial velocity of the gas remains approximately constant and equal to

$$\frac{V_{\rm c}}{c} \simeq \frac{\epsilon}{2} . \tag{4.30}$$

Finally, inside the radius at which the flow becomes optically thick to electron scattering, the radiation flux in the frame comoving with the gas becomes super-critical, the flow is decelerated, and the inward radial velocity of the gas decreases linearly with decreasing radius.

For the purposes of our calculations we shall use the analytic expression for the velocity profile derived by Miller (1990; his equation [2.25]).

Density Profile—Assuming a steady state and given a velocity profile in the region of radial accretion we calculate the electron density profile using the equation of

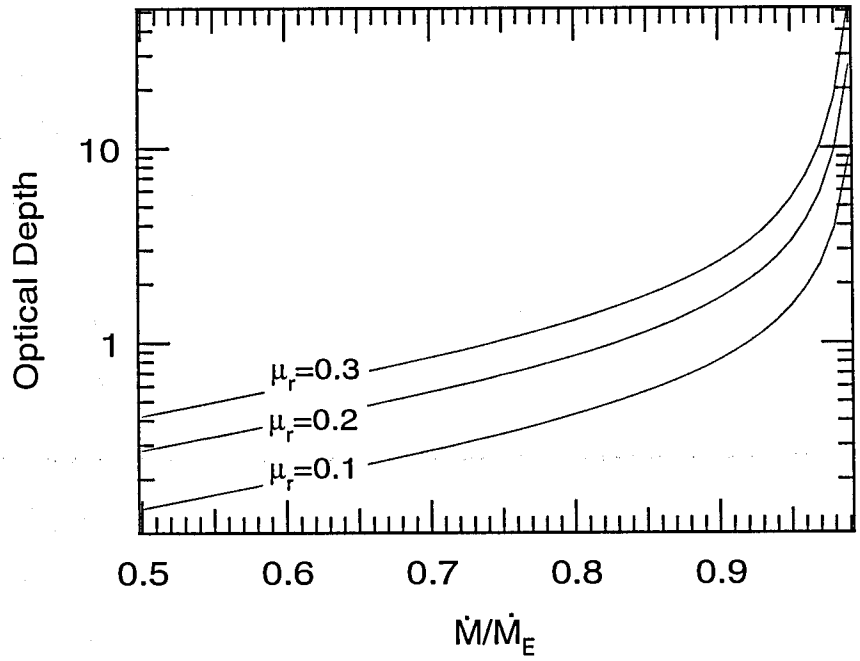

Figure 4.3: The radial electron scattering optical depth in the region of radial inflow measured from infinity to $R_{\rm HCC} = 2R_{\rm NS}$, as a function of the mass accretion rate. The parameter μ_r gives the fraction of the total mass flux that is accreted onto the neutron star through the region of radial inflow.

continuity

$$n_e(r) = \frac{\mu_r \dot{M}}{4\pi r^2 V^r} \,, \tag{4.31}$$

where V^r is the inward radial velocity of the accreting gas. In writing equation (4.31) we have assumed that all the mass that is accreted via the region of radial inflow leaves the disk at the radius $R_{\rm RF}$.

Figure 4.3 shows the radial electron scattering optical depth in the region of radial inflow from infinity to $R_{\rm HCC} = 2R_{\rm NS}$, for different mass accretion rates and fractions μ_r. As the mass accretion rate increases and becomes comparable to $\dot{M}_E$, radiation forces brake the accretion flow and the electron scattering optical depth of the region of radial inflow increases sharply with $\dot{M}$.

4.4.2 Radiation Processes

Compton scattering of photons by fast moving electrons is the dominant radiation process in the region of nearly radial inflow.

The electron temperature in the radial flow is $\sim$ 1 keV and therefore, if the electrons had no bulk velocity, soft X-ray photons with energies $\ll$ 1 keV would gain energy from the electron thermal motion, whereas harder X-ray photons with energies $\gg$ 1 keV would loose energy to the electrons. As a result, if the electron bulk velocity were negligible, Compton scattering by the electrons in the radial flow would produce a "peak" at the spectrum around $\sim 1-2$ keV. However, Comptonization of the photons by the fast moving electrons affects the X-ray spectrum in two ways (see Psaltis & Lamb 1997b; see also Chapter 3). First, the propagation of photons against the infalling electrons leads to a systematic displacement of the radiation spectrum towards higher photon energies; this effect is described by the terms in the transfer equation that are first order in the electron bulk velocity. Second, the systematic increase of the energy of the photons with the number of scatterings leads to the formation of a high-energy tail in the radiation spectrum; this effect is described by the terms that are second order in the electron bulk velocity. Both effects dominate Comptonization by the thermal electrons and as a net result the X-ray spectrum becomes harder in the region of radial inflow, in agreement with the Monte Carlo results of Litchfield & Kylafis (1996).

As in the case of the hot central corona, in the following calculations we model Compton scattering in the region of nearly radial inflow by solving iteratively the radiative transfer equation for a moving medium and its zeroth and first moments derived by Psaltis & Lamb (1997a; see also Chapter 2) using the generalization of the method of variable Eddington factors described in Psaltis & Lamb (1997b; see also Chapter 3).

4.5 The X-ray Spectra of Z Sources

The X-ray spectrum of a Z source depends primarily on the strength of the neutron star magnetic field and the mass accretion rate. Since we are not trying to solve the coupled radiation hydrodynamic problem of the accretion disk, boundary layer, HCC, and radial flow, in the spectral model described in this and following sections we introduce a number of simplifications that allow us to determine the X-ray spectrum of a Z source.

For the magnetic-field strengths and accretion rates of interest here, a fraction of the accretion luminosity is released near the neutron star, where the accreting gas interacts with the stellar surface. The electron temperature in this region must be larger than the electron temperature in the HCC, otherwise the electron scattering optical depth and temperature in the HCC required to account for the accretion luminosities of the Z sources result, because of Comptonization, in countrate spectra that are significantly harder than the observed countrate spectra. Note here that emission from very near the neutron-star surface is also required in the model proposed by Miller et al. (1997) to explain the properties of the kilohertz QPOs.

At the outer surface layers of the neutron star, cyclotron emission and self-absorption dominates thermal bremsstrahlung even when the electron density is up to four orders of magnitude higher than in the HCC (see Fig. 4.3). Therefore, the energy spectrum of photons emitted near the neutron star surface is largely that of self-absorbed cyclotron emission that is truncated typically at $\lesssim$1 keV. The emiting layer is also expected to be geometrically thin in the radial direction so that Comptonization of the soft photons within this layer do not deform the power-law spectra produced by Comptonization in the HCC that has a different electron temperature. As a result the magnetic-field strength and emission and absorption coefficients are expected to be uniform in this region. In order to model the emission of this layer we set the flux $F_{\rm NS}(E)$ emerging from the neutron star surface at a given photon energy

E equal to a truncated Rayleigh-Jeans spectrum (see, e.g., Hartmann et al. 1988), i.e., equal to

$$F_{\rm NS}(E)dE \equiv 4\pi H_{\rm NS}(E)dE = \frac{2\pi}{c^2h^3}k_{\rm B}T_e^{\rm NS}E^2\left(1-e^{-\tau_{\rm NS}X_{\rm cyc}}\right)dE\,, \qquad (4.32)$$

where $X_{\rm cyc}$ is the absorption coefficient for cyclotron self-absorption in units of the inverse photon mean-free path to electron scattering, $\tau_{\rm NS}$ is the electron scattering optical depth of the region in which the emission originates, and h is Planck's constant.

In order to model the transport of radiation in the HCC, we assume that the electron temperature $T_e^{\rm HCC}$ and electron density $n_e^{\rm HCC}$ are uniform at all radii between $R_{\rm NS}$ and $R_{\rm HCC}$. In order to model the transport of radiation in the region of radial inflow, we calculate the electron velocity and density profiles at all radii between $R_{\rm HCC}$ and $R_{\rm RF}$, for a given mass accretion rate $\dot{M}$ and mass fraction μ_r, as outlined in the previous section and calculate self-consistently the electron temperature $T_e^{\rm RF}$ using equation (4.28). For the calculations of the electron velocity and density profiles in the radial flow, we set the mass and radius of the neutron star equal to $1.4M_\odot$ and 10 km respectively.

In order to test our model X-ray spectra with observations we convolve them with the response of an X-ray detector and then compare the predicted countrate spectrum directly to the observations (see Gorenstein et al. 1968). For comparing our theoretical X-ray spectra and colors with observations we also need to take into account the effects of interstellar extinction. Here, we use the coefficients for interstellar extinction given by Morrison & McCammon (1983) and the energy response matrix of the ME detector of the *EXOSAT* satellite (see Turner et al. 1981).

4.5.1 Constraints on the Model Parameters

For a given neutron-star magnetic field and mass accretion rate, our model spectra depend, in principle, on the following parameters: the electron temperature $T_e^{\rm NS}$ and electron scattering optical depth $\tau_{\rm NS}$ of the emiting layer near the neutron star surface,

the radius $R_{\rm HCC}$, electron temperature $T_e^{\rm HCC}$, and electron scattering optical depth $\tau_{\rm HCC}$ of the HCC, and the radius $R_{\rm RF}$ and fraction μ_r of the total mass accretion rate of the radial flow. In this section we demonstrate that the model spectra at energies $\sim 2-15$ keV are determined mainly by the Compton $y^{\rm HCC}$ parameter of the hot central corona and the fraction μ_r of the mass flux through the region of nearly radial inflow and depend very weakly on the remaining parameters.

Neutron-star surface layer—For the magnetic-field strengths that are typical for the Z sources, $\tau_{\rm NS}X_{\rm cyc} \ll 1$ at $\gtrsim$1 keV and therefore cyclotron emission is negligible at these photon energies. Furthermore, because the spectrum of cyclotron photons (eq. [4.32]) follows the low-energy (Rayleigh-Jeans) part of the Planck function, the electron temperature $T_e^{\rm NS}$ and scattering optical depth $\tau_{\rm NS}$ determine mainly the normalization and high-energy cut-off of this spectrum and not its detailed shape. As a result, the shape of the X-ray spectrum of a Z source at energies $E \gtrsim 1$ keV depends only very weakly on $T_e^{\rm NS}$ and $\tau_{\rm NS}$. We shall therefore set $\tau_{\rm NS} = 5$, which corresponds to a collumn density of ~ 12 g cm^{-3}, throughout the following calculations and calculate iteratively $T_e^{\rm NS}$ and the spectrum of the source until the energy-integrated luminosity that emerges from the system is equal to the accretion luminosity $L_{\rm acc} = GM_{\rm NS}\dot{M}/R_{\rm NS}$. The electron temperature $T_e^{\rm NS}$ is typically found to be $\sim 15-20$ keV.

Hot central corona—We can constrain significantly the possible values of the radius $R_{\rm HCC}$, electron temperature $T_e^{\rm HCC}$, and electron scattering optical depth $\tau_{\rm HCC}$ of the HCC using the following observational and theoretical arguments.

The absence of any appreciable periodic oscillations at the spin frequency of the neutron star in LMXBs (see Mereghetti & Grindlay 1987; Wood et al. 1991; Vaughan et al. 1994) can be explained in the context of the unified model if the HCC completely engulfs the magnetosphere of the neutron star. For neutron star magnetic fields $\sim 10^9-10^{10}$ G the characteristic size of the magnetosphere is a few neutron star radii (Ghosh & Lamb 1992) and hence the size $R_{\rm HCC}$ of the hot central corona must be

comparable to the size of the neutron star[1].

The attenuation of the amplitude of a beaming oscillation passing through a spherically symmetric scattering medium of optical depth $\tau_{\rm HCC}$ is given approximately by $A \simeq 1/(1+\tau_{\rm HCC})$ (Brainerd & Lamb 1987; see Kylafis & Phinney 1989 for a more general expression). The electron scattering optical depth in the HCC must therefore be

$$\tau_{\rm HCC} \gtrsim 4 \left(\frac{A^{-1}-1}{0.2^{-1}-1} \right) \tag{4.33}$$

so that electron scattering in the HCC can suppress the amplitude of brightness oscillations at the spin frequency of the neutron star by a factor of at least $A^{-1} \sim 5$, possibly making them undetectable with current instruments. The lower limit given by equation (4.33) is shown as a dotted line in Figure 4.4, which depicts the $T_e^{\rm HCC} - \tau_{\rm HCC}$ parameter space for the Z sources.

The fact that the observed X-ray spectra of Z sources sources are relatively flat (see for example White et al. 1986) suggests that Comptonization in the HCC is unsaturated and hence the value of the Compton $y^{\rm HCC}$ parameter in the HCC is close to unity. To quantify this argument, we use the approximate Comptonization model spectrum given by equation (4.20). First, we require the Compton $y^{\rm HCC}$ parameter in the HCC to be ≤ 5 so that Comptonization is not saturated—the value 5 used here is very conservative as can be seen in Figure 4.8 below. Second, we fold the approximate photon spectrum through the response of the *EXOSAT* ME detector, and compute the $(6.00 - 19.78$ keV$)/(2.86 - 6.00$ kev) X-ray colors defined by Schulz et al. (1989; this hard X-ray color is mostly independent of the effects of interstellar absorption) for a range of electron temperatures and electron scattering optical depths. The observed values of this X-ray color for the Z sources are $\sim 0.2 - 0.3$ (Schulz et al. 1989). In order to allow for the approximations made in deriving equation (4.20)

[1]Recent *RXTE* observations of microsecond time-lags in the kilohertz QPO of the atoll source 4U 1608-52 reveal that the size of the Comptonizing region in this source is indeed similar to the size of the neutron star (Vaughan et al. 1997).

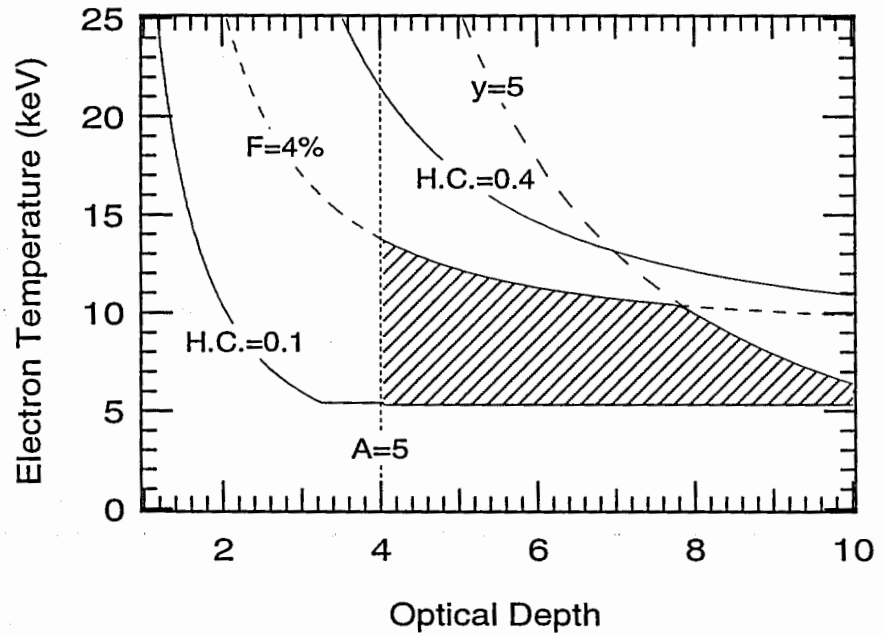

Figure 4.4: Limits on the parameter space of the electron temperature $T_e^{\rm HCC}$ and electron scattering optical depth $\tau_{\rm HCC}$ in the hot central corona. For the amplitudes of beaming oscillations in the HCC to be attenuated by more than a factor of 5, the optical depth in the HCC should be to the right of the dotted line. For the hard X-ray colors of the Z sources to be consistent with *EXOSAT* observations, the electron temperature and optical depth in the HCC should lie within the two solid lines. For Comptonization not to be saturated in the HCC, the electron temperature and optical depth in the HCC should lie below the long-dashed line. Finally, for the energy flux above 30 keV to be consistent with high-energy observations of Z sources, the electron temperature and optical depth in the HCC should lie below the short-dashed line. The shaded area shows the region of the parameters space that is consistent with observations of Z sources.

we require that the electron temperature and electron scattering optical depth in the HCC result in X-ray colors that range between $0.1 - 0.4$; the range of allowed values of $T_e^{\rm HCC}$ and $\tau^{\rm HCC}$ are shown in Figure 4.4. Note that when the electron temperature is $\lesssim$5 keV, the exponential cut-off of the countrate spectrum occurs at low photon energies and therefore the X-ray color is smaller than ~ 0.1 for all optical depths, as long as Comptonization is unsaturated.

The model X-ray spectra should also meet the requirement imposed by high-energy observations of some Z sources that the radiation flux above 30 keV is $\lesssim$1% of the

bolometric flux (Barret & Vedrenne 1994). Figure 4.4 shows the resulting upper limits on the electron temperature and optical depth in the HCC for the flux above 30 keV to be $\lesssim 4\%$ of the bolometric flux, where again we have allowed for uncertainties in the approximations made in deriving equation (4.20); in calculating these last limits we have assumed that the radiation flux at energies ≤ 1 keV is negligible.

Figure 4.4 shows that the electron temperature in the HCC of a Z source is $\sim 5-10$ keV and the electron scattering optical depth in the HCC is $\sim 4-8$, in agreement with our calculations of the heating and cooling rates in the HCC, discussed in §4.3.1.

Radial Flow—The radius $R_{\rm RF}$ of the radial flow is approximately ~ 250 km (see equation [4.25]). At these large radii, the photon mean-free path $\lambda_{\rm mfp}$ for electron scattering is

$$\frac{\lambda_{\rm mfp}}{R_{\rm RF}} = \frac{1}{n_e \sigma_T R_{\rm RF}} \sim 10 \mu_r^{-1} \epsilon^{1/2} \left(\frac{\dot{M}}{\dot{M}_E}\right)^{-1} \left(\frac{R_g/R_{\rm NS}}{0.2}\right)^{1/2} \left(\frac{R_{\rm RF}}{250\ {\rm km}}\right)^{1/2} \qquad (4.34)$$

and hence the effect on the X-ray spectrum of Compton scattering at these radii is negligible, independent of the exact value of $R_{\rm RF}$. We shall therefore set $R_{\rm RF} = 30 R_{\rm NS}$ throughout our calculations.

Finally, the fraction μ_r of the mass flux through the region of radial flow is constrained between zero and ~ 0.3 as discussed in §4.4.

4.5.2 A Reference Model

Figure 4.5 shows the result of a typical radiative transfer calculation for a neutron star with dipole magnetic moment 7×10^{27} G cm^{-3} that is accreting matter at a rate $0.97\ \dot{M}_{\rm E}$, 27% of which is accreted through the region of radial flow (i.e., $\mu_r = 0.27$; the reason for choosing this particular parameters will become obvious later in this section). The neutron star is assumed to be surrounded by a HCC with optical depth 3.0, electron temperature 5 keV, and $R_{\rm HCC} = 2.5 R_{\rm NS}$ km.

Near the stellar surface, the photon flux peaks sharply at $E_{\rm max}$. At photon energies lower than $E_{\rm max}$ the photon flux follows the Rayleigh-Jeans spectrum because at

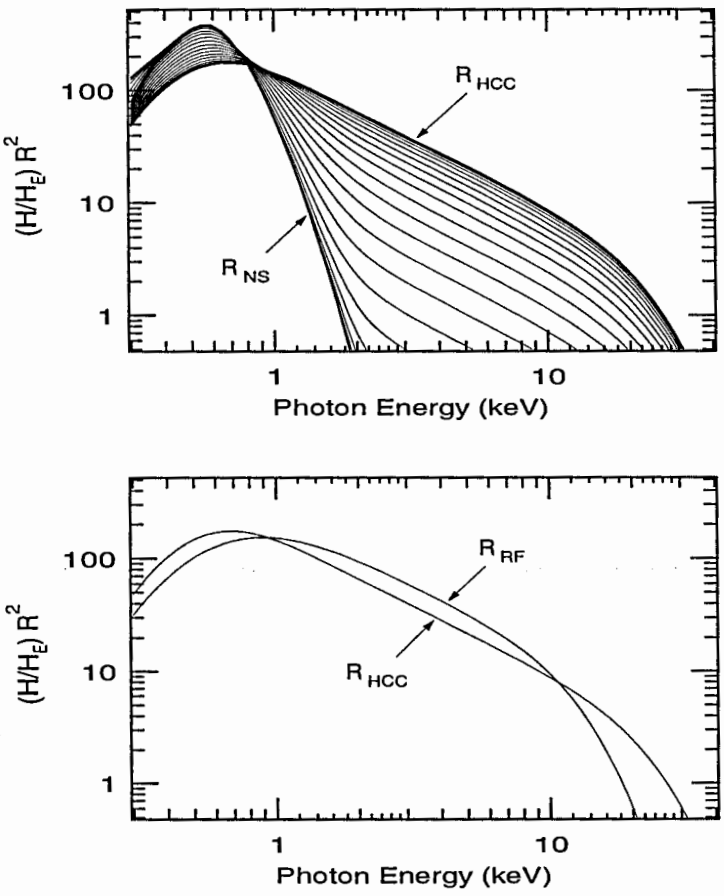

Figure 4.5: The evolution of the radiation flux (a) in the hot central corona and (b) in the region of radial inflow around a neutron star with dipole magnetic moment 7×10^{27} G cm^{-3} that is accreting matter at a rate 0.97 $\dot{M}_{\rm E}$, 27% of which is accreted through the region of radial inflow (i.e., $\mu_{\rm r} = 0.27$). The HCC has optical depth 3.0, electron temperature 5 keV, and $R_{\rm HCC} = 2.5 R_{\rm NS}$.

these energies the cyclotron absorption photon mean-free path is much smaller than $R_{\rm HCC}$. On the other hand, at photon energies higher than $E_{\rm max}$ the photon flux drops rapidly because the emission of cyclotron photons is very inefficient at these very high-harmonic numbers. A few kilometers above the stellar surface a high energy tail is formed as photons gain energy by scattering off hot electrons. As a result, the emerging radiation spectrum has a peak at $\sim E_{\rm max}$ and a power-law tail at higher energies with an exponential cut-off at $\sim 3T_e$. In the region of nearly radial inflow the spectrum is further deformed as the photons mainly gain energy from the bulk

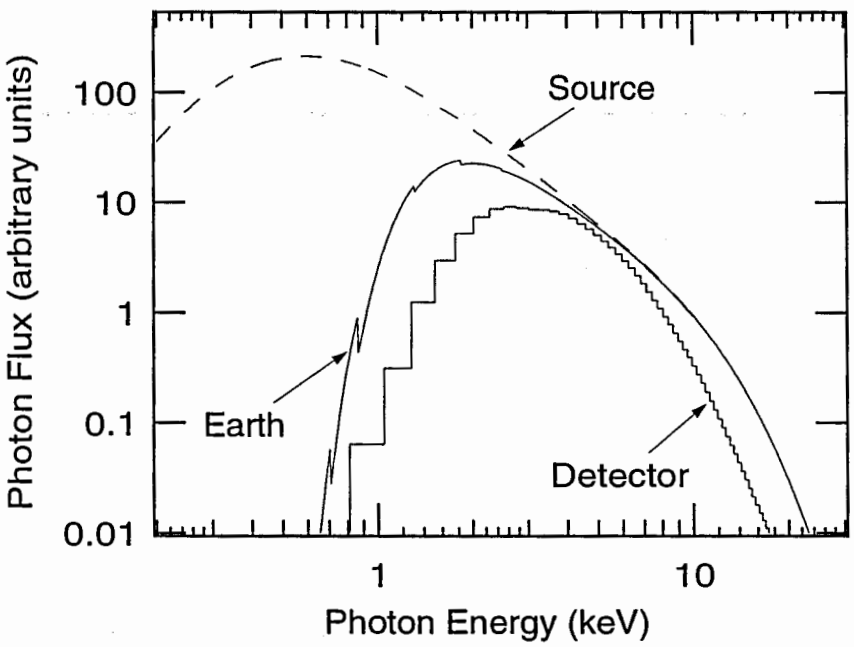

Figure 4.6: The X-ray spectrum of a Z source (for the same parameters as in Figure 4.5) as seen at the source, at earth (for a hydrogen column density of 1.7×10^{22} cm^{-2}), and as observed by the *EXOSAT* ME detector.

kinetic energy of the electrons.

The model spectrum that was calculated above, as emitted at the Z source, is shown in Figure 4.6, together with the spectrum at earth (for a hydrogen column density of 1.7×10^{22} cm^{-2}) and the observed countrate spectrum. Note that for electron temperatures $\gtrsim$5 keV, which are typical for the Z sources, the high-energy cut-off of the photon spectrum occurs at photon energies $\gtrsim$10 keV. At these energies, the quantum efficiency of the *EXOSAT* ME detector is very small and hence the countrate spectra and X-ray colors of Z sources observed with *EXOSAT* are insensitive to the exact energy of this cut-off.

In Figure 4.7 we compare the simulated spectrum with a countrate spectrum of Cyg X-2 observed by EXOSAT (see Kuulkers et al. 1996 for the details of the observation). Note that, although we have not formally fitted the observations, we found an excellent agreement between the spectral model and the observed spectrum

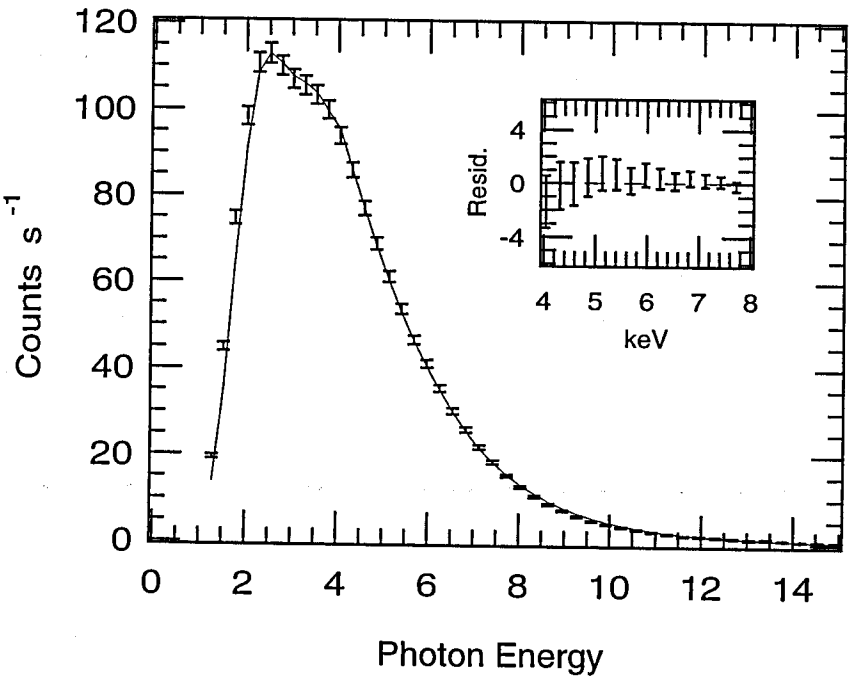

Figure 4.7: The simulated count-rate spectrum for our reference mode (solid line) and the countrate spectrum of Cyg X-2 (error bars) as observed by *EXOSAT*.

for the model parameters we chose—the χ^2 per degree of freedom is $\sim$1.9. The residuals of the comparison of the model to the countrate spectrum also show that there is no evidence for an emission line at $6-7$ keV.

4.5.3 Parameter Study

As we discussed in §4.2, the spectral and timing properties of a Z source at any given moment are, in principle, determined by the neutron-star magnetic field strength and the mass accretion rate. In the simplified model we present here, the shape of the X-ray spectrum between 2–15 keV of a neutron star of given dipole magnetic moment $\mu_{\rm d}$ accreting matter at rate $\dot{M}$ depends mainly on the Compton $y^{\rm HCC}$ parameter of the hot central corona and the fraction μ_r of the mass flux in the region of nearly radial inflow. The remaining parameters either affect the shape of the X-ray spectrum at energies $\lesssim$2 keV or its normalization.

When the optical depth of the region of nearly radial inflow is $\ll 1$, the slope

of the X-ray spectrum between $2 - 10$ keV depends mainly on the Compton $y^{\rm HCC}$ parameter of the hot central corona. On the other hand, the high-energy cut-off of the spectrum is determined by the electron temperature $T_e^{\rm HCC}$ in the hot central corona. However, as we demonstrated in §5.1, the quantum efficiency of the *EXOSAT* ME detector drops fast above ~ 10 keV and therefore the *EXOSAT* X-ray colors depend mainly on the Compton $y^{\rm HCC}$ parameter and not on the optical depth or electron temperature of the hot central corona individually.

When the Compton $y^{\rm HCC}$ parameter in the hot central corona increases, the absolute value of the power-law index of the radiation spectrum decreases (see equations [4.20] and [4.22]) and therefore the spectrum become harder. For large values of the Compton $y^{\rm HCC}$ parameter ($\gtrsim 3$), the spectrum cannot be described by a power-law with a higher energy cut-off and a prominent peak develops at energies $\sim 3k_{\rm B}T_e$ in the energy spectrum. Figure 4.8 shows the effect on the X-ray spectrum of the variation of the Compton $y^{\rm HCC}$ parameter of the hot central corona.

The development of a radial inflow outside the hot central corona increases the efficiency of the upscattering of photons, because photons gain energy by scattering off fast moving electrons. As a result, when the fraction μ_r of the mass flux in the radial flow or the total mass accretion rate $\dot{M}$ increases, the energy and countrate spectra become harder. Figure 4.9 shows the effect on the X-ray spectrum of the variation of the fraction μ_r of the mass flux in the radial flow and of the total mass accretion rate $\dot{M}$.

Figure 4.10 shows the variations of the simulated X-ray colors when the parameters of the spectral model are varied as discussed above and compares it with the Z pattern of Cyg X-2. In plotting Figure 10 we used the *EXOSAT* soft ($3.2 - 4.7$ keV$/0.9 - 3.2$ keV) and hard ($6.4 - 19.1$ keV$/6.4 - 4.7$ keV) X-ray colors defined by Hasinger & van der Klis (1989) to characterize the simulated and observed countrate spectra.

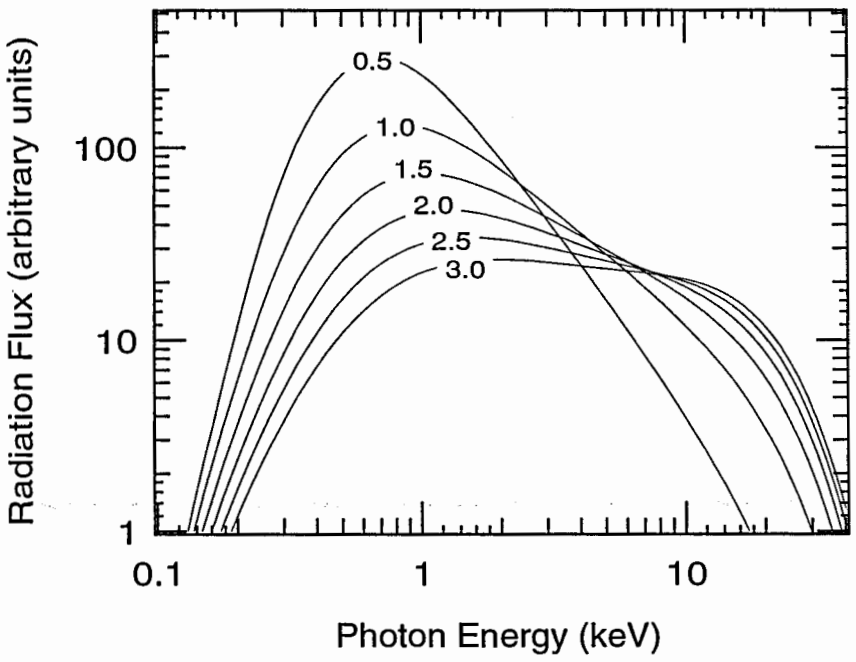

Figure 4.8: X-ray spectra of Z sources for different values of the Compton $y^{\rm HCC}$ parameter in the hot central corona; the remaining parameters are the same as in Figure 4.5.

4.5.4 Dependence on Mass Accretion Rate

In the Z sources, the mass accretion rate onto the neutron star is expected to be within a factor of two below $\dot{M}_{\rm E}$. When the mass accretion rate increases, the accretion flow around the neutron star changes in two ways. First, a region of nearly radial inflow develops outside the hot central corona and inner disk with a mass flux through this region that is expected to increase monotonically with increasing mass accretion rate. Second, the outward radiation force becomes comparable to the gravitational force, the ion temperature that is required to support the HCC becomes smaller, the heating rate of the electrons in the HCC is reduced and at the same time the photon energy density in the HCC is increased. As a result the electron temperature $T_e^{\rm HCC}$ and hence the Compton $y^{\rm HCC}$ parameter in the HCC decrease (see eq. [4.8]).

The increase of μ_r and the decrease of $y^{\rm HCC}$ with increasing mass accretion rate

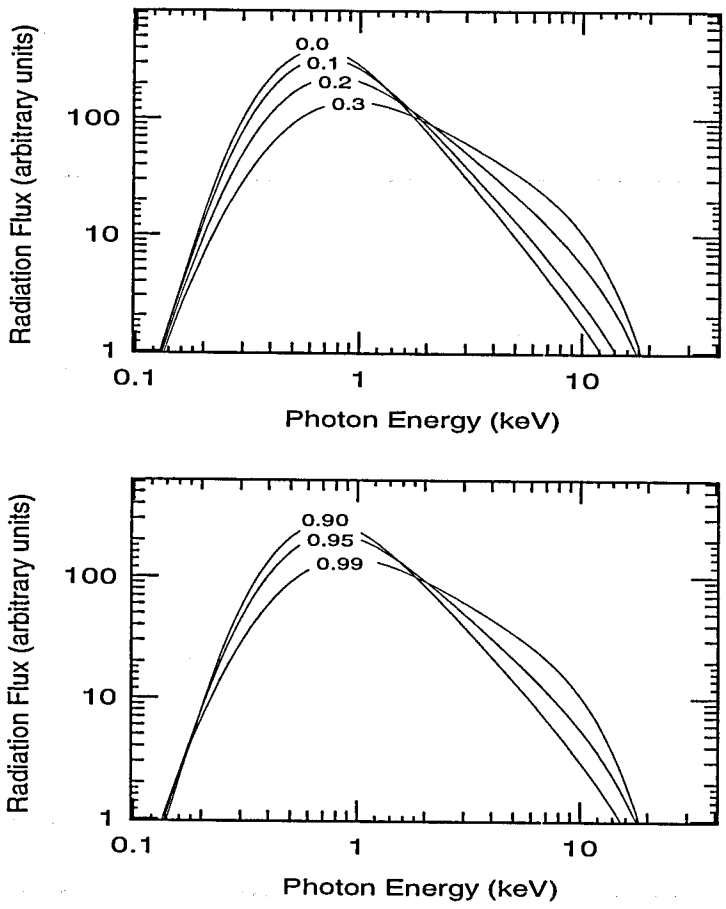

Figure 4.9: X-ray spectra of Z sources for different values (a) of the fraction μ_r of the total mass flux that is accreted onto the neutron star via the radial flow and (b) of the total mass accretion rate $\dot{M}/\dot{M}_{\rm E}$; the remaining parameters are the same as in Figure 4.5).

affect both the photon flux as well as the soft and hard X-ray colors of the source. Detailed modeling of the variation of μ_r and $y^{\rm HCC}$ with mass accretion rate depends very sensitively on the unknown heating rates in the hot central corona and is beyond the scope of the current work. On the other hand, because the model countrate spectra between $\sim 1 - 15$ keV depend mainly on only three parameters, we can use the observed soft and hard X-ray colors as well as the observed countrates of Cyg X-2 to estimate the variation of these three parameters along the Z pattern and check for consistency with the constraints and estimates given in the previous sections. The resulting values of μ_r, $y^{\rm HCC}$, and $\dot{M}$ required to model the horizontal

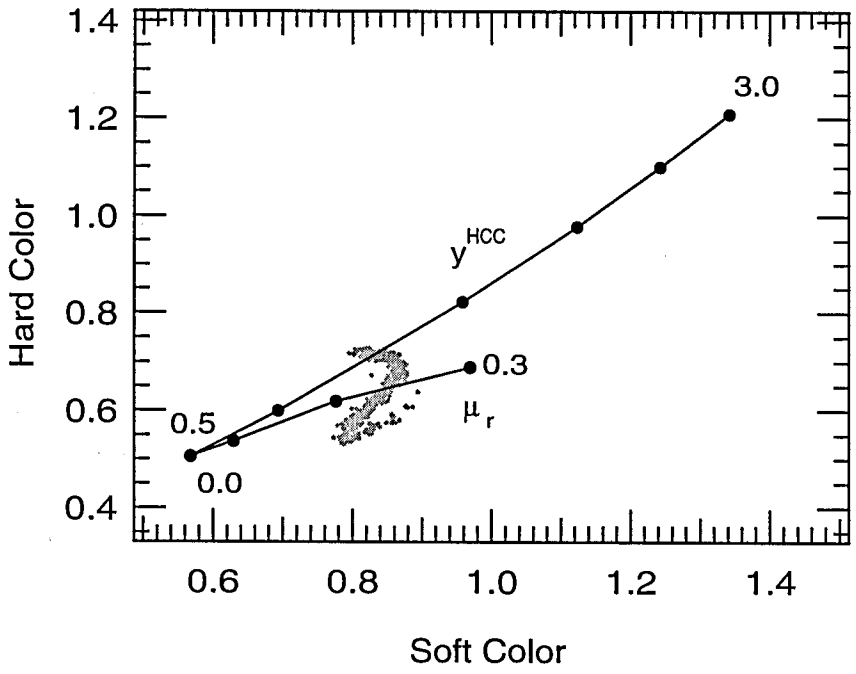

Figure 4.10: Simulated X-ray colors of Z sources for the different Compton $y^{\rm HCC}$ parameters and fractions μ_r shown in Figures 4.8 and 4.9. The color-color diagram of Cyg X-2 (light dots) is shown for comparison.

and normal branches of Cyg X-2 are plotted in Figure 4.11 and the color-color and hardness-countrate diagrams are shown in Figure 4.12.

There are two basic characteristics of the resulting variation of the model parameters with rank number evident in Figure 4.11: (a) all parameters vary monotonically with rank number following the general trends discussed above and (b) the transition from the horizontal to the normal branch occurs when the behavior of the upscattering efficiency of Comptonization of soft photons by hot electrons in the HCC changes. The latter is actually a generic feature of Comptonization models of the Z patterns, as can be seen in the models of Psaltis et al. (1995), Litchfield & Kylafis (1996), as well as in the ones of Schulz et al. (1989) and Schulz & Wijers (1993), and is largely independent of the details of the spectral models.

When the mass accretion rate onto the neutron star comes within $\sim 1-2\%$ of

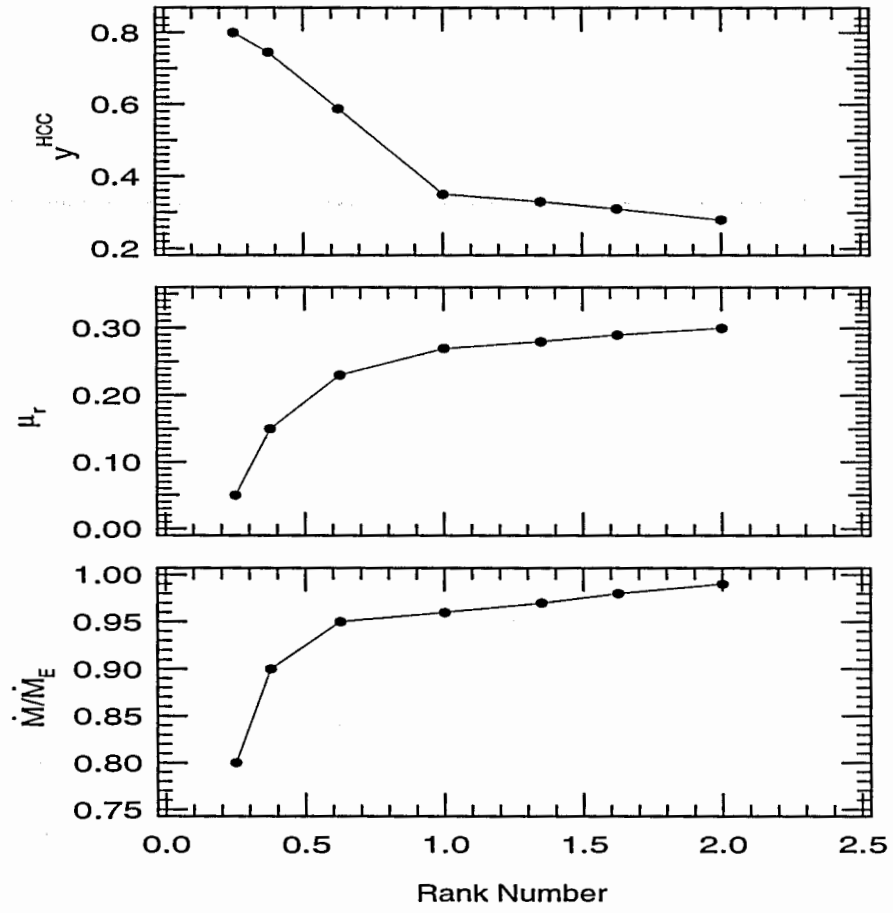

Figure 4.11: The values of y^{HCC}, μ_r, and $\dot{M}$ that are required to model the horizontal and normal branches of Cyg X-2.

$\dot{M}_E$ or even when it becomes larger than $\dot{M}_E$, the accretion flow is expect to be time-dependent and highly variable as radiation will escape through regions of smaller electron density and fingers of matter will surge down onto the neutron star. Our time-independent, spherically symmetric spectral models are inadequate to describe such a phase. Generally speaking though, the electron scattering optical depth in the region of radial inflow increases very fast with increasing mass accretion rate when $\dot{M} \sim \dot{M}_E$ (see Figure 4.3). As a result, upscattering of photons by the bulk velocity of the electrons in the radial flow becomes very efficient (although the bulk velocity of the electron decreases) and therefore the spectrum is expected to become harder again, producing the flaring branch of the Z sources.

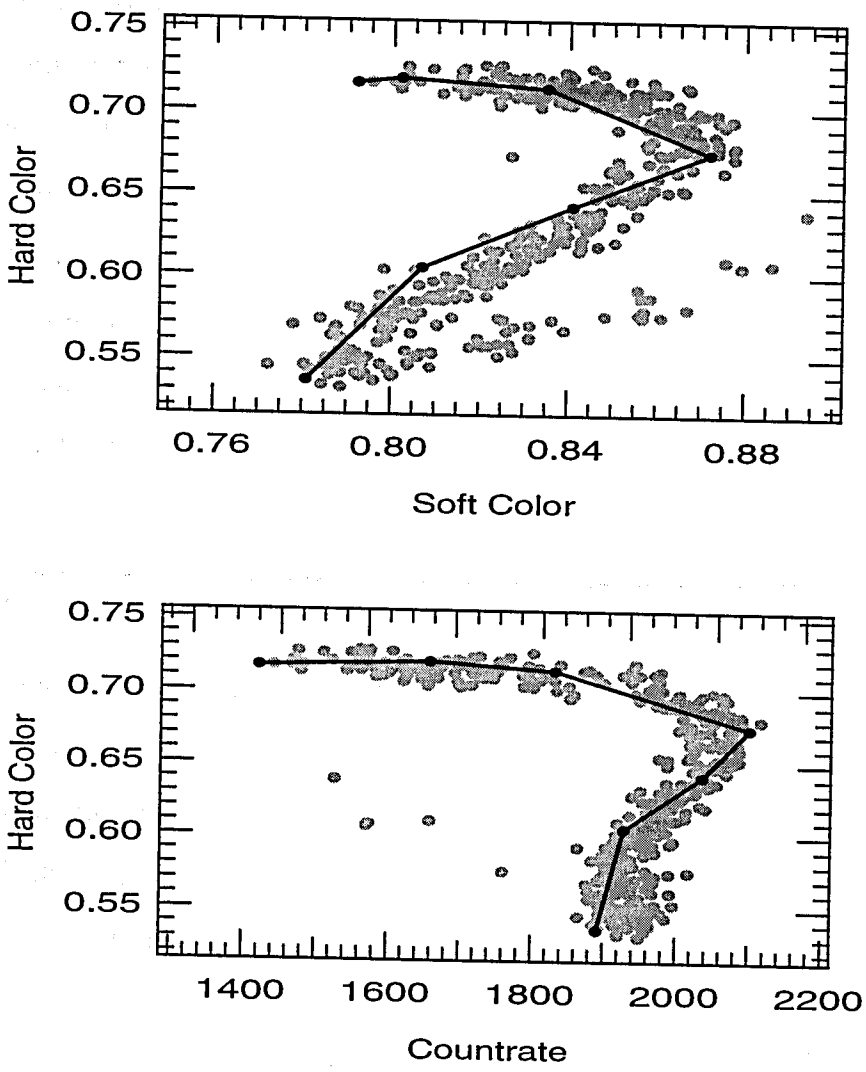

Figure 4.12: The simulated (lines) and observed (grey points) color-color and hardness-countrate diagrams of Cyg X-2.

The results plotted in Figures 4.11 and 4.12 are in general agreement with the results obtained by Psaltis et al. (1995) and by Litchfield & Kylafis (1996). There exist though a number of differences between these studies. Psaltis et al. (1995) did not consider the effects of Comptonization by the bulk electron flow in the region of nearly radial inflow. This resulted in spectral parameters that did not vary monotonically with rank number; it also required electron scattering optical depths in the region of nearly radial inflow that were unphysically high for the mass accretion rates considered

(see Litchfield & Kylafis 1996). Litchfield & Kylafis (1996) modeled the transport of radiation only in the region of nearly radial inflow and therefore neglected the effect of backscattering of photons from the radial flow back to the hot central corona, which increases the upscattering efficiency of Comptonization. For this reason, they managed to keep the hard color constant in the horizontal branch while increasing the mass accretion rate through the radial flow. When the backscattering of photons from the radial flow to the hot central corona is taken into account, the Compton y^{HCC} parameter has to decrease along the horizontal branch for the hard color to remain constant.

4.5.5 Dependence on Neutron Star Magnetic Field Strength

The accretion flow around the neutron star in sources with weaker neutron-star magnetic field strengths differs from the model outlined above in two aspects. First, cyclotron emission from the neutron star surface layers and the magnetosphere becomes optically thin at a lower photon energy (see Fig. 4.2). As a result, the soft X-ray spectrum of the source ($\lesssim$1 keV) peaks at a lower photon energy. Second, the efficiency of cyclotron cooling in the hot central corona decreases with decreasing magnetic field strength (see equation [4.8]). Therefore the Compton $y^{\rm HCC}$ parameter in the hot central corona is expected to increase and the countrate spectra to become, on average, harder with decreasing neutron star magnetic field strength.

Figure 4.13 shows the dependence of the *EXOSAT* hard color (defined by Schulz et al. 1989) on the $y^{\rm HCC}$ parameter (in plotting Fig. 4.13 we set the remaining parameters of the spectral model equal to the parameters obtained above for modeling the soft vertex in Cyg X-2). Figure 4.14 on the other hand shows the dependence of the relative size of the horizontal branch on the Compton $y^{\rm HCC}$ parameter in the hot central corona and the dipole magnetic moment of the neutron star. In plotting Figure 4.14 we used the same values for the remaining parameters of the spectral

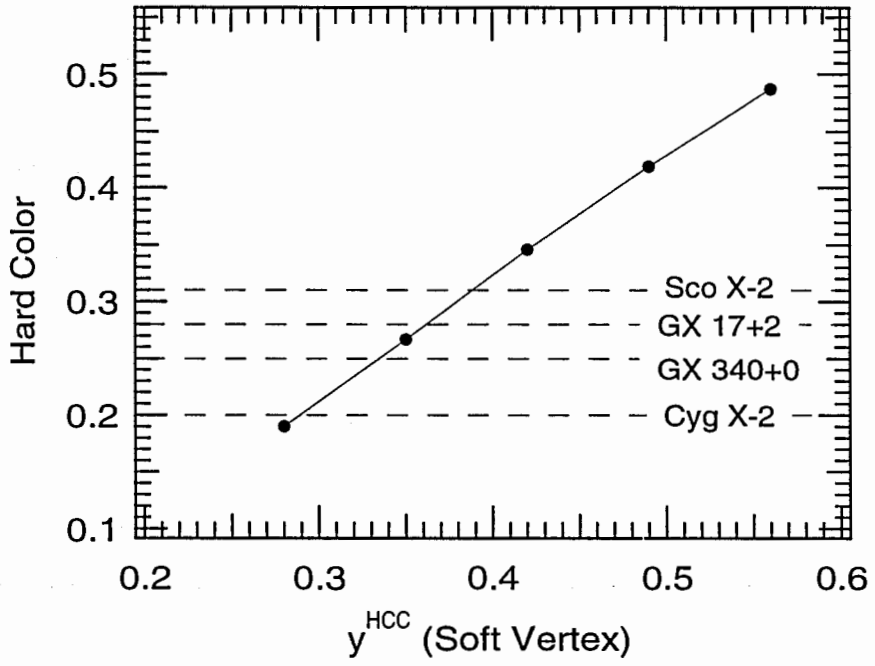

Figure 4.13: *EXOSAT* hard colors of Z sources (as defined by Schulz et al. 1989) for different values of the y^{HCC} parameter in the hot central corona; the remaining parameters of the spectral model were set equal to the parameters required for modeling the soft vertex of Cyg X-2. The observed hard X-ray colors of the soft verteces of four Z sources are also marked with dashed lines for comparison.

model as in Figure 4.12 and calculated the relative size of the horizontal branch as $2(SC_2-SC_1)/(SC_2+SC_1)$, where SC_1 and SC_2 are the soft colors (as defined by Hasinger & van der Klis 1989 for Cyg X-2) at the extremes of the horizontal branch. Both figures demonstrate that the Z sources with weaker neutron-star magnetic field strengths have on average harder X-ray spectra and shorter horizontal branches.

4.6 Discussion

In the previous sections we presented the results of detailed numerical simulations of the transport of radiation around weakly magnetic, accreting neutron stars according to the unified model of their X-ray spectral and temporal characteristics. In this section we discuss the consistency of our model parameters with the rapid variability

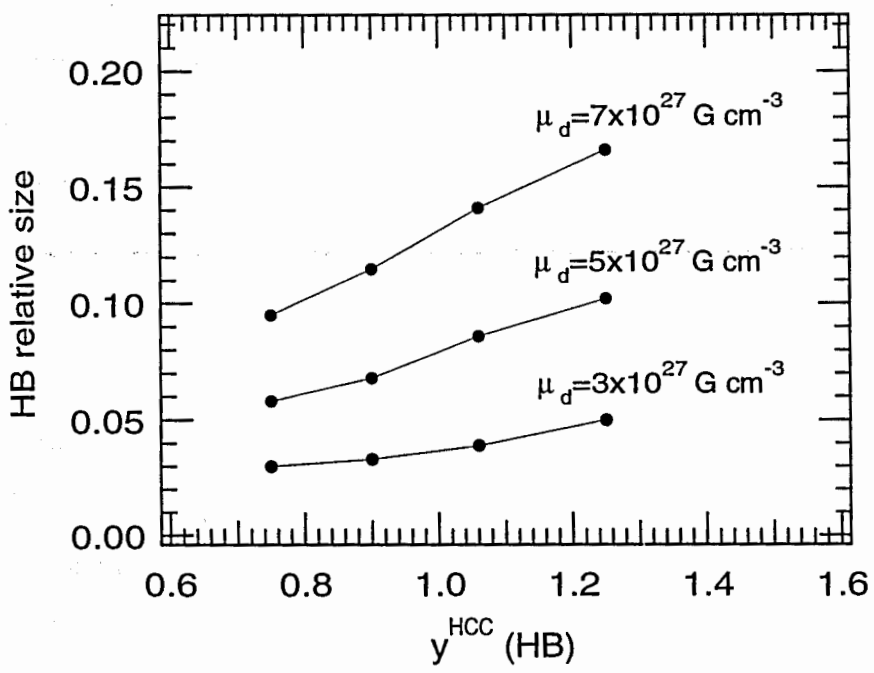

Figure 4.14: The relative size (defined in the text) of the horizontal branches of Z source for different neutron-star dipole magnetic moments μ_d and maximum Compton y^{HCC} parameters (i.e., at the leftmost points of the horizontal branches) in the hot central corona.

of Z sources, the differences between the spectral and rapid variability characteristics of the various Z sources, as well as the possible detection of emission lines in their X-ray spectra.

4.6.1 Consistency with Models of Rapid Variability

In the spirit of the unified model (see Lamb 1989), we require the spectral calculations discussed above to be consistent with previous models of the rapid variability of Z sources.

The values of the Compton y^{HCC} parameter in the HCC required to model the observations of Cyg X-2 at low mass-accretion rates imply that the electron scattering optical depth in the HCC is

$$\tau \simeq 3.9 \left(\frac{y^{HCC}}{0.7}\right)^{1/2} \left(\frac{T_e^{HCC}}{6}\right)^{-1/2} , \qquad (4.35)$$

where we have used a value for the electron temperature in the HCC that is consistent with our simple estimates for the heating and cooling of the electrons there (see §4.3.1). As the mass accretion rate increases, the radial electron scattering optical depth from infinity to the stellar surface increases further because of the development of the region of nearly radial inflow. Therefore, our spectral calculations are consistent with the models for the absence of any detectable, periodic brightness oscillations in the observations of Z sources (Brainerd & Lamb 1987; Kylafis & Phinney 1989).

The magnetospheric beat-frequency model for the HBO requires that the dipole magnetic fields of the Z sources are $\sim 10^9$ G (see Ghosh & Lamb 1992). Furthermore, the decrease of the HBO frequency with increasing mass accretion rate observed in GX 17+2 (Wijnands et al. 1996) and in Cyg X-2 (Wijnands et al. 1997), when these sources were in their normal branches, set upper limits on their stellar magnetic dipole moments of $\sim 5\times10^{27}$ and 8×10^{27} G cm^3 respectively. These magnetic field strengths are consistent with the upper limits on the dipole magnetic moments of the neutron stars estimated in the previous section from our spectral models.

Finally, in the radiation-hydrodynamic model of the N/FBO, oscillations become weakly damped and appear as QPOs only when the mass accretion rate becomes within a few percent of $\dot{M}_E$, and in particular when $\mu_r > 6\epsilon$ (Fortner et al. 1989; Fortner 1992). Figure 4.15 shows the dependence of μ_r on ϵ along the Z pattern for Cyg X-2 as well as the condition for the radiation-hydrodynamic modes in the region of radial inflow to become weakly damped and demonstrates that the N/FBO is expected to become observable in the middle of the normal branch, in agreement with observations.

4.6.2 Two types of Z sources

As we discussed in detail in §4.2.1, recent analysis of archival *EXOSAT* data (Kuulkers 1995) has confirmed the suggestion of Hasinger & van der Klis (1989) that the Z

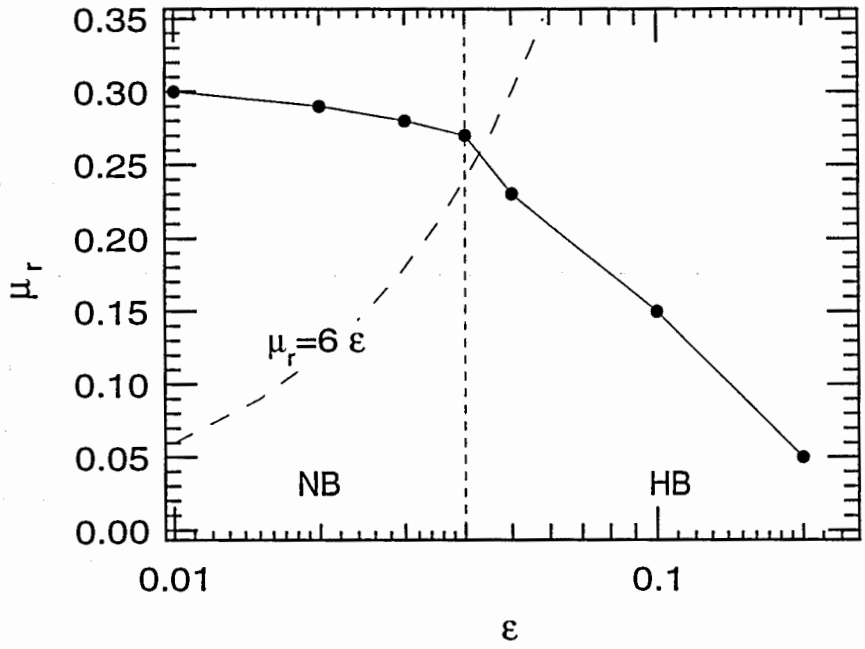

Figure 4.15: The variation of the fraction μ_r of the total mass flux that is accreted through the region of radial inflow with ϵ along the Z pattern of Cyg X-2 (solid line) and the limit for radial radiation-hydrodynamic modes to become weakly damped (dashed line).

sources can be subdivided into two groups: the so-called "Sco-like" and "Cyg-like" sources. Here we suggest that a number of characteristics of the members of these two subgroups can be explained if the "Sco-like" sources have on average weaker magnetic fields than the "Cyg-like" sources.

X-ray Colors— The "Sco-like" sources have on average harder countrate spectra than the "Cyg-like" sources, as it is demonstrated by the average hard colors of these sources at their soft verteces (see Fig. 4.14). At this point on their Z patterns, all sources are believed to accrete matter at near-Eddington mass accretion rates as it is implied by their similar temporal characteristics. We therefore expect their differences in hard X-ray color (which is also unaffected by interstellar extinction) at this point along the Z to be determined by a parameter other than the mass accretion rate. As we discussed in §4.5.5, the higher hard X-ray colors of the "Sco-like" sources suggest

that these Z sources have on average weaker magnetic fields than the "Cyg-like" sources.

Z patterns—Although Hasinger & van der Klis (1989) used slightly different definitions of the X-ray colors for different Z sources and the soft X-ray color of a source depends strongly on the interstellar extinction, it is evident in their color diagrams that the "Sco-like" sources have on average horizontal branches that are $\sim 2-3$ times shorter than the horizontal branches of the "Cyg-like" sources. As we discussed in §4.5.4, this fact can be naturally accounted for in our model if the "Sco-like" sources have neutron-star magnetic field strengths that are ~ 2 times weaker than the field strengths of the "Cyg"-like sources.

Amplitudes of the HBO—HBOs have been detected in all three "Cyg-like" sources with r.m.s. amplitudes $\sim 2-5\%$ (see Hasinger & van der Klis 1989). However, only a weak HBO has been detected from GX 17+2 and no HBO has been detected from Sco X-1 using the *EXOSAT* or *GINGA* satellites (Hasinger & van der Klis 1989; Hertz et al. 1992). More recently, *RXTE* observations of Sco X-1 revealed a very weak HBO with an r.m.s. amplitude of $\sim 1\%$ (van der Klis et al. 1997). According to the beat-frequency model of the horizontal branch oscillations (Alpar & Shaham 1985; Lamb et al. 1985; Shibazaki & Lamb 1987), the HBO is magnetospheric in origin and hence we expect the amplitudes of these oscillations to be correlated with the neutron star magnetic field strength. As a result, the low r.m.s. amplitudes of the HBO in the "Sco-like" sources is consistent with the fact that the "Sco-like" sources have on average weaker magnetic fields strengths than the "Cyg-like" sources.

4.6.3 Emission Lines

As we discussed in §4.2, detection of emission lines at ~ 6.7 keV, as well as at lower ($\lesssim 1$ keV) photon energies, has been reported for a few Z sources (see, e.g., Kuulkers et al. 1997 and reference therein). The resulting emission lines were identified with

iron K and L emission lines but their large FWHM were hard to explain, even when Compton broadening was taken into account (see, e.g., Ponman et al. 1990; Kallman 1995 and references therein).

The reported emission lines in the spectra of Z sources were detected in the residuals of the subtraction of the best-fit continuum spectral models from the observed countrate spectra. In order to investigate the effects of this method on the observed properties of the emission lines, we fitted our calculated X-ray spectrum shown in Figure 4.6 (labeled as the 'source' spectrum) with a simple two-component model that consists of a cut-off power-law plus a blackbody component (as in, e.g., Schulz et al. 1989). We performed the fitting between 0.5 and 15 keV and found that the simple two-component model can describe well the X-ray spectrum shown in Figure 4.6 if the power-law index and temperature for the first component is ~ -1.3 and ~ 5 keV respectively, the blackbody temperature is ~ 0.8 keV, and the ratio of the $2-10$ keV flux of the blackbody to the cut-off power-law component is $\sim 18\%$. These parameters are very similar to the parameters obtained by Schulz et al. (1989) and Hasinger et al. (1990) for Cyg X-2 even though we have not taken into account the biases introduced by the response of the detector or by interstellar extinction. Figure 4.16 shows the result of the fit as well as its residuals, which show 'evidence' for emission lines at energies ~ 0.9 keV and ~ 7 keV. Although the spectrum in Figure 4.6 contains no emission lines, the blackbody component of the spectral model is narrower than the peak in the countrate spectrum at ~ 1 keV that is produced by Comptonization of photons, and hence two additional broad components at the wings of the blackbody are needed to improve the fit. Figure 4.16 demonstrates that the observed properties of emission lines possibly detected in the residuals of spectral fits depend very strongly on the assumed model for the continuum spectrum and even the reported detections of such emission lines may as well be artifacts of this process.

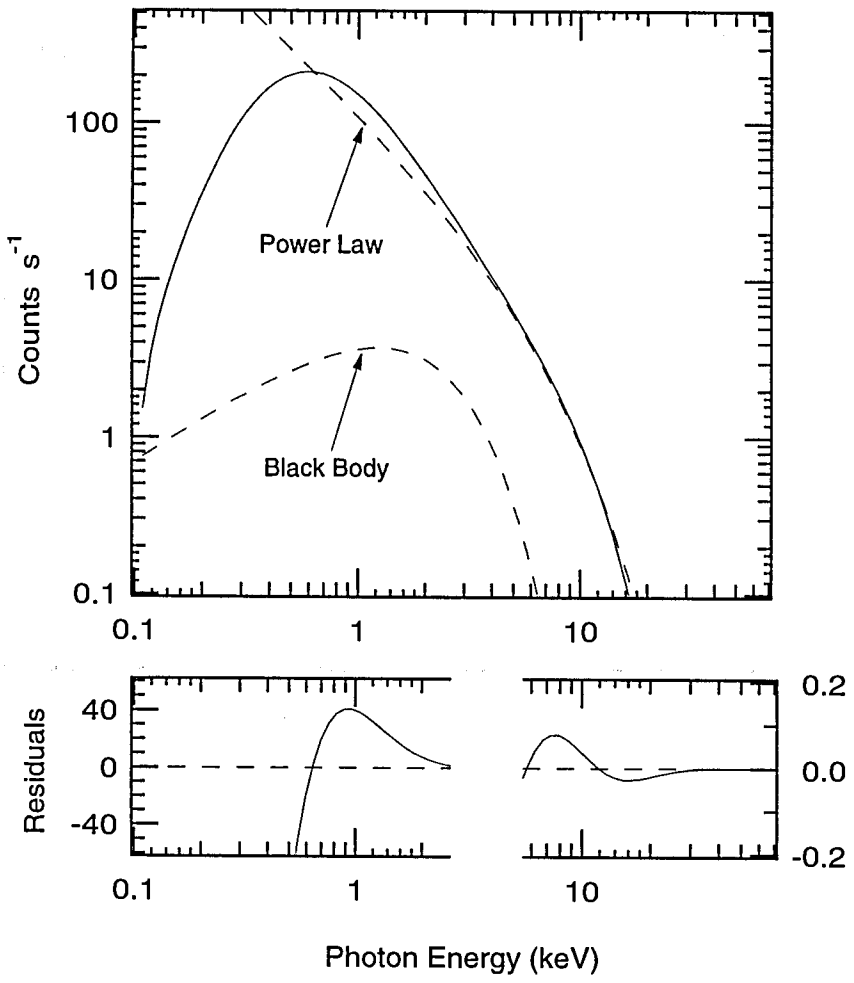

Figure 4.16: The simulated X-ray spectrum of Cyg X-2 at the middle of the normal branch (solid line in upper panel), the two components of the mathematical spectral model that were used to fit it (dashed lines in upper panel), and the residuals of the fit (lower panel).

In conclusion, in this chapter we demonstrated that the X-ray spectra predicted by the unified model are in excellent agreement with the observed $\sim 2-15$ keV countrate spectra of the Z sources and that the resulting model parameters are in agreement with models of their rapid variability. The spectra of these sources at energies $\lesssim 2$ keV depend very strongly on microphysical processes that cannot be treated accurately within the model presented here. Moreover, the spectra at energies $\gtrsim 15$ keV depend on the unknown heating processes in the HCC. A more detailed treatment of either

energy regime requires a self-consistent solution of the equations for the radiation transport and the gas flow and possibly in multiple dimensions. Future observations of Z sources at energies $\lesssim$2 keV and $\gtrsim$15 keV are needed to guide and place constraints on the theoretical modeling. Both types of observations can now be performed either with *ASCA* (at low photon energies) or with the HEXTE experiment on *RXTE* (at high photon energies) and will provide valuable information for the physical conditions very close to the compact objects in Z sources.

Appendix A

Photon Kinetic and Radiative Transfer Equations for Scattering by an Electron Fluid

In this appendix we give the photon kinetic equation and the corresponding radiative transfer equation for scattering by an electron gas with temperature T_e and bulk velocity $\vec{V}$.

We start from the photon kinetic equation (2.27), transform all the quantities to the system frame using equations (2.18)–(2.19), and then average over the electron velocity distribution. The resulting photon kinetic equation is

$$\begin{aligned}\frac{1}{n_e\sigma_T}\left(\partial_t + l^i\partial_i\right)n(\hat{l},\varepsilon) &= \mathcal{R}_1 n(\hat{l},\varepsilon) \\ &+ \frac{3}{4}\left(\mathcal{R}_2 n + \mathcal{R}_3^i n^i + \mathcal{R}_4^{ij} n^{ij} + \mathcal{R}_5^{ijk} n^{ijk} + \mathcal{R}_6^{ijkl} n^{ijkl}\right) \\ &+ \frac{3}{2}\left(\frac{\varepsilon}{m_e}\right) n(\hat{l},\varepsilon)\left(2+\varepsilon\partial_\varepsilon\right)\left(n - l^i n^i + l^i l^j n^{ij} - l^i l^j l^k n^{ijk}\right) ,\end{aligned} \tag{A.1}$$

where

$$\mathcal{R}_1 = -1 + 2\frac{\varepsilon}{m_e} + \left(\hat{l}\cdot\vec{V}\right) , \tag{A.2}$$

$$\begin{aligned}\mathcal{R}_2 &= 1 + 2\frac{\varepsilon}{m_e} + \frac{\varepsilon}{m_e}\varepsilon\partial_\varepsilon + 2\frac{T_e}{m_e} - \left(\hat{l}\cdot\vec{V}\right) + \left(\hat{l}\cdot\vec{V}\right)^2 - V^2 \\ &+ \varepsilon\partial_\varepsilon\left[4\frac{T_e}{m_e} - \left(\hat{l}\cdot\vec{V}\right) + \left(\hat{l}\cdot\vec{V}\right)^2\right] + \frac{1}{2}\varepsilon^2\partial_\varepsilon^2\left[2\frac{T_e}{m_e} + \left(\hat{l}\cdot\vec{V}\right)^2\right] ,\end{aligned} \tag{A.3}$$

$$\mathcal{R}_3^i = -2\frac{\varepsilon}{m_e}l^i - \frac{\varepsilon}{m_e}\varepsilon\partial_\varepsilon l^i - 4\frac{T_e}{m_e}l^i + 2V_i - 2\left(\hat{l}\cdot\vec{V}\right)l^i - 2\left(\hat{l}\cdot\vec{V}\right)^2 l^i + 2V^2 l^i$$
$$+\varepsilon\partial_\varepsilon\left[-4\frac{T_e}{m_e}l^i + V_i - 4\left(\hat{l}\cdot\vec{V}\right)V_i + 2\left(\hat{l}\cdot\vec{V}\right)^2 l^i\right]$$
$$+\frac{1}{2}\varepsilon\partial_\varepsilon^2\left[-2\frac{T_e}{m_e}l^i - 2\left(\hat{l}\cdot\vec{V}\right)V_i\right], \tag{A.4}$$

$$\mathcal{R}_4^{ij} = l^i l^j + 2\frac{\varepsilon}{m_e}l^i l^j + \frac{\varepsilon}{m_e}\varepsilon\partial_\varepsilon l^i l^j - 6\frac{T_e}{m_e}l^i l^j + \left(\hat{l}\cdot\vec{V}\right)l^i l^j - 2l^i V_j$$
$$+\left(\hat{l}\cdot\vec{V}\right)^2 l^i l^j - 8\left(\hat{l}\cdot\vec{V}\right)l^i V_j - 3V^2 l^i l^j + 4V_i V_j$$
$$+\varepsilon\partial_\varepsilon\left[4\frac{T_e}{m_e}l^i l^j - \left(\hat{l}\cdot\vec{V}\right)l^i l^j + 3V_i V_j - \left(\hat{l}\cdot\vec{V}\right)^2 l^i l^j\right]$$
$$+\frac{1}{2}\varepsilon\partial_\varepsilon^2\left[2\frac{T_e}{m_e}l^i l^j + V_i V_j + \left(\hat{l}\cdot\vec{V}\right)^2 l^i l^j\right], \tag{A.5}$$

$$\mathcal{R}_5^{ijk} = -2\frac{\varepsilon}{m_e}l^i l^j l^k - \frac{\varepsilon}{m_e}\varepsilon\partial_\varepsilon l^i l^j l^k + 4\frac{T_e}{m_e}l^i l^j l^k$$
$$+4l^i l^j V_k - 8\hat{l}^i V_j V_k + 4\left(\hat{l}\cdot\vec{V}\right)l^i l^j V_k$$
$$+\varepsilon\partial_\varepsilon\left[-4\frac{T_e}{m_e}l^i l^j l^k + l^i l^j V_k - 4\left(\hat{l}\cdot\vec{V}\right)l^i l^j V_k - 2l^i V_j V_k\right]$$
$$+\frac{1}{2}\varepsilon^2\partial_\varepsilon^2\left[-2\frac{T_e}{m_e}l^i l^j l^k - 2\left(\hat{l}\cdot\vec{V}\right)l^i l^j V_k\right], \tag{A.6}$$

$$\mathcal{R}_6^{ijkl} = 10l^i l^j V_k V_l + 5\varepsilon\partial_\varepsilon l^i l^j V_k V_l + \frac{1}{2}\varepsilon^2\partial_\varepsilon^2 l^i l^j V_k V_l\,. \tag{A.7}$$

The corresponding radiative transfer equation is

$$\frac{1}{n_e\sigma_T}\left(\partial_t + l^i\partial_i\right)I(\hat{l},\varepsilon) = \mathcal{L}_1 I(\hat{l},\varepsilon)$$
$$+\frac{3}{4}\left(\mathcal{L}_2 J + \mathcal{L}_3^i H^i + \mathcal{L}_4^{ij}K^{ij} + \mathcal{L}_5^{ijk}Q^{ijk} + \mathcal{L}_6^{ijkl}R^{ijkl}\right)$$
$$+\frac{3}{4\varepsilon^3}\left(\frac{\varepsilon}{m_e}\right)I(\hat{l},\varepsilon)\,(\varepsilon\partial_\varepsilon - 1)$$
$$\left(J - l^i H^i + l^i l^j K^{ij} - l^i l^j l^k Q^{ijk}\right), \tag{A.8}$$

where

$$\mathcal{L}_1 = -1 + 2\frac{\varepsilon}{m_e} + \left(\hat{l}\cdot\vec{V}\right), \tag{A.9}$$

$$\mathcal{L}_2 = 1 - \frac{\varepsilon}{m_e} + \frac{\varepsilon}{m_e}\varepsilon\partial_\varepsilon + 2\frac{T_e}{m_e} + 2\left(\hat{l}\cdot\vec{V}\right) + 4\left(\hat{l}\cdot\vec{V}\right)^2 - V^2$$
$$+\varepsilon\partial_\varepsilon\left[-2\frac{T_e}{m_e} - \left(\hat{l}\cdot\vec{V}\right) - 2\left(\hat{l}\cdot\vec{V}\right)^2\right] + \frac{1}{2}\varepsilon^2\partial_\varepsilon^2\left[2\frac{T_e}{m_e} + \left(\hat{l}\cdot\vec{V}\right)^2\right], \tag{A.10}$$

$$\mathcal{L}_3^i = \frac{\varepsilon}{m_e}l^i - \frac{\varepsilon}{m_e}\varepsilon\partial_\varepsilon l^i - 4\frac{T_e}{m_e}l^i - V_i - 2\left(\hat{l}\cdot\vec{V}\right)l^i - 8\left(\hat{l}\cdot\vec{V}\right)^2 l^i + 2V^2 l^i$$

$$+\varepsilon\partial_e\left[2\frac{T_e}{m_e}l^i+V_i+2\left(\hat{l}\cdot\vec{V}\right)V_i+2\left(\hat{l}\cdot\vec{V}\right)^2 l^i\right]$$
$$+\frac{1}{2}\varepsilon\partial_e^2\left[-2\frac{T_e}{m_e}l^i-2\left(\hat{l}\cdot\vec{V}\right)V_i\right], \tag{A.11}$$

$$\mathcal{L}_4^{ij} = l^il^j-\frac{\varepsilon}{m_e}l^il^j+\frac{\varepsilon}{m_e}\varepsilon\partial_e l^il^j-6\frac{T_e}{m_e}l^il^j+4\left(\hat{l}\cdot\vec{V}\right)l^il^j-2l^iV_j$$
$$+10\left(\hat{l}\cdot\vec{V}\right)^2 l^il^j-8\left(\hat{l}\cdot\vec{V}\right)l^iV_j-3V^2l^il^j+V_iV_j$$
$$+\varepsilon\partial_e\left[-2\frac{T_e}{m_e}l^il^j-\left(\hat{l}\cdot\vec{V}\right)l^il^j-4\left(\hat{l}\cdot\vec{V}\right)^2 l^il^j\right]$$
$$+\frac{1}{2}\varepsilon\partial_e^2\left[2\frac{T_e}{m_e}l^il^j+V_iV_j+\left(\hat{l}\cdot\vec{V}\right)^2 l^il^j\right], \tag{A.12}$$

$$\mathcal{L}_5^{ijk} = \frac{\varepsilon}{m_e}l^il^jl^k-\frac{\varepsilon}{m_e}\varepsilon\partial_e l^il^jl^k+4\frac{T_e}{m_e}l^il^jl^k$$
$$+l^il^jV_k-2l^iV_jV_k+4\left(\hat{l}\cdot\vec{V}\right)l^il^jV_k$$
$$+\varepsilon\partial_e\left[2\frac{T_e}{m_e}l^il^jl^k+l^il^jV_k+2\left(\hat{l}\cdot\vec{V}\right)l^il^jV_k-2l^iV_jV_k\right]$$
$$+\frac{1}{2}\varepsilon^2\partial_e^2\left[-2\frac{T_e}{m_e}l^il^jl^k-2\left(\hat{l}\cdot\vec{V}\right)l^il^jV_k\right], \tag{A.13}$$

$$\mathcal{L}_6^{ijkl} = l^il^jV_kV_l+2\varepsilon\partial_e l^il^jV_kV_l+\frac{1}{2}\varepsilon^2\partial_e^2 l^il^jV_kV_l\,. \tag{A.14}$$

Appendix B

Emission and Absorption Processes in the System Frame

In the absence of scattering, the transfer equation in the system frame becomes simply (see, e.g., Mihalas & Mihalas 1984, p. 422)

$$\left(\partial_t + l^i \partial_i\right) I(\hat{l}, \varepsilon) = \left(\frac{\varepsilon}{\varepsilon_f}\right)^2 \eta(\varepsilon_f) - \left(\frac{\varepsilon_f}{\varepsilon}\right) \chi(\varepsilon_f) I(\hat{l}, \varepsilon), \tag{B.1}$$

where again the subscript 'f' refers to quantities in the fluid frame and we have for simplicity assumed that the emission coefficient η and the absorption coefficient χ are isotropic in this frame. In writing equation (B.1) we have also used the fact that the absorption and emission coefficients are defined in the fluid frame and that (η/ε^2) and $(\varepsilon\chi)$ are Lorentz invariants.

We can now expand $\eta(\varepsilon_f)$ to second order in $\vec{V}$ as

$$\begin{aligned} \eta(\varepsilon_f) &= \eta[\varepsilon + (\varepsilon_f - \varepsilon)] \\ &\simeq \eta_e + (\varepsilon_f - \varepsilon)\partial_\varepsilon \eta_e + \frac{1}{2}(\varepsilon_f - \varepsilon)^2 \partial_\varepsilon^2 \eta_e \\ &\simeq \eta_e + \left(\frac{1}{2}V^2 - \hat{l}\cdot\vec{V}\right)\varepsilon\partial_\varepsilon\eta_e + \left(\hat{l}\cdot\vec{V}\right)^2 \varepsilon^2 \partial_\varepsilon^2 \eta_e \,, \end{aligned} \tag{B.2}$$

where $\eta_e = \eta(\varepsilon)$. We also expand $\chi(\varepsilon_f)$ in a similar way. The transfer equation to second order in V then becomes

$$\left(\partial_t + l^i \partial_i\right) I(\hat{l}, \varepsilon) = \left\{\left[1 + 2(\hat{l}\cdot\vec{V}) + 3(\hat{l}\cdot\vec{V})^2 - V^2\right]\right.$$

$$+\left[-(\hat{l}\cdot\vec{V})-2(\hat{l}\cdot\vec{V})^2+\frac{1}{2}V^2\right]\varepsilon\partial_\varepsilon+\frac{1}{2}(\hat{l}\cdot\vec{V})^2\varepsilon^2\partial_\varepsilon^2\Big\}\eta_\varepsilon$$
$$-\Big\{\left[1-(\hat{l}\cdot\vec{V})+\frac{1}{2}V^2\right]+\left[-(\hat{l}\cdot\vec{V})+(\hat{l}\cdot\vec{V})^2+\frac{1}{2}V^2\right]\varepsilon\partial_\varepsilon$$
$$+\frac{1}{2}(\hat{l}\cdot\vec{V})^2\varepsilon\partial_\varepsilon\Big\}\chi_\varepsilon I(\hat{l},\varepsilon)\,. \tag{B.3}$$

We can then obtain the zeroth and first moments of the transfer equation,

$$\begin{aligned}\partial_t J+\partial_i H^i &= \eta_\varepsilon-\chi_\varepsilon J+V^iH^i\left[\chi_\varepsilon+\varepsilon\partial_\varepsilon\chi_\varepsilon\right]\\ &\quad-\frac{1}{6}V^2\varepsilon\partial_\varepsilon\eta_\varepsilon+\frac{1}{6}V^2\varepsilon^2\partial_\varepsilon^2\eta_\varepsilon-\frac{1}{2}\chi_\varepsilon JV^2-\left[\frac{1}{2}JV^2+K^{ij}V_iV_j\right]\varepsilon\partial_\varepsilon\chi_\varepsilon\\ &\quad-\frac{1}{2}K^{ij}V_iV_j\varepsilon^2\partial_\varepsilon^2\chi_\varepsilon\end{aligned} \tag{B.4}$$

and

$$\begin{aligned}\partial_t H^i+\partial_j K^{ij} &= -\chi_\varepsilon H^i+\frac{1}{3}V^i\left(2\eta_\varepsilon-\varepsilon\partial_\varepsilon\eta_\varepsilon\right)+K^{ij}V_j\left(\chi_\varepsilon+\varepsilon\partial_\varepsilon\chi_\varepsilon\right)\\ &\quad-\frac{1}{2}\chi_\varepsilon H^iV^2-\left(\frac{1}{2}H^iV^2+Q^{ijk}V_jV_k\right)\varepsilon\partial_\varepsilon\chi_\varepsilon\\ &\quad-\frac{1}{2}Q^{ijk}V_jV_k\varepsilon^2\partial_\varepsilon^2\chi_\varepsilon\,.\end{aligned} \tag{B.5}$$

Blandford & Payne (1981a) added a photon source term to the right side of their transfer equation, without adding any corresponding absorption term. This is fundamentally inconsistent with thermodynamics (if absorption is not included, the photon source can never come into thermodynamic equilibrium with the radiation field). It is equivalent to including the terms on the right sides of equations (B.3)–(B.5) that involve the emission coefficient η_ε but neglecting all the terms that involve the absorption coefficient χ_ε.

Neglecting the absorption terms compared to the emission term is a valid *approximation* only if the specific intensity of the radiation field is negligible compared to the source function $S_\varepsilon=\eta_\varepsilon/\chi_\varepsilon$ *at all photon energies*, i.e., only if self absorption is never important at any energy, anywhere in the system. This is rarely the case in astrophysical systems. For example, it is not the case in the Comptonizing regions around accreting neutron star and black hole X-ray sources.

Neglecting the absorption terms in the transfer equation leads to equations that have a different mathematical character from equations (B.3)–(B.5), because in this case the right sides of the transfer and moment equations do not depend explicitly on the radiation field.

Appendix C

Moments of the Specific Intensity in Spherical Geometry

In defining the moments of the specific intensity in the system frame we shall use the quantities

$$u(z,p,\epsilon) \equiv \frac{1}{2}\left[I^+(z,p,\epsilon) + I^-(z,p,\epsilon)\right] \tag{C.1}$$

and

$$v(z,p,\epsilon) \equiv \frac{1}{2}\left[I^+(z,p,\epsilon) - I^-(z,p,\epsilon)\right] \ . \tag{C.2}$$

The zeroth moment of the specific intensity is then

$$J(r,\epsilon) = \frac{1}{r}\int_0^r u(z,p,\epsilon)dz \ , \tag{C.3}$$

where r depends on z and p through the relation $r^2 = z^2 + p^2$. Because of the assumed spherical symmetry, the only non-zero component of the first moment of the specific intensity is the r–component:

$$H^r(r,\epsilon) = \frac{1}{r^2}\int_0^r zv(z,p,\epsilon)dz \ . \tag{C.4}$$

Similarly, the non-zero components of the second, third, and fourth moments of the specific intensity are

$$\begin{aligned} K^{rr}(r,\epsilon) &= \frac{1}{r^3}\int_0^r z^2 u(z,p,\epsilon)dz \\ K^{\theta\theta}(r,\epsilon) = K^{\phi\phi}(r,\epsilon) &= \frac{1}{2}(J - K^{rr}) \ , \end{aligned} \tag{C.5}$$

$$
\begin{aligned}
Q^{rrr}(r,\epsilon) &= \frac{1}{r^4}\int_0^r z^3 v(z,p,\epsilon)dz \\
Q^{\theta\theta r}(r,\epsilon) = Q^{\theta r\theta}(r,\epsilon) = Q^{r\theta\theta}(r,\epsilon) &= \frac{1}{2}(H^r - Q^{rrr}) \\
Q^{\phi\phi r}(r,\epsilon) = Q^{\phi r\phi}(r,\epsilon) = Q^{r\phi\phi}(r,\epsilon) &= \frac{1}{2}(H^r - Q^{rrr})\ , \\
R^{rrrr}(r,\epsilon) &= \frac{1}{r^4}\int_0^r z^3 u(z,p,\epsilon)dz \\
R^{\theta\theta\theta\theta}(r,\epsilon) &= \frac{3}{8}(J - 2K^{rr} + R^{rrrr}) \\
R^{\phi\phi\phi\phi}(r,\epsilon) &= \frac{3}{8}(J - 2K^{rr} + R^{rrrr}) \\
R^{rr\theta\theta}(r,\epsilon) = R^{r\theta r\theta}(r,\epsilon) = \ldots &= \frac{1}{2}(K^{rr} - R^{rrrr}) \\
R^{rr\phi\phi}(r,\epsilon) = R^{r\phi r\phi}(r,\epsilon) = \ldots &= \frac{1}{2}(K^{rr} - R^{rrrr}) \\
R^{\theta\theta\phi\phi}(r,\epsilon) = R^{\theta\phi\theta\phi}(r,\epsilon) = \ldots &= \frac{3}{8}R^{rrrr}\ . \qquad \text{(C.6)}
\end{aligned}
$$

Appendix D

The Generalized Source Function

Using equation (A1)-(A8) of Appendix A we derive the generalized source function for a spherically symmetric system:

$$S^{\pm}(z,p,\epsilon) \equiv S_1^{\pm} + \frac{\epsilon}{m_e} S_2^{\pm} + \frac{T_e}{m_e} S_3^{\pm} + V S_4^{\pm} + V^2 S_5^{\pm} \,, \tag{D.1}$$

where

$$S_1^{\pm} = \frac{3}{8}\left[3 - \cos\theta^2 + \left(3\cos\theta^2 - 1\right) f^{rr}\right] J \tag{D.2}$$

$$\begin{aligned} S_2^{\pm} = \frac{3}{8}\Big\{ & (-1+\epsilon\partial_\epsilon)\left[3 - \cos^2\theta + \left(3\cos^2\theta - 1\right) f^{rr}\right] J \\ & + (1-\epsilon\partial_\epsilon)\left[5 - 3\cos^2\theta + \left(5\cos^2\theta - 3\right) g^{rr}\right] H^r \cos\theta \Big\} \end{aligned} \tag{D.3}$$

$$\begin{aligned} S_3^{\pm} = \frac{3}{4}\Big\{ & \left[3cos^2\theta - 1 - 3\left(3cos^2\theta - 1\right) f^{rr}\right] J \\ & + 2\left[1 - 3g^{rr} + (5g^{rr} - 3)\cos^2\theta\right] H^r \cos\theta \\ & + \frac{1}{2}\left(-2\epsilon\partial_\epsilon + \epsilon^2\partial_\epsilon^2\right)\left[3 - \cos^2\theta + \left(3\cos^2\theta - 1\right) f^{rr}\right] J \\ & + \frac{1}{2}\left(2\epsilon\partial_\epsilon - \epsilon^2\partial_\epsilon^2\right)\left[5 - 3\cos^2\theta + \left(5\cos^2\theta - 3\right) g^{rr}\right] H^r \cos\theta \end{aligned} \tag{D.4}$$

$$\begin{aligned} S_4^{\pm} = {} & V\cos\theta I + \frac{3}{8} V \Big\{ 4\cos\theta\left[2 - cos^2\theta + \left(3\cos^2\theta - 2\right) f^{rr}\right] J \\ & + \left[-1 - 5\cos^2\theta + \left(3\cos^2\theta - 1\right) g^{rr}\right] H^r \\ & - \cos\theta\partial_\epsilon\left[3 - \cos^2\theta + \left(3\cos^2\theta - 1\right) f^{rr}\right] J \\ & + \partial_\epsilon\left[\frac{1}{2}\left(3 - \cos^2\theta\right) + \left(3\cos^2\theta - 1\right) g^{rr}\right] H^r \Big\} \end{aligned} \tag{D.5}$$

$$S_5^{\pm} = \frac{3}{4} V^2 \Big\{ \Big[-5\cos^4\theta + \frac{21}{2}\cos^2\theta - 1 - 2\cos^2\theta\left(2 - \cos^2\theta\right)\epsilon\partial_\epsilon$$

$$
\begin{aligned}
&\quad + \frac{1}{4}\cos^2\theta\left(3-\cos^2\theta\right)\epsilon^2\partial_\epsilon^2\Big] J \\
&+ \left[4 - 10\cos^2\theta + \left(3+\cos^2\theta\right)\epsilon\partial_\epsilon - \frac{1}{2}\left(3-\cos^2\theta\right)\epsilon^2\partial_\epsilon^2\right]\cos\theta H \\
&+ \Big[\frac{1}{2}\left(30\cos^4\theta - 37\cos^2\theta + 7\right) + 2\left(1-3\cos^4\theta\right)\epsilon\partial_\epsilon \\
&\quad + \frac{1}{2}\left(3\cos^4\theta - 3\cos^2\theta + 4\right)\epsilon^2\partial_\epsilon^2\Big] f^{rr}K^{rr} \\
&+ \left[\left(6\cos^2\theta - 4\right) + \left(3\cos^2\theta - 3\right)\epsilon\partial_\epsilon - \frac{1}{2}\left(3\cos^2\theta - 1\right)\epsilon^2\partial_\epsilon^2\right]\cos\theta g^{rr}H^r \\
&+ \left(2\cos^2\theta - 1\right)\left(1 + 2\epsilon\partial_\epsilon + \frac{1}{2}\epsilon^2\partial_\epsilon^2\right)R^{rrrr}\Big\} \qquad \text{(D.6)}
\end{aligned}
$$

where $cos\theta \equiv z/r$, $f^{rr}(\epsilon) = K^{rr}(\epsilon)/J(\epsilon)$, and $g^{rr}(\epsilon) = Q^{rrr}(\epsilon)/H^r(\epsilon)$.

Appendix E

Coefficients of the Moment Equations

Using equations (2.34) and (2.40) we derive

$$A_1 = n_e\left[\epsilon + V^2\left(\frac{1}{10}\epsilon\partial_\epsilon + \frac{11}{20}\epsilon^2\partial_\epsilon^2\right)f^{rr}\right] - \left[1 + \frac{1}{2}V^2 + \left(f^{rr} + \frac{1}{2}\right)V^2\epsilon\partial_\epsilon + \frac{1}{2}f^{rr}V^2\epsilon^2\partial_\epsilon^2\right]\chi \quad \text{(E.1)}$$

$$A_2 = n_e\left\{\epsilon - 2T_e - \frac{2}{3}V^2 + \left[\frac{1}{10}\left(f^{rr} - \frac{1}{3}\right) + \frac{22}{20}\epsilon\partial_\epsilon f^{rr}\right]V^2\right\} \quad \text{(E.2)}$$

$$A_3 = n_e\left[T_e + \frac{1}{3}V^2 + \frac{11}{20}\left(f^{rr} - \frac{1}{3}\right)V^2\right] \quad \text{(E.3)}$$

$$A_4 = -\frac{2}{\tau_0 - \tau} + V^r\chi + V^r\epsilon\partial_\epsilon\chi \quad \text{(E.4)}$$

$$A_5 = n_e V^r \quad \text{(E.5)}$$

$$C_1 = -\chi S_e + \frac{1}{6}V^2 S_e\left(\epsilon\partial_\epsilon - \epsilon^2\partial_\epsilon^2\right)\chi + \frac{1}{6}V^2\epsilon\left(\partial_\epsilon S_e\right)\left(1 - 2\epsilon\partial_\epsilon\right)\chi - \frac{1}{6}V^2\epsilon^2\left(\partial_\epsilon^2 S_e\right)\chi \quad \text{(E.6)}$$

and

$$B_1 = \frac{1}{10}n_e V^r\left(9f^{rr} - 7 - \epsilon\partial_\epsilon f^{rr}\right) + V^r f^{rr}\left(1 + \epsilon\partial_\epsilon\right)\chi + \partial_{\tau_r} f^{rr} - \frac{3}{\tau_0 - \tau}\left(f^{rr} - \frac{1}{3}\right) \quad \text{(E.7)}$$

$$B_2 = -\frac{1}{10}n_e V^r\left(f^{rr} + 3\right) \quad \text{(E.8)}$$

$$B_3 = n_e\left[-1 + \frac{4}{5}\epsilon - \frac{2}{5}T_e - \frac{5}{10}V^2 + \frac{1}{10}V^2\left(-5 - 3\epsilon\partial_\epsilon - \partial_\epsilon^2\right)g^{rr}\right] - \left[1 + \frac{1}{2}V^2 - V^2\left(g^{rr} + \frac{1}{2}\right)\epsilon\partial_\epsilon - \frac{1}{2}V^2 g^{rr}\epsilon^2\partial_\epsilon^2\right]\chi \quad \text{(E.9)}$$

$$B_4 = n_e\left[-\frac{2}{5}\epsilon+\frac{4}{5}T_e+\frac{9}{10}V^2+\frac{3}{10}V^2\left(-1-\frac{2}{3}\epsilon\partial_\epsilon\right)g^{rr}\right] \quad \text{(E.10)}$$

$$B_5 = n_e\left[-\frac{2}{5}T_e-\frac{1}{10}V^2\left(g^{rr}+1\right)\right] \quad \text{(E.11)}$$

$$C_2 = -\frac{2}{3}V^r\chi S+\frac{1}{3}V^r\chi\epsilon\partial_\epsilon S+\frac{1}{3}V^r S\epsilon\partial_\epsilon\chi\,, \quad \text{(E.12)}$$

where $\tau_0 \equiv \tau(r=0)$ and we have supressed the dependence of the various quantities on spatial position and photon energy.

Appendix F

Parabolic Character of the System of Equations

In this Appendix we follow the procedure outlined by Ames (1992, pp. 8–12) to prove that the system of partial differential equations (3.9) and (3.10) is parabolic.

We define the quantities $L = \partial_E J$ and $M^r = \partial_E H^r$, which together with the partial differential equations (4.23) and (3.10), and the equations for the differentials dJ, dH^r, dL, and dM^r, form an 8×8 system of algebraic equations for the eight derivatives

$$\begin{bmatrix} 1 & & & & & & & \\ & 1 & & & & & & \\ & & 1 & A_3E^2 & & & & \\ f^{rr} & & & & B_5E^2 & & & \\ d\tau_r & & & & & & & \\ & & d\tau_r & & & & & \\ & & & dE & d\tau_r & & & \\ & & & & dE & d\tau_r & & \end{bmatrix} \cdot \begin{bmatrix} \partial_E J \\ \partial_{\tau_r} J \\ \partial_E H^r \\ \partial_{\tau_r} H^r \\ \partial_E L \\ \partial_{\tau_r} L \\ \partial_E M^r \\ \partial_{\tau_r} M^r \end{bmatrix} = \tag{F.1}$$

$$= \begin{bmatrix} L \\ M^r \\ C_1 - A_1 J - A_2 EL - A_4 H^r - A_5 EL \\ C_2 - B_2 EL - B_3 H - B_4 EM^r \\ dJ - LdE \\ dH^r - M^r dE \\ dL \\ dM^r \end{bmatrix} . \tag{F.2}$$

Equating the determinant of the coefficient matrix to zero, we obtain the characteristic

equation for the system of equations,

$$A_3 B_5 E^4 (d\tau_r)^4 = 0 \,, \tag{F.3}$$

from which we obtain that the system has only one multiple, real characteristic direction, i.e., $d\tau_r = 0$. Therefore, the system of partial differential equations (4.23) and (3.10) is parabolic.

Bibliography

Alpar, M. A., Hasinger, G., Shaham, J., & Yancopoulos, S. 1992, A&A, 257, 627

Alpar, M. A. & Shaham, J. 1985, Nature, 316, 239

Ames, W. F. 1992, Numerical Methods for Partial Differential Equations, (Boston: Academic Press, Inc)

Asai, K., Dotani, T., Mitsuda, K., Nagase, F., Kamado, Y., Kuulkers, E., & Breedon, L. M. 1994, PASJ, 46, 479

Babuel-Peyrissac, J. P. & Rouvillois, G. 1969, J. Phys., 30, 301

Barret, D. & Vedrenne, G. 1994, ApJS, 92, 505

Bekefi, G. 1966, Radiation Processes in Plasmas (New York: Wiley)

Belian, R. D., Conner, J. P., & Evans, W. D. 1976, ApJ, 206, L135

Berestetskiĭ, V. B., Lifshitz, E. M., & Pitaevskiĭ, L. P. 1971, Relativistic Quantum Theory, Part 1 (Oxford: Pergamon Press)

Berger, M. et al. 1996, ApJL, 469, L13

Bildsten, L. 1993, ApJ, 418, L21

———. 1995, ApJ, 438, 852

Bildsten, L. & Cutler, C. 1995, ApJ, 449, 800

Bildsten, L., Salpeter, E. E., & Wasserman, I. 1992, ApJ, 384, 143

Bildsten, L., Ushomirsky, G., & Cutler, C. 1996, ApJ, 460, 827

Blandford, R. D. & Payne, D. G. 1981a, MNRAS, 194, 1033

———. 1981b, MNRAS, 194, 1040

Blissett, R. J. & Cruise, A. M. 1979, MNRAS, 186, 45

Brainerd, J. & Lamb, F.K. 1987, ApJ, 317, L33

Chan, K. L. & Jones, B. J. T. 1975, ApJ, 200, 454

Chanmugam, G. & Langer, S. 1991, ApJ, 368, 580

Chanmugam, G., Wu, K., Courtney, M. W., & Barrett, P. E. 1989, ApJS, 71, 323

Chiappetti, L. et al. 1990, ApJ, 361, 596

Christian, D. J. & Swang, J. H. 1997, ApJS, 109, 177

Colpi, M. 1988, ApJ, 326, 233

Davidson, K. & Ostriker, J. P. 1973, ApJ, 179, 585

Dieters, S. & van der Klis, M. 1997, MNRAS, in press

Dieters, S., Vaughan, B. A., Kuulkers, E., & van der Klis, M. 1997, in preparation

Dolan, J. 1972, Astroph. & Sp. Sc. 17, 472

Ebisuzaki, T., Hanawa, T., & Sugimoto, D. 1983, PASJ, 35, 17

Fortner, B. F., Lamb, F. K., & Miller, G. S. 1989, Nature, 342, 775

Fortner, B. F. 1992, PhD Thesis, University of Illinois at Urbana-Champaign

Fukue, J., Kato, S., & Matsumoto, R. 1985, PASJ, 37, 383

Fushiki, I. & Lamb, D. Q. 1987, ApJ, 323, L55

Ghosh, P., & Lamb, F. K. 1992 in X-ray Binaries and Recycled Pulsars, ed. E. P. J. van den Heuvel and S. A. Rappaport (Dordrecht: Kluwer), 487

Giacconi, R., Gursky, H., Kellogg, E., Schreier, E., & Tananbaum, H. 1971, ApJ, 167, L67

Giacconi, R., Gursky, H., Paolini, F. R., & Rossi, B. B. 1962, Phys. Rev. Let., 9, 439

Gilfanov, M. et al. 1993, ApJ, 418, 884

Gorenstein, P., Gursky, H., & Garmire, G. 1968, ApJ, 153, 885

Gottlieb, E. W., Wright, E. L., Liller, W. 1975, ApJ , 195, L33

Gottwald, M., Parmar, A. N., Reynolds, A. P., White, N. E., Peacock, A., & Taylor, B. G. 1995, A&AS, 109, 9

Grindlay, J., Gursky, H., Schnopper, H., Parsignault, D., Heise, J., Brinkman, A. L., & Schrijver, J. 1976, ApJ, 205, L127

Gursky, H. 1994, in The Evolution of X-ray Binaries, eds. S. S. Holt & C. S. Day (New York: AIP), p. 39

Hartmann, D., Woosley, S. E., Arons, J. 1988, ApJ, 332, 777

Hasinger, G., & van der Klis, M. 1989, A&A, 225, 79

Hasinger, G., van der Klis, M., Ebisawa, K., Dotani, T., & Mitsuda, K. 1990, A&A, 235, 131

Hertz, P., Vaughan, B., Wood, K. S., Norris, J. P., Mitsuda, K., Michelson, P. F., Dotani, T. 1992, ApJ, 396, 201

Joss, P. C. 1977, Nature, 270, 310

Kaaret, P., Ford, E. C., & Chen, K. 1997, ApJ, 480, L27

Kahn, S. M. & Blissett, R. J. 1980, ApJ, 238, 417

Kahn, S. M. & Grindlay, J. E. 1984, ApJ, 281, 826

Kato, M. 1983, PASJ, 35, 33

Katz, J. I. 1976, ApJ 206, 910

———. 1987, High Energy Astrophysics (Menlo Park, CA: Addison-Wesley)

Kendziorra, E., Collmar, W., Brunner, H., Staubert, R., & Pietsch, W. 1985, Sp. Sc. Rev., 40, 361

Kompaneets, A. S. 1957, Sov. Phys. JETP, 4, 730

Kouveliotou, C., van Paradijs, J., Fishman, G. J., Briggs, M. S., Kommers, J., Harmon, B. A., Meegan, C. A., Lewin, W. H. G. 1996, Nature, 379, 799

Kuulkers, E. 1995, PhD Thesis, University of Amsterdam

Kuulkers, E., Parmar, A. N., Owens, A., Oosterbroek, T., & Lammers, U. 1997, A&A, submitted

Kuulkers, E. et al. 1994, A&A 1994, 289, 795

Kuulkers, E. & van der Klis, M. 1995, A&A, 305, 801

———. 1996, A&A 1994, 315, 567

Kuulkers, E., van der Klis, M., & van Paradijs, J. 1995, A&A 450, 748

Kuulkers, E., van der Klis, M., & Vaughan, B.A. 1996, A&A 1994, 311, 197

Kylafis, N. & Phinney, E. S. 1989, in Timing Neutron Stars, eds. H. Ögelman and E. P. J. van den Heuvel (Dordrecht: Kluwer), 731

Lamb, D. Q., & Lamb, F. K. 1978, ApJ, 220, 291

Lamb, F. K. 1989, in Proc. 23 ESLAB Symp. on X-ray Astronomy, ed. N. E. White (ESA SP-296), p. 215

Lamb, F. K. & Miller, M. C. 1995, ApJ, 439, 828

Lamb, F. K., Pethick, C. J., & Pines, D. 1973, ApJ, 224, 969

Lamb, F. K., Shibazaki, N., Alpar, M. A., & Shaham, J. 1985, Nature, 317, 681

Landau, L. D. & Lifshitz, E. M. 1987, Fluid Mechanics (Oxford: Pergamon Press)

Lewin, W. H. G., van Paradijs, J., & Taam, R. 1995, in X-ray Binaries, eds. W. H. G. Lewin, E. P. J. van den Heuvel, & J. van Paradijs, (Cambridge: University Press)

Lewin, W. H. G. et al. 1976, ApJ, 207, L95

Lewin, W. H. G., Rutledge, R. E., Kommers, J. M., van Paradijs, J., & Kouveliotou, C. 1996, ApJ, 462, L39

Litchfield, S. J. & Kylafis, N. D. 1996, A&A, 314, L25

Lyubarskij, Y. E. & Sunyaev, R. A. 1982, Sov. Astr. Let., 8, 330

Madej, J. 1989, ApJ, 339, 386

———. 1991, ApJ, 376, 161

Mason, K. O., Kahn. S. M., Charles, P. A., & Lampton, M. L. 1979, ApJ, 230, L163

Mastichiadis, A. & Kylafis, N. D. 1992, ApJ, 384, 136

Matt, G., Costa, E., Dal Fiume, D., Dusi, W., Frontera, F., & Morelli, E. 1990, ApJ, 355, 468

McCray, R. 1993, ARAA, 31, 175

McDermott, P. N. & Taam, R. E. 1987, ApJ, 318, 278

Mereghetti, S. & Grindlay, J. E. 1987, ApJ, 312, 727

Mereghetti, S. & Stella, L. 1995, ApJ, 442, L17

Middleditch, J. & Priedhorsky, W. C. 1986, ApJ, 306, 230

Mihalas, D. 1978, Stellar Atmospheres (New York: W.H. Freeman & Co.)

———. 1980, ApJ, 238, 1034

Mihalas, D. & Mihalas, B. W. 1984, Foundations of Radiation Hydrodynamics (Oxford: Oxford University Press)

Miller, G. S. 1990, ApJ, 356, 572

Miller, G. S. & Lamb, F. K. 1992, ApJ, 388, 541

Miller, G. S. & Park, M. G. 1995, ApJ, 440, 771

Miller, M. C. & Lamb, F. K. 1993, ApJ, 413, L43

———. 1995, ApJ, 439, 828

———. 1996, ApJ, 470, 1033

Miller, M. C., Lamb, F. K., & Psaltis, D. 1997, ApJ, submitted

Mitsuda, K. 1988, in Physics of Neutron Stars and Black Holes, ed. Y. Tanaka (Tokyo: Universal Academy Press), p. 117

Mitsuda, K., Inoue, H., Koyama, K., Makishima, K., Matsuoka, M., Ogawara, Y., Shibazaki, N., Suzuki, K., & Tanaka, Y. 1984, PASJ, 36, 741

Morrison, R. & McCammon, D. 1983, ApJ, 270, 119

Mukarami, T. et al. 1980, ApJ, 240, L143

Mushotzky, R. F., Done, C., & Pounds, K. 1993, ARAA 31, 717

Narayan, R., McClintock, J. E., & Yi, I. 1996, ApJ, 457, 821

Nagirner, D. I. & Poutanen, J. 1994, Astr. Sp. Phys. Rev., Vol. 9

Nozakura, T., Ikeuchi, S., & Fujimoto, M. Y. 1984, ApJ, 286, 221

Park, M. G. & Miller, G. S. 1991, ApJ, 371, 708

Payne, D. G. 1980, ApJ, 237, 951

Payne, D. G. & Blandford, R. D. 1981, MNRAS, 196, 781

Peebles, P. J. E. 1971, Physical Cosmology (Princeton: Princeton University Press)

Pomraning, G. C. 1973, The Equations of Radiation Hydrodynamics, International Series of Monographs in Natural Philosophy, Vol. 54 (Oxford: Pergamon Press)

Ponman, T. J., Foster, A. J., & Ross, R. R. 1990, MNRAS, 246, 287

Pozdnyakov, L. A., Sobol, I. M., & Sunyaev, R. A. 1983, Astr. Sp. Phys. Rev., 2, 189

Press, W. H., Teukolsky, S. A., Vetterling, W. T., Flannery, B. P. 1992, Numerical Recipes in Fortran (Cambridge: University Press)

Pringle, J. E. & Rees, M. J. 1972, A&A, 21, 1

Psaltis, D., Lamb, F. K., & Miller, G. S. 1995, ApJ, 454, L137

Psaltis, D. & Lamb, F. K., 1997a, ApJ, submitted

———. 1997b, in preparation

Rephaeli, Y. 1995, ARAA, 33, 541

Riffert, H. 1988, ApJ, 327, 760

Robinson, P. A. & Melrose, D. B., Aus. J. Phys. , 1984, 37, 675

Rybicki, G. B. & Lightman, A. L. 1979, Radiative Processes in Astrophysics (New York: John Wiley)

Schulz, N. S., Hasinger, G., & Trümper, J. 1989, A&A, 225, 48

Schulz, N. S., & Wijers, R. A. M. J. 1993, A&A, 273, 123

Shapiro, S. L., Lightman, A. P., & Eardly, D. M. 1976, ApJ, 204, 187

Shibazaki, N. & Lamb, F. K. 1987, ApJ, 318, 767

Shklovskii, I. 1967, ApJ, 148, L1

Smale, A. et al. 1993, ApJ, 410, 796

Smith, B. A., Morgan, E. H., & Bradt, H. 1997, ApJ, in press

Spitzer, L. 1956,

———. 1973,

Stollman, G. M., van Paradijs, J., Hasinger, G., Lewin, W. H. G., & van der Klis, M. 1987, MNRAS, 227, p7

Strohmayer, T. E., Zhang, W., Swank, J. H., Smale, A., Titarchuk, L., Day, C., &

Lee, U. 1996a, ApJL, 469, L9

Strohmayer, T., Lee, U., & Jahoda, K. 1996b, IAU Circ. 6484

Sunyaev, R. A. & Titarchuk, L. G. 1980, A&A, 86, 121

Sunyaev, R. A. & Zeldovich, Ya. B. 1980, ARAA, 18, 537

Suzuki, K., Matsuoka, M., Inoue, H., Mitsuda, K., Tanaka, Y., Ohashi, T., Hirano, T., & Miyamoto, S. 1984, PASJ, 36, 761

Swank, J. H., Becker, R. H., Boldt, E. A., Holt, S. S., Pravdo, S. H., & Serlemitsos, P. J. 1977, ApJ, 212, L73

Swank, J. H. & Serlemitsos, P. J. 1985, in Galactic and Extragalactic Compact X-ray Sources, ed. Y. Tanaka and W. H. G. Lewin (Tokyo: ISAS), 175

Sztajno, M., van Paradijs, J., Lewin, W. H. G., Langmeier, A., Trumper, J., & Pietsch, W. 1986, MNRAS, 222, 499

Taam, R. E., Woosley, S. E., & Lamb, D. Q. 1996, ApJ, 479, 251

Tanaka, Y. & Lewin, W. H. G. 1995, in X-ray Binaries, eds. W. H. G. Lewin, E. P. J. van den Heuvel, & J. van Paradijs, (Cambridge: University Press)

Tawara, Y., Hirano, T., Kii, T., Matsuoka, M., & Murakami, T. 1983, PASJ, 36, 861

Thorne, K. S. 1981, MNRAS, 194, 439

Thorne, K. S., Flammang, R. A., & Żytkow, A. N. 1981, MNRAS, 194, 475

Titarchuk, L. 1994, ApJ, 434, 570

Titarchuk. L. & Lyubarskij, Y. E. 1995, ApJ, 450, 876

Titarchuk, L., Mastichiadis, A., & Kylafis, N. D. 1997, ApJ, in press

Trimble, V. 1994, in The Evolution of X-ray Binaries, eds. S. S. Holt & C. S. Day (New York: AIP), p. 665

Turner, M. J. L., Smith, A., & Zimmerman, H. U., 1981, Space Sci. Rev., 30, 513

Turolla, R., Zane, S., Zampieri, L., & Nobili, L. 1997, MNRAS, in press

Ubertini, P., Bazzano, A., Cocchi, M., La Padula, C., & Sood,R. K. 1992, ApJ, 386, 710

Vacca, W. D., Sztajno, M., Lewin, W. H. G., Truemper,J., Van Paradijs,J., & Smith,A. 1987, ApJ, 172, 143

van der Klis, M. 1989, ARA&A, 27, 517

van der Klis, M., Hasinger, G., Stella, L., Langmeier, A., van Paradijs, J., & Lewin, W. H. G. 1987c, ApJ, 319c, 913

van der Klis, M., Jansen,F., van Paradijs,J., vandenHeuvel,E. P. J., & Lewin,W. H. G. 1985, Nature, 316, 225

van der Klis, M., Jansen,F., van Paradijs,J., Lewin,W. H. G., Sztajno, M., & Trumper, J. 1987a, ApJ, 313, L19

van der Klis, M., Stella, L., White, N. E., Jansen, F., & Parmar, A. N. 1987b, 316, 411

van der Klis, M. & Lamb, F. K. 1997, in preparation

van der Klis, M., Swank, J. H., Zhang, W., Jahoda, K., Morgan, E. H., Lewin, W. H. G., Vaughan, B., & vanParadijs, J. 1996, ApJ, 469, L1

van der Klis, M., Wijnands, R., Horne, K., & Chen, W. 1997, ApJ, in press

van Paradijs, J. 1991, in Neutron Stars: Theory and Observation, eds. J. Ventura & D. Pines (Dordrecht: Kluwer), p 245

———. 1995, in X-ray Binaries, eds. W. H. G. Lewin, E. P. J. van den Heuvel, & J. van Paradijs, (Cambridge: University Press)

van Paradijs, J. & van der Klis, M. 1994, A&A, 281, L17

Vaughan, B. A., van der Klis, M., Lewin, W. H. G., Wijers, R. A. M. J., van Paradijs, J., Dotani, T., & Mitsuda, K. 1994a, ApJ, 421, 738

Vaughan, B. A., van der Klis, M., Wood, K. S., Norris, J. P., Hertz, P., Michelson, P. F., vanParadijs, J., Lewin, W. H. G., Mitsuda, K., & Penninx, W. 1994b, ApJ, 435, 362

Vrtilek, S. D., Raymond, J. C., Garcia, M. R., Verbunt, F., Hasinger, G., & Kurster, M. 1990, A&A, 235, 162

White, N. E., Stella, L., & Parmar, A. N. 1988, ApJ 324, 363

White, N. E., Peakock, A., Hasinger, G., Mason, K. O., Manzo, G., Taylor, B. G., & Branduardi-Raymont, G. P. 1986, MNRAS 218, 129

White, N.E., Peacock, A., & Taylor. B. G. 1985, ApJ, 296, 475

Wijers, R. A. M. J., van Paradijs, J., & Lewin, W. H. G. 1987, MNRAS, 228, p17

Wijnands, R., van der Klis, M., Psaltis, D., Lamb, F. K., Kuulkers, E., Dieters, S., van Paradijs, J., & Lewin, W. H. G. 1996, ApJ, 469, L5

Wijnands, R. et al. 1997, A&A, submitted

Wood, K. S., Hertz, P., Norris, J. P., Vaughan, B. A., Michelson, P. F., Mitsuda, K., Lewin, W. H. G., vanParadijs,J., Penninx,W., & van der Klis,M. 1991, ApJ, 379, 295

Woosley, S. E. & Taam, R. E. 1976, Nature, 263, 101

Yin, W.-W. & Miller, G. S. 1995, ApJ, 449, 826

Zampieri, L., Turolla, R., Zane, S., & Treves, A. 1995, ApJ, 439, 849

Zampieri, L. et al. 1997, in preparation

Zane, S., Turolla, R., Nobili, L., & Erna, M. 1996, ApJ, 466, 871

Zhang, W., Lapidus, I., White, N. E., & Titarchuk, L. 1996, ApJL, 469

Zhang, W., Lapidus, I., Swank, J. H., White, N. E., & Titarchuk, L. 1997, IAU Circ. 6541

Vita

Dimitrios Psaltis was born in Serres, a town in northern Greece, on Monday June 1, 1970, a day he used to believe was the first day of the week, the first day of the month, and the first day of summer. It took four years in Kindergarten (procrastination was obvious even back then), six years in elementary school, three years in junior-high, and three years in high school for him to realize that neither is Monday the first day of the week nor is June 1st the first day of summer. In the meantime, he spent most of the years in junior-high and in high school working as a part-time programmer in a computer company. During the last year of high school he realized that he did not want to spend one more minute of his life debugging computer codes or studying Ancient Greek and decided to study Physics at the University of Thessaloniki. Within two months after graduating from high school he was hired by a computer company to develop software for the teaching of Ancient Greek in private and public schools! In the fall of 1988 he started attending classes at the Physics Department of the Aristotle University of Thessaloniki and soon afterwards he started looking for a research project. He never considered working on nuclear or particle physics being afraid that his work might be used for the development of nuclear weapons. A boring one-semester project in solid-state physics was enough to drive him as far away as possible from this field too. Research in Astronomy was the only obvious way forward (fortunately for his solid-state physics professors but unfortunatelly for his astronomy ones) and he spent the last 3 years in college working on various problems in astronomy at the Observatory of the University of Thessaloniki, as well as at the Astronomical Institute of the University of Amsterdam (funded by

the Erasmus program for exchange students) and at the Max-Planck Institute fuer Radioastronomie in Bonn. He graduated in July 1992 and started his graduate studies in the Astronomy Department of the University of Illinois at Urbana-Champaign. After spending a year trying to solve unsolvable homework problems, he started working on his doctoral thesis with his advisor, Fred Lamb. Ever since, he has spent his time mostly debugging his radiative transport code and working on a project that could (but he really hopes it won't) be used for developing nuclear weapons.